MASTERARBEIT / MASTER'S THESIS

Titel der Masterarbeit / Title of the Master's Thesis

Experimental Multi-Photon High-Dimensional Entanglement

verfasst von / submitted by

Manuel Erhard BSc.

angestrebter akademischer Grad / in partial fulfilment of the requirements for the degree of

Master of Science (MSc.)

Wien, 2016 / Vienna, 2016

Studienkennzahl lt. Studienblatt / degree programme code as it appears on the student record sheet:	A 066 876
Studienrichtung lt. Studienblatt / degree programme as it appears on the student record sheet:	Masterstudium Physik
Betreut von / Supervisor:	o.Univ.-Prof. Dr. Anton Zeilinger

Contents

Abstract

Quantum entanglement is a phenomenon that describes very strong correlations between physical quantum systems and cannot be explained by classical theories. Experimentally, quantum entanglement has been shown in a variety of physical systems, for example, 14 ions entangled in 2 dimensions each or two photons entangled in more than 100 dimensions each. So far, no experimental demonstration of the entanglement of more than two particles in more than two dimensions has been reported in the literature. Thus, this thesis aims to experimentally create the first simultaneously multi-partite and high-dimensional entangled state. Specifically, a three-photon entangled state, where two photons reside in a three dimensional state space and one photon resides in a two dimensional space is created. In order to create such a state, several novel techniques such as a Hong-Ou-Mandel (HOM) effect in the orbital-angular-momentum (OAM) degree of freedom and a high-dimensional entanglement router (HDR) are developed. Furthermore, merging these newly developed tools and exploiting the OAM-HOM effect at the HDR results in creating the first multi-partite high-dimensionally entangled state. Very high visibilities of more than 90 percent were achieved in OAM-HOM interference, demonstrating the suitability of using the OAM of photons for such experiments. Additionally, long term stability of the HDR for more than 35 hours and the high routing precision during this time prove the usefulness of this device for multi-photon experiments. Finally, the high-dimensional multi-partite state was created with an experimental fidelity of more than 80 percent as compared to an ideal pure state. A fidelity witness designed to test for the presence of high-dimensional multi-partite entanglement was violated by 7 standard deviations, clearly showing the creation and verification of the first multi-photon and high-dimensionally entangled state. The results presented in this work demonstrate the capability of the OAM of photons to serve as a test bed for even more complex quantum states in the future.

Zusammenfassung

Das quantenphysikalische Phänomen der Verschränkung beschreibt Korrelationen zwischen quantenphysikalischen Systemen welche mit klassisch-physikalischen Theorien nicht erklärbar sind. Diese Verschränkung wurde experimentell bereits in komplexen Systemen mit bis zu 14 Ionen in zwei Dimensionen, oder auch zwischen zwei Photonen in mehr als 100 Dimensionen nachgewiesen. Allerdings gibt es bis heute keinen experimentellen Nachweis von Verschränkung in einem System zwischen mehr als zwei Objekten und gleichzeitig in mehr als 2 Dimensionen. Die vorliegende Arbeit hat daher zum Ziel, Verschränkung in einem derartig komplexen System zum ersten Mal experimentell nachzuweisen. Genauer gesagt sollen drei Photonen derart miteinander verschränkt werden, dass zwei Photonen in einem drei-dimensionalen Zustandsraum existieren, während das dritte in einem zwei-dimensionalen Zustandsraum verbleibt. Um solch einen Zustand experimentell erzeugen zu können, wurden neuartige Techniken wie z.B. ein Hong-Ou-Mandel (HOM) Effekt im Drehimpuls-Freiheitsgrad von Photonen (OAM) oder auch ein hochdimensionaler Router (HDR) für Quantenzustände entwickelt. Die geschickte Kombination dieser Elemente in Form eines OAM-HOM Effektes direkt am HDR erlaubt es letztlich, die Verschränkung von mehreren Photonen in mehreren Dimensionen zu erzeugen. Experimentell wurde ein Interferenzkontrast des OAM-HOM Effekts von mehr als 90 Prozent erreicht, was auf die gute technische Beherrschbarkeit des Drehimpuls-Freiheitsgrades der Photonen zurückzuführen ist. Die Langzeitstabilität des HDR von mehr als 35 Stunden bei konstant hoher Routing-Qualität demonstriert die Einsatztauglichkeit dieses Elements in Viel-Photon-Experimenten. Letztlich wurde der hochdimensionale Viel-Photon-Quantenzustand mit einem Überlapp von mehr als 80 Prozent zum theoretischen Idealzustand bestätigt. Dieses Ergebnis konnte mit Hilfe eines Verschränkungszeugen mit einer statistischen Sicherheit von 7 Standardabweichungen belegt werden. Die vorgelegten experimentellen Ergebnisse zeigen deutlich, dass der Drehimpuls von Photonen auch zur Realisierung von Quantensystemen mit noch komplexerer Verschränkung geeignet ist.

Introduction

One of the most intriguing and fascinating effects in quantum mechanics is entanglement. The word entanglement in this context describes a very strong connection between at least two spatially separated physical objects that is not explainable using classical physics. Historically, the seminal paper by Einstein, Podolsky and Rosen (EPR) [1] published in 1935 is the first work investigating this strong connection. Later that year, Schrödinger named this strong connection *"Verschränkung"*[1] in his famous work *Die gegenwärtige Situation in der Quantenmechanik* [2]. The groundbreaking article *"On the Einstein Podolski Rosen Paradox"* by John Bell in 1964 [3] used entanglement to derive an inequality, the so-called Bell-inequality, that allows one to experimentally verify that nature is indeed as counterintuitive as predicted by quantum theory. Soon after this, quantum entanglement not only proved to be useful for answering fundamental questions, but also in modern technology. Ranging from applications in unconditionally secure communication to ultra-precise metrology, quantum entanglement promises huge advantages for future applications based on this technology. Today, a wide range of research areas has been established investigating entanglement in very different operational systems. Trapped ions [4], superconducting circuits [5], NV-centers [6], electrons [7], and photons [8] are all examples of different physical systems that have been shown to be capable of being entangled. The simplest system exhibiting entanglement is a two-partite two-level system. Such a theoretical system describes for example a physical system consisting of two electrons in their spin degree of freedom, or two photons in their polarization degree of freedom. The main focus of research so far has been on increasing the number of particles entangled. This is mainly due to the fact that for a general quantum computer, many entangled qubits (two-level particles) are necessary. The current record for the highest number of particles entangled in two dimensions is with 14 ions [4]. Just recently, the entanglement dimensionality of a two-photon state was been shown to be at least 103-dimensionally entangled [8]. Although there has been theoretical work on multi-partite and high-dimensionally entangled systems [9], there have been no reports of experiments creating such states.

Therefore, this thesis aims to investigate the creation and verification of the first simultaneously multi-partite and high-dimensional entangled state. The information carriers of choice for this experiment are photons. Photons have a very low decoherence rate and at the same time allow certain degrees of freedom to be manipulated in a highly controlled fashion. Secondly, the orbital-angular-momentum (OAM) degree of photons naturally spans a high-dimensional state space, thus it is perfectly fitted for the task at hand. In this thesis, established methods like Hong-Ou-Mandel [10] interference for creating multi-partite entangled states are generalized to the OAM degree of freedom. Furthermore, a new device called a high-dimensional entanglement router (HDR) is developed. The HDR is capable of routing a high-dimensional entangled state into two spatially separated lower-dimensional entangled states. Finally, a novel experiment using the OAM-HOM effect at the HDR is proposed and realized in the lab to create, for the first time, a three-particle high-dimensionally entangled quantum state. The results of this thesis show how to experimen-

[1] entanglement

tally create and verify multi-partite and high-dimensionally entangled states. These experiments pave the way for investigating even more complicated entanglement structures. Given these new tools, other fundamentally interesting quantum states such as a high-dimensional version of the Greenberger-Horne-Zeilinger (GHZ) state [11] could be created in high dimensions. Creating and investigating such states potentially leads to further fundamental insight into the strange behavior of the quantum world. Going to multiple particles in high-dimensions also opens the possibility for realizing complex quantum communication protocols by introducing a completely new type of asymmetric entanglement structure that simply does not exist in two-dimensional bipartite entanglement.

Chapter 1

"Verschränkung" — Entanglement

"Bestmögliche Kenntnis eines Ganzen schließt nicht bestmögliche Kenntnis seiner Teile ein– und darauf beruht doch der ganze Spuk."[1]
— Erwin Schrödinger, *Die gegenwärtige Situation in der Quantenmechanik [2]*

1.1 *Verschränkung* – A Brief History

The concept of entanglement appeared for the first time in 1935 in the seminal paper by Einstein, Podolsky and Rosen [1]. In this article the authors posed the question whether the quantum mechanical description of physical reality can be considered complete or not. Here we will solely focus on the part referring to entanglement rather than the implications that the EPR paradox actually give rise to. The *"Gedankenexperiment"*[2] assumes the following situation: Two separate particles are in a well defined state before $t = 0$. Then these two particles interact for some time T. During the interaction time only the combined state exists and in general it *cannot* be separated anymore. After the time $t = T$ the two systems are *not* interacting anymore. This non-separability of the wave-functions is then called *"Verschränkung"* in Erwin Schrödinger's essay "Die gegenwärtige Situation in der Quantenmechanik" [2]. Literally translated this word means *entanglement*. Its origin is actually from the idea that the two wave functions are tangled up in a way such that they cannot, even in principle, be separated anymore. Thus only the combined state remains. Note that even though only the combined state exists, this does not mean that the two particles are at the same place. Actually this is the most important point, that the two particles are well separated spatially. But what implications does this *entanglement* has now? Consider two physical observables $A_{1,2}, B_{1,2}$ acting on two physical systems $1, 2$. Now after the interaction time T, the two particles are well separated spatially and the two different measurements A and B are performed. As shown in the EPR paper, this leads to the following results:

$$A_1 = A_2 \quad \text{and} \quad B_1 = -B_2. \tag{1.1}$$

This means that whenever measurement A_1 is performed on system 1, it is known with certainty that a measurement A_2 performed right after the first one A_1 results in exactly the same outcome

[1] "Best possible knowledge of a whole does not include best possible knowledge of its parts – and that is what keeps coming back to haunt us.", Trans. John D. Trimmer [12]

[2] thought-experiment

on system 2. The situation is analogous for the B measurements, but with anti-correlated measurement outcomes. Is this calculation telling us that even though the two particles are far apart from each other and *not* interacting anymore, that if we perform a measurement on one system we know with certainty the outcome of the second measurement performed later on the other system? Indeed it does, and the reason for that is exactly this new phenomenon called *entanglement*. Now we can also understand the famous quote from Einstein *"spooky action at a distance"*. Today, we have a complete branch of physics that developed out of these seminal articles, namely, that of quantum information. The modern view of entanglement is very much like the one in Schrödinger's essay- it is about information. Although entanglement is hard to grasp empirically, there exists a surprisingly simple mathematical definition. In the following text we will focus on the mathematical description of entanglement rather than the implications on the interpretation of quantum mechanics and appearing paradoxes.

1.2 *Verschränkung* – From a Mathematical Point of View

In this section we will focus on the mathematical description of entanglement. Therefore, we assume that the reader is familiar with the basic mathematics and theoretical concepts that underly quantum theory. The overall aim of this section is to explain and understand what *"Multi-Partite High-Dimensional Entanglement"* means. However, keep in mind that quantum information theory is still a very active research area, thus we will not be able to give a final answer to all the questions that may arise. Additionally, there are many exciting and interesting theorems in quantum information theory and we will by far not be able to cover them all here. The interested reader is referred to the following papers which give an excellent overview [13, 14, 15, 16].

1.2.1 Definitions and Restrictions

As we will see in the following, although the mathematical idea of *separability* is formulated in a simple way, the operational approach is very difficult in general. Actually, only a few classes restricted in their number of particles and dimensionality are understood well. For a given quantum state we may ask the following questions, see Fig. 1.1.

In mathematical terms a quantum mechanical system is described by a *Hilbert* space $\mathcal{H}$. It is postulated that a number of such systems, denoted $\mathcal{H}^1, \mathcal{H}^2, ..., \mathcal{H}^N$, are represented in a *Hilbert* product space

$$\mathcal{H}^{12\cdots N} = \mathcal{H}^1 \otimes \mathcal{H}^2 \otimes \cdots \otimes \mathcal{H}^N, \tag{1.2}$$

with $\otimes$ denoting the tensor product. A general quantum state is denoted by its density matrix ρ where $\rho \in \mathcal{H}^{12}$. In this work the focus lies on discrete and unbounded Hilbert spaces. Thus continuous variable systems are not treated here. The first question raised in Fig. 1.1 is mathematically formulated as follows:

Definition 1.2.1. Separability for pure states: Suppose a Hilbert space $\mathcal{H}$ is composed of two subspaces $\mathcal{H}^1$ and $\mathcal{H}^2$ such that $\mathcal{H}^{12} = \mathcal{H}^1 \otimes \mathcal{H}^2$ holds. Furthermore, assume an element of the composite Hilbert space $|\psi\rangle \in \mathcal{H}^{12}$. We call $|\psi\rangle$ separable if and only if it can be written as $|\varphi_{1,2}\rangle \in \mathcal{H}^{1,2}$, meaning $|\psi\rangle = |\varphi_1\rangle \otimes |\varphi_2\rangle$.

Definition 1.2.2. Separability for mixed states: Similar to the case for pure states, we assume a Hilbert space $\mathcal{H}^{12} = \mathcal{H}^1 \otimes \mathcal{H}^2$ and a mixed state ρ which is an element of this space $\rho \in \mathcal{H}$. A mixed state ρ is called a separable state iff it can be written as $\rho = \sum_i p_i \rho_1^i \otimes \rho_2^i$, with $p_i \geq 0$, $\sum_i p_i = 1$ and $\rho_1 \in \mathcal{H}^1, \rho_2 \in \mathcal{H}^2$.

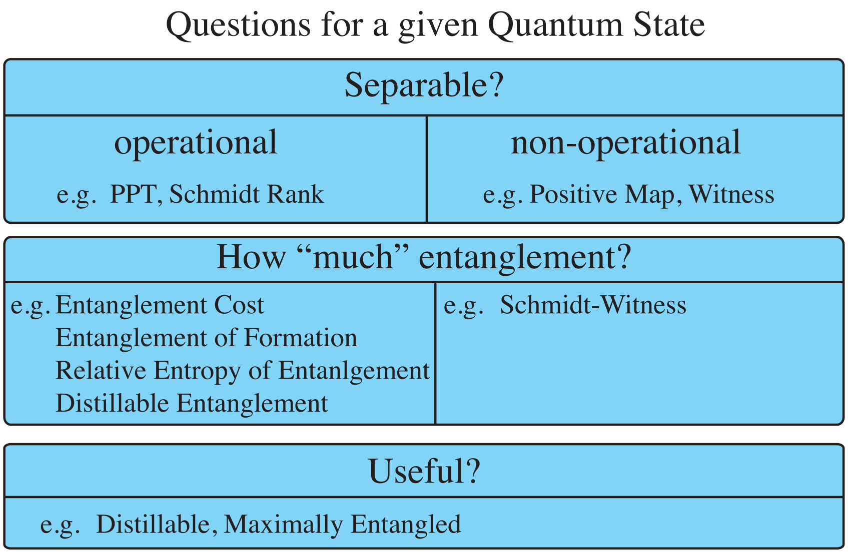

Figure 1.1: Questions for a given quantum state. The most important question is whether the state is separable or not. If yes, the next question is probably how much is this state entangled? Is it useful for some applications or fundamental questions?

As depicted in Fig. 1.1, there is a distinction between *operational* and *non-operational* tools. Operational here means that there exists a “simple” algorithm to determine whether a given quantum state is separable or not. More insight and examples are given later in the text. With these definitions of the separability of a given quantum state it is possible to define entanglement in a mathematical form:

Definition 1.2.3. Entanglement: We call a quantum state ρ (pure or mixed) entangled, if and only if it is *non-separable*.

While this definition is simple to understand, it remains an NP-hard problem to decide whether a given state ρ is actually separable or non-separable [17]. Thus finding necessary and sufficient conditions for general states is still part of active research. To illustrate such an operational separability criterion let us give an example:

The Positive Partial Transpose:
For a 2×2 or 2×3 dimensional bipartite system, a necessary and sufficient condition for separability that should be mentioned here is the so called “PPT” or “Peres-Horodecki criterion” [18]. For this assume a general state

$$\rho = \sum_{i,j,k,l} p_{k,l}^{i,j} \, |i\rangle\langle j|_A \otimes |k\rangle\langle l|_B \, . \tag{1.3}$$

The partial transpose on subsystem B is denoted as $\rho^{T_B} = (\mathbb{I} \otimes T)\rho$, meaning the identity is applied to system A and the transpose map[3] is applied to system B. The criterion states that if ρ^{T_B} has negative eigenvalues, then ρ is guaranteed to be entangled. Note, this is only sufficient for $\rho \in \mathcal{H}$ with $\dim(\mathcal{H}) \leq 6$.

Another powerful tool for *pure* states is the so called **Schmidt decomposition**:

[3]the subspace B is transposed: $|k\rangle\langle l|_B \xrightarrow{T_B} |l\rangle\langle k|_B$

Theorem 1. *A pure state $|\psi_{AB}\rangle \in \mathcal{H}^{AB}$ with $\mathcal{H}^{AB} = \mathcal{H}_A \otimes \mathcal{H}_B$ and $dim(\mathcal{H}_A) = m \leq dim(\mathcal{H}_B) = n$ has Schmidt-rank $r \leq m$ if it can be decomposed as the bi-orthogonal sum*

$$|\psi_{AB}\rangle = \sum_{i=1}^{r} \lambda_i \, |a_i\rangle \, |b_i\rangle \,, \tag{1.4}$$

with $\lambda_i > 0$, $\langle a_i | b_j \rangle = \delta_{ij}$ and $\sum_{i=1}^{r} \lambda_i^2 = 1$.

A given pure state $|\psi_{AB}\rangle$ is called separable if and only if $r = 1$. Note that this is easy to compute since the λ_i^2 are the eigenvalues of the reduced density matrices, see Appendix A.1.

Non-operational tools to distinguish separable from non-separable states include for e.g. positive maps [14] or entanglement witnesses [16]. In the following paragraph, the fundamental theorem of entanglement witnesses is explained:

Theorem 2. *A general quantum state $\rho \in \mathcal{H}$ is entangled iff there exists a hermitian operator $\mathcal{W}$ such that*

$$\mathrm{Tr}\,(\rho\mathcal{W}) < 0, \tag{1.5}$$

otherwise the quantum state ρ is called separable. This is a direct consequence of the Hahn-Banach *theorem of functional analysis [19, 20].*

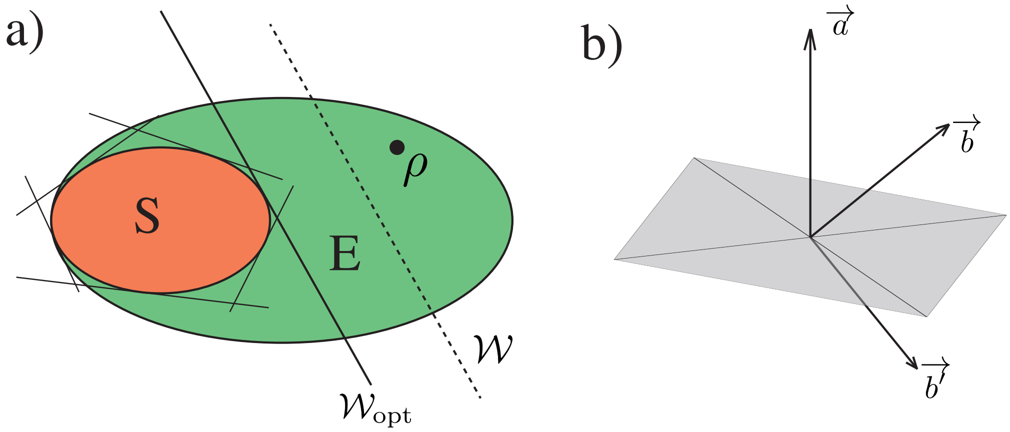

Figure 1.2: Intuitive picture of entanglement detection with witnesses. **a)** S, E are separable and entangled sets, respectively. Given a quantum state ρ there exists according to theorem 2 a hermitian operator $\mathcal{W}$ to detect whether $\rho \in$ S or $\rho \in$ E. In order to completely distinguish S and E for all possible density matrices ρ an infinite number of witnesses $\mathcal{W}$ are necessary. Note that the dashed line represents the hyperplane $\mathrm{Tr}\,(\rho\mathcal{W}) = 0$. Additionally, it is not necessary that a given $\mathcal{W}$ optimally detects an entangled state ρ. But there exist cases where an optimal entanglement witness $\mathcal{W}_{\mathrm{opt}}$ can be constructed. **b)** Analog picture in vector representation. The scalar product of two normalized vectors $\vec{a}$ and $\vec{b}$ is negative dependent on which side $\vec{b}$ is on.

In order to get an intuitive idea of what an entanglement witness means, it is helpful to think of $\mathrm{Tr}\,(\rho\mathcal{W})$ as a scalar product $\langle \rho^\dagger, \mathcal{W} \rangle$. The scalar product of two normalized vectors $\vec{a}$ and $\vec{b}$ reads $\vec{a} \cdot \vec{b} = \cos(\varphi)$, with φ describing the enclosed angle between $\vec{a}$ and $\vec{b}$. All vectors orthogonal to $\vec{a}$ span a plane. Vectors on this plane have a scalar product of zero and enclose an angle of $\pi/2$ with $\vec{a}$. According to the properties of the cosine, $\cos(\varphi) \in [-1, 1]\ \forall \varphi \in [0, \pi]$, the scalar product is either positive (e.g. $\overrightarrow{b}$) or negative (e.g. $\overrightarrow{b'}$). Hence, vectors $\overrightarrow{b}$ or $\overrightarrow{b'}$ on one side of the plane orthogonal to $\overrightarrow{a}$ yield a positive or negative outcome, respectively. This picture can also be transferred to the hyperplane spanned by $\mathrm{Tr}\,(\rho\mathcal{W}) = 0$. Density matrices on one side of this hyperplane yield a negative result and are guaranteed to be entangled, while the ones with a positive outcome are not guaranteed to be entangled.

Now suppose a given quantum state ρ is shown to be non-separable, then the next question one could ask is *how* entangled is this state? In Fig. 1.1 some examples for different entanglement measures are given. We will focus on two specifically the relative entropy of entanglement and the Schmidt witness. The first one beautifully shows the connection of information and entanglement and the second one is essential for the understanding of this work. There are several requirements for a "good" entanglement measure [16]:

- *Separability*
  If ρ is seperable, then $E(\rho) = 0$.
- *Normalization*
  If ρ is a state consisting of two d-dimensional systems, then $E(\rho) = \log_2(d)$.
- *No increase under LOCC*
  $E(\rho)$ does not increase under local operations and classical communications
- *Continuity*
  In the limit of zero distance between two density matrices, the difference of their entanglement measures is also zero.
- *Additivity*
  A number of N identical copies of a quantum state contains N times the entanglement of one copy.
- *Subadditivity*
  The entanglement measure of the tensor product of two density matrices is not greater than the sum of the entanglement of both systems, $E(\rho_1 \otimes \rho_2) \leq E(\rho_1) + E(\rho_2)$.
- *Convexity*
  The entanglement measure is a convex function.

In general, not all the examples given in Fig. 1.1 fulfill the above mentioned requirements. A simple yet instructive example of an entanglement measure is the so-called entropy of entanglement. Let us first define the Von Neumann entropy:

Definition 1.2.4. von Neumann Entropy:

$$S\,(\rho) = -\mathrm{Tr}\,(\rho\log\rho) \tag{1.6}$$

Rewriting ρ into a decomposition of eigenstates yields $\rho = \sum_i \lambda_i \left|i\right\rangle \left\langle i\right|$. Hence, the Von Neumann entropy then reads

$$S\,(\rho) = -\sum_i \lambda_i \log\lambda_i. \tag{1.7}$$

This equation directly shows the similarity between the Von Neumann entropy and the information-theoretically defined Shannon entropy [21]. If ρ is a pure bipartite state the following theorem applies:

Theorem 3. *Suppose ρ is a pure bipartite d-dimensional quantum state. Then $E(\rho)$ is called an entanglement measure if $E(\rho) = S(\rho_A) = S(\rho_B)$, with $\rho_{A,B}$ denoting the partial trace with respect to the according subsystem $\rho_i = \mathrm{Tr}_j(\rho)$ and j denotes the complement of i.*

For the proof of the theorem see Appendix A.2. Let us briefly study two instructive cases, a pure separable state and a maximally entangled state. For a pure separable two-dimensional state let us write

$$|\psi_s\rangle = 1/2\,(|0\rangle + |1\rangle) \otimes (|0\rangle + |1\rangle) = 1/2\,(|0,0\rangle + |0,1\rangle + |0,1\rangle + |1,1\rangle)\,. \tag{1.8}$$

The corresponding density matrix reads $\rho_s = |\psi_s\rangle\langle\psi_s| = 1/4\sum_{i,j,k,l=0}^{1}|ij\rangle\langle kl|$). The partial trace over sub-system B leads to $\rho_s^A = 1/2\sum_{i,l=0}^{1}|i\rangle\langle l|$. Hence for the entanglement measure

$$E(\rho_s) = S(\rho_s^A) = -\mathrm{Tr}(\rho_s^A \log \rho_s^A) = -\sum_{i=0}^{1}\lambda_i \log \lambda_i, \tag{1.9}$$

where $\lambda_0 = 0$ and $\lambda_1 = 1$ and thus $E(\rho_s) = 0$. Note that $\lim_{x\to 0} x\log(x) \to 0$. We have thus calculated that a bipartite pure two-dimensional quantum state is not entangled and its entanglement entropy therefore is zero.

Repetition of the same calculation for a maximally entangled state Bell state

$$\left|\varphi^+\right\rangle = 1/\sqrt{2}\,(|0,0\rangle + |1,1\rangle) \tag{1.10}$$

leads to $E(\rho_{\varphi^+}) = 1$. Thus, although the von Neumann entropy for the total state $\left|\varphi^+\right\rangle$ gives $S(\rho_{\varphi^+}) = 0$ meaning we have all information available, the von Neumann entropy for the subsystems only lead to $S(\rho^A_{\varphi^+}) = S(\rho^B_{\varphi^+}) = 1$ meaning we have no information about the state. This directly leads us the beautiful quote stated in the beginning of this chapter:

> *"Best possible knowledge of a whole does not include best possible knowledge of its parts – and that is what keeps coming back to haunt us."*

It is very fascinating and impressive that Schrödinger had such deep insights even though complex mathematical tools such as these hadn't been developed at that time.

A very important concept for this thesis are the so called *Schmidt classes* [22]. For this classification, the Schmidt-rank defined in theorem 1 is generalized to the *Schmidt-number k* for mixed bipartite systems [23].

Definition 1.2.5. Schmidt-Number: A bipartite system with density matrix ρ has Schmidt number k if

(i) for any decomposition of $\rho = \sum_i p_i |\psi_i\rangle\langle\psi_i|$ with $p_i \geq 0$ at least one of the vectors $\{|\psi_i\rangle\}$ has Schmidt-rank k,

(ii) there exists a decomposition of ρ with all vectors $\{|\psi_i\rangle\}$ of Schmidt-rank at most k.

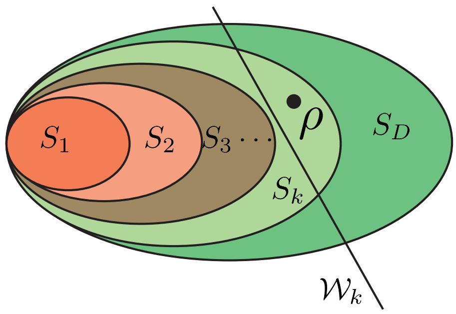

Figure 1.3: Russian nesting doll-like structure of the Schmidt classes. $\mathcal{W}_k$ denotes a hermitian operator to detect a density matrix ρ.

Note, for pure states ρ the Schmidt number and
Schmidt rank are equivalent. Additionally, the Schmidt number does not increase under local operations and classical communication (LOCC). According to the Schmidt number, a given quantum state can further be classified into Schmidt classes S_k. A Schmidt class S_k is a subset of all density matrices ρ that contains the density matrices $\rho_k \in S_k$ that have a Schmidt number $\leq k$. The Schmidt classes are successively embedded into each other like a Russian nesting doll $S_1 \subset S_2 \subset \cdots \subset S_D$, see Fig. 1.3. Furthermore, Schmidt class witnesses $\mathcal{W}_k$ are defined as follows.

Definition 1.2.6. Schmidt Witness: A given quantum state $\rho \in S$ can be further classified according to Schmidt classes with a hermitian operator $\mathcal{W}_k$. For

$$\rho \in S_k : \quad \mathrm{Tr}(\rho \mathcal{W}_k) < 0 \tag{1.11}$$

$$\rho \in S_{s<k} : \quad \mathrm{Tr}(\rho \mathcal{W}_k) \geq 0 \tag{1.12}$$

In section **??** we will explicitly show how to construct such a bipartite high-dimensional witness.

Now the final step to reach the aim of this chapter is to take multiple parties into account. So far, our focus lay on bipartite systems and the corresponding mathematical tools to decide whether a given bipartite state is separable or entangled. The basic idea of the *Schmidt-Rank-Vector* [9] is to investigate all possible bipartitions and store the dimensionality information (Schmidt number) of each bipartition in a vector. Let us consider a quantum system composed of three subsystems $|\psi_{\mathrm{ABC}}\rangle \in \mathcal{H}_{\mathrm{A}} \otimes \mathcal{H}_{\mathrm{B}} \otimes \mathcal{H}_{\mathrm{C}}$. For simplicity only pure states are considered for now, thus $\rho_{\mathrm{ABC}} = |\psi_{\mathrm{ABC}}\rangle\langle\psi_{\mathrm{ABC}}|$.

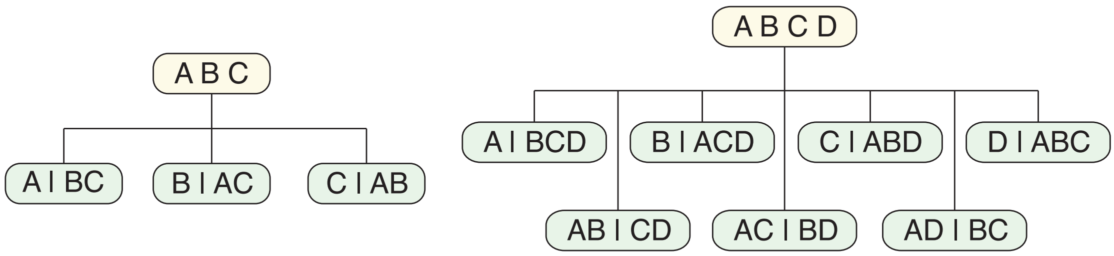

Figure 1.4: Bipartite decomposition of multi-partite systems. A tripartite system ABC is decomposed into three bipartite systems. Here $x|yz$ denotes the bipartition x with respect to yz, where yz is still combined. Similarly, for a four partite system ABCD, seven bipartite subsystems exist. In general, $2^{n-1} - 1$ bipartitions exist for an n-partite system.

As shown in Fig. 1.4 the tripartite system can be decomposed into three possible bipartitions $\rho_{\mathrm{A|BC}}, \rho_{\mathrm{B|AC}}$ and $\rho_{\mathrm{C|AB}}$. From Def. 1.2.5 it is already clear how to classify bipartite systems according to their entanglement dimensionality. As mentioned before, for pure states the Schmidt number is equivalent to the Schmidt rank. The Schmidt rank is denoted as r_i, with $r_i = \mathrm{rank}(\rho_i)$, $\rho_i = \mathrm{Tr}_j(\rho)$ and j denotes the complement of i. Thus the Schmidt rank vector (SRV) reads $\mathrm{SRV}(\rho_{\mathrm{ABC}}) = (r_{\mathrm{A}}, r_{\mathrm{B}}, r_{\mathrm{C}})$, with r_i denoting the Schmidt number of the respective bipartition. Note, that $r_{\mathrm{A}} = r_{\mathrm{BC}}, r_{\mathrm{B}} = r_{\mathrm{AC}}$ and $r_{\mathrm{C}} = r_{\mathrm{AB}}$ holds. Due to the sub-additivity of the Renyi 0-entropy[4] only certain combination of r_i's are allowed. Suppose $r_{\mathrm{A}} \geq r_{\mathrm{B}}, r_{\mathrm{C}}$, then for every combination fulfilling $r_{\mathrm{A}} \leq r_{\mathrm{B}} \cdot r_{\mathrm{C}}$ a pure state $|\psi_{\mathrm{ABC}}\rangle$ exists realizing this combination. This boundary condition is not sufficient any more for four or n-partite systems.

[4]which translates as the sub-multiplicity of the Schmidt rank

Table 1.1: Different tripartite pure states and their Schmidt rank vectors (SRV). Note, the SRVs are always sorted such that (r_1, r_2, r_3) with $r_1 \geq r_2 \geq r_3$. Normalization is omitted for the sake of readability.

Nr.	State	SRV
1	$\|000\rangle + \|111\rangle + \|201\rangle + \|321\rangle$	(4,3,2)
2	$\|000\rangle + \|111\rangle + \|221\rangle + \|321\rangle$	(3,3,2)
3	$\|000\rangle + \|111\rangle + \|222\rangle$	(3,3,3)
4	$\|000\rangle + \|111\rangle + \|220\rangle$	(3,3,2)
5	$\|000\rangle + \|111\rangle + \|210\rangle$	(3,2,2)
6	$\|000\rangle + \|111\rangle$	(2,2,2)
7	$(\|00\rangle + \|11\rangle + \|22\rangle) \otimes \|0\rangle$	(3,3,1)

Definition 1.2.7. Schmidt-Rank-Vector (SRV): Given a pure tripartite state $|\psi\rangle \in \mathcal{H}_{\mathrm{ABC}}$, the Schmidt rank vector is defined as

$$\mathrm{SRV}(|\psi\rangle) := (r_A, r_B, r_C)\,, \tag{1.13}$$

with $r_i = \mathrm{rank}(\rho_i)$, $\rho_i = \mathrm{Tr}_j(\rho)$ and j denotes the complement of i.

Some general remarks about the SRV:

(i) A given state $|\psi\rangle$ is called multipartite entangled iff $r_i \geq 2, \forall i$.

(ii) Different subsets in the SRV are LOCC incomparable, this means it is not possible to transform a state from $(4, 3, 2) \rightarrow (3, 3, 2)$ with LOCC transformations. This results from the LOCC invariance of the Schmidt rank. Note that this only imposes a partial ordering (e.g. for mixed states).

(iii) There exists a Russian nesting doll like structure for pure states only.

(iv) The lack of a Russian nesting doll-like structure for mixed states can be explained as follows. Consider two subsets e.g. (4,2,2) and (3,3,2) see Fig. 1.5. It cannot be guaranteed that for a set of mixed states $\rho = p\,|\psi_{422}\rangle\langle\psi_{422}| + (1-p)\,|\psi_{332}\rangle\langle\psi_{332}|$ one is always embedded in the other.

There exists a generalization to mixed states to resolve the above mentioned inconsistency and get a clear mathematical structure. Since this generalization is not necessary for this thesis the interested reader is referred to [9]. In table 1.1 some examples of tripartite high-dimensionally entangled pure states are given. While the first state in table 1.1 is indeed a $(4, 3, 2)$ entangled state, the second (very similar looking) state is not. The third state shows a generalization of the famous GHZ-like state [11]. Two different (3,3,2) states (2^{nd} and 4^{th}) can have the same SRV. The difference will be clear after the definition of the maximally entangled states. Additionally, to show an example of the lowest genuinely tripartite high-dimensionally entangled SRV state, a (3,2,2) state in number 5 is displayed. The two-dimensional GHZ state has an SRV of (2,2,2), thus showing genuine tripartite entanglement in two dimensions. A three-dimensional maximally entangled bipartite state in a product state with a third party (number 7) has a SRV of (3,3,1) and hence belongs to the bi-separable set displayed in Fig. 1.5.

To further clarify the SRV and gain some more insight, let us also consider different high-dimensional quadripartite systems. In table 1.2 different quadripartite pure states are displayed. The first state is a four-dimensional quadripartite GHZ like state. Other dimensionality structures

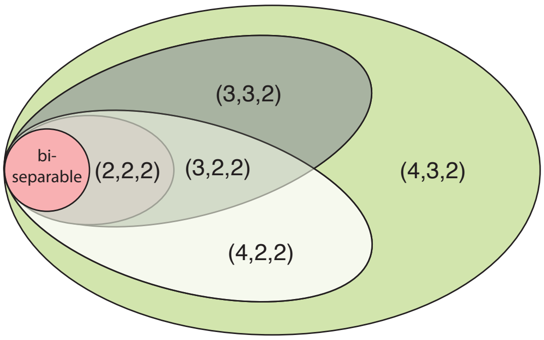

Figure 1.5: Structure of the SRV-subsets of a given $|\psi\rangle_{432}$ state.

Table 1.2: Different quadripartite pure states and their Schmidt rank vectors (SRV). Note, the SRVs are always sorted such that $(r_1, r_2, r_3, r_4, r_5, r_6, r_7)$ with $r_1 \geq r_2 \geq \cdots \geq r_7$. Normalization is omitted for the sake of readability.

Nr.	State	SRV
1	$\lvert 0000\rangle + \lvert 1111\rangle + \lvert 2222\rangle + \lvert 3333\rangle$	(4,4,4,4,4,4,4)
2	$\lvert 0000\rangle + \lvert 1111\rangle + \lvert 2222\rangle + \lvert 3210\rangle$	(4,3,3,3,3,3,3)
3	$\lvert 0000\rangle + \lvert 1211\rangle + \lvert 2200\rangle + \lvert 3210\rangle$	(4,2,2,2,2,2,2)
4	$(\lvert 00\rangle + \lvert 11\rangle) \otimes (\lvert 00\rangle + \lvert 11\rangle)$	(4,2,2,2,2,1,1)
5	$\lvert 0000\rangle + \lvert 1111\rangle$	(2,2,2,2,2,2,2)

of quadripartite pure states are 2, 3 and 5. A product state of two maximally entangled bipartite two-dimensional states is shown as number 4. As expected, the SRV of this state clearly shows that there is no genuine quadripartite entanglement contained in this state.

Let us summarize the most important features of the SRV:

(i) A given state $|\psi\rangle$ is called multipartite entangled iff $r_i \geq 2, \forall i$.

(ii) For a system composed of n parties there are $2^{n-1} - 1$ possible bipartitions.

(iii) Different subsets in the SRV are LOCC incomparable, this means for example that it is not possible to transform a state from $(4,3,2) \rightarrow (3,3,2)$ with LOCC transformations. This results from the LOCC invariance of the Schmidt rank.

(iv) There exists a Russian nesting doll like structure for pure states only.

(v) There is no information about the amount of entanglement contained in the state (maximally entangled, distillable,...).

(vi) There is no information about the usefulness of the state.

(vii) Therefore, the SRV is not a complete but versatile tool to further classify multipartite quantum mechanical systems in higher dimensions and gives a deeper insight into the complexity and structure of entangled states.

As mentioned above, it is not possible to quantify the amount of entanglement of a multipartite and high-dimensionally entangled state with the SRV. Thus we define the maximally entangled pure state with a given SRV as follows:

Definition 1.2.8. Maximally entangled states: Consider a state $\rho(r_A, r_B, r_c) = |\psi_{\text{ABC}}\rangle\langle\psi_{\text{ABC}}|$, which refers to a quantum state ψ_{ABC} with a Schmidt rank vector (r_A, r_B, r_c). In this thesis, such a state is considered maximally entangled if:

(i) For $r_A \geq r_B \geq r_c$ there exists a decomposition of $|\psi_{\text{ABC}}\rangle = \sum_{i=1}^{r_A} \alpha_i |a_i, b_i, c_i\rangle$ such that $\sum_i |\alpha_i| = 1$ and $|\alpha_1| = |\alpha_2| = ... = \left|\alpha_{r_A}\right| = 1/\sqrt{r_A}$.

For an illustrative example of what this definition means, consider state number 2 and 4 of table 1.1. While both states have an SRV = $(3, 3, 2)$, state number two does not fulfill the maximally entangled state requirement mentioned above because there are four α_i coefficients necessary to write this state down. Rewriting to three coefficients is possible but then violates the equality and maximality condition imposed on the coefficients $|\alpha_1| = |\alpha_2| = ... = \left|\alpha_{r_A}\right| = 1/\sqrt{r_A}$. On the other hand, state number 4 does fulfill all the necessary conditions and is thus considered to be a maximally entangled $(3, 3, 2)$ state. The goal of this thesis is to create such a state experimentally, see section 6.

Finally, let us briefly discuss the last question raised in Fig. 1.1. About the usefulness of a given quantum state ρ. By "usefulness", we mean that the state be used in a quantum information protocol (e.g. QKD[5], quantum teleportation, quantum computing, etc.) or for fundamental tests of nature (e.g. Bell test, GHZ-like tests, etc.). In the standard quantum teleportation protocol by Bennett *et.al.*, [24] maximally entangled Bell states are used as EPR channels to transmit the non-classical quantum information. In reality, such pure quantum states rarely exit between two distant parties due to interaction of the two particles with the environment. Therefore, the initially pure state, lets call it $|\varphi\rangle$, decoheres to a mixed state ρ. Now the question arises whether a protocol based on LOCC exists that would enable Alice and Bob to recover the pure state $|\varphi\rangle$ from ρ? Indeed, under certain circumstances such protocols do exist and they are called *distillation* protocols. A simple yet instructive example of such a protocol is given in Ref. [25].

[5]quantum key distribution

Chapter 2

Orbital Angular Momentum of Light

"War es ein Gott der diese Zeichen schrieb?"[1]
— Ludwig Boltzmann *zitiert aus Goethe's "Faust" über Maxwell's Theorie des Elektromagnetismus*

In this chapter, the origin of orbital angular momentum of light is presented. Beginning with Maxwell's equation of electromagnetism in vacuum, the wave-equation and its paraxial approximation are derived. Solutions of this equation are discussed, among them the Laguerre-Gaussian (LG) modes. It is then argued that the helical phase front of the LG beam gives rise to the so-called orbital-angular-momentum of light.

2.1 From Maxwell's Equations to the Paraxial Approximation

The Maxwell equations in SI units and in vacuum are given by:

$$\nabla \cdot \mathbf{E} = 0 \tag{2.1}$$

$$\nabla \cdot \mathbf{B} = 0 \tag{2.2}$$

$$\nabla \times \mathbf{E} = -\frac{\partial \mathbf{B}}{\partial t} \tag{2.3}$$

$$\nabla \times \mathbf{B} = \frac{1}{c^2}\frac{\partial \mathbf{E}}{\partial t} \tag{2.4}$$

with **E**, **B**, c denoting the *electric* and *magnetic* field and the speed of light in vacuum, respectively.

Taking the curl of eq. 2.3 leads to

$$\nabla \times \left(\nabla \times \mathbf{E}\right) = \nabla(\nabla \cdot \mathbf{E}) - \nabla^2 \mathbf{E} = -(\nabla \times \frac{\partial \mathbf{B}}{\partial t}) \tag{2.5}$$

and with Eq. 2.3 & 2.4 follows

$$\nabla^2 \mathbf{E} - \frac{1}{c^2}\frac{\partial^2 \mathbf{E}}{\partial t^2} = 0, \tag{2.6}$$

which is the well known wave equation, and we used the curl of the curl relation. The same procedure also holds for the **B**-Field.

[1] "Was it a god who wrote these signs?", Ludwig Boltzmann quotes Goethe's "Faust" on Maxwell's Theory of Electromagnetism [26]

2.2 The Helmholtz Equation

Let us now derive the Helmholtz equation. Starting at the wave-equation with the Ansatz that the function $\mathbf{E}(\mathbf{r}, t)$ can be written as the product of two functions

$$\mathbf{E}(\mathbf{r}, t) = \mathbf{R}(\mathbf{r})T(t). \tag{2.7}$$

Substituting this into Eq. 2.6 leads to

$$\nabla^2\Big[\mathbf{R}(\mathbf{r})T(t)\Big] - \frac{1}{c^2}\frac{\partial^2\mathbf{R}(\mathbf{r})T(t)}{\partial t^2} = 0 \tag{2.8}$$

$$T(t)\nabla^2[\mathbf{R}(\mathbf{r})] - \mathbf{R}(\mathbf{r})\frac{1}{c^2}\frac{\partial^2 T(t)}{\partial t^2} = 0 \tag{2.9}$$

$$\frac{\nabla^2\mathbf{R}(\mathbf{r})}{\mathbf{R}(\mathbf{r})} = \frac{1}{c^2 T(t)}\frac{\partial^2 T(t)}{\partial t^2}. \tag{2.10}$$

This can only be true if the left and the right hand side above are constant. In general, this constant is named $-k^2$. Rewriting this equation yields

$$\begin{aligned} \frac{\nabla^2\mathbf{R}(\mathbf{r})}{\mathbf{R}(\mathbf{r})} &= -k^2 \\ \left(\nabla^2 + k^2\right)\mathbf{R}(\mathbf{r}) &= 0, \end{aligned} \tag{2.11}$$

and is called Helmholtz equation for the spatial variable $\mathbf{r}$.

2.3 Paraxial Approximation

The paraxial approximation is the basic equation to describe non-tightly focused laser beams. In geometrical optics a paraxial ray encloses only a small angle with the optical axis and is therefore almost parallel. Hence, the field associated with a paraxial beam can be written as

$$\mathbf{E}(\mathbf{r}) = \widetilde{\mathbf{E}}(\mathbf{r})e^{ikz}, \tag{2.12}$$

where the term e^{ikz} denotes propagation in z direction and $\widetilde{\mathbf{E}}(\mathbf{r})$ is varying slowly compared to e^{ikz}. Inserting this into Eq. 2.11 yields

$$\begin{aligned} \left(\nabla^2 + k^2\right)\widetilde{\mathbf{E}}(\mathbf{r})e^{ikz} &= 0 \\ \left(\partial_x^2 + \partial_y^2 + \partial_z^2 + k^2\right)\widetilde{\mathbf{E}}(\mathbf{r})e^{ikz} &= 0 \\ \left(\partial_x^2 + \partial_y^2 + \partial_z^2\right)\widetilde{\mathbf{E}}(\mathbf{r})e^{ikz} + 2ik\partial_z\widetilde{\mathbf{E}}(\mathbf{r}) &= 0. \end{aligned} \tag{2.13}$$

The paraxial approximation is made by neglecting the second derivative with respect to z, assuming

$$\begin{aligned} \left|\partial_z^2\widetilde{\mathbf{E}}(\mathbf{r})\right| &<< k\left|\partial_z\widetilde{\mathbf{E}}(\mathbf{r})\right| \\ \left|\partial_z^2\widetilde{\mathbf{E}}(\mathbf{r})\right| &<< \left|\nabla_\perp^2\widetilde{\mathbf{E}}(\mathbf{r})\right|, \end{aligned} \tag{2.14}$$

with $\nabla_\perp^2 = \partial_x^2 + \partial_y^2$. Thus, the paraxial approximation is

$$\left(\nabla_\perp^2 + 2ik\partial_z\right)\widetilde{\mathbf{E}}(\mathbf{r}) = 0. \tag{2.15}$$

As pointed out by Lax *et al.* [27], this contradicts Maxwell's equations. The Maxwell equation $\nabla \cdot \mathbf{E} = 0$ requires the divergence of the source-free field to vanish, in contradiction to the approximation in Eq. 2.14. This apparent paradox is resolved in the article by Lax *et al.*and beautifully confirmed in a different and very elegant way by Davis [28]. Davis shows that within the framework of vector potentials with Lorentzian gauge condition, that Eq. 2.15 is equivalent in the lowest order without inconsistencies.

2.4 Solutions of the Paraxial Approximation

There exist several different families of solutions of the paraxial approximation. These are classified by their separability and the type of coordinate system used (e.g. Cartesian, Cylindrical, Elliptical, etc.). The main focus here lies on the so-called *Laguerre-Gauss* solutions in cylindrical coordinates. In Appendix A.3 a detailed derivation of the paraxial approximation is given for Cartesian coordinates resulting in the so-called *Hermite-Gauss* solutions.

2.4.1 Laguerre-Gaussian Modes

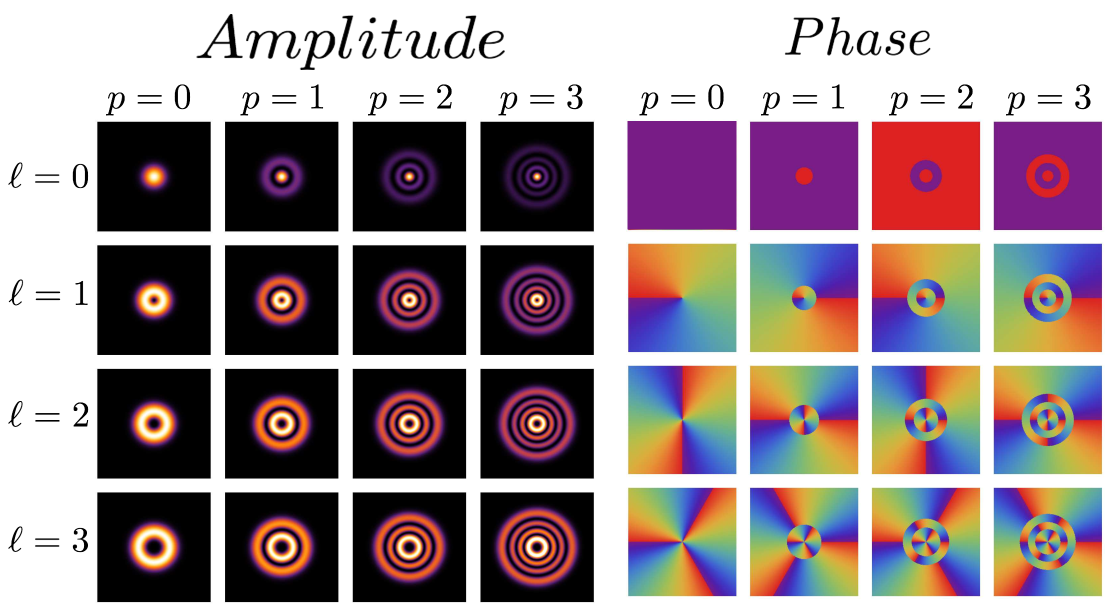

Figure 2.1: Amplitude and phase distribution for different Laguerre-Gaussian modes are displayed. The amplitude is given by the absolute value squared $|u|^2$ and the phase is the argument of the complex function u and is given by $\arg(u)$.

The well known Laguerre-Gaussian solution of the paraxial approximation reads

$$u_{l,p}^{LG}(\rho,\varphi,z) = \frac{C_{l,p}^{LG}}{\sqrt{\omega(z)}}\left(\frac{\sqrt{2}\rho}{\omega(z)}\right)^{|l|} \mathrm{L}_p^{|l|}\left(\frac{2\rho^2}{\omega^2(z)}\right) \exp\left[\frac{-\rho^2}{\omega^2(z)}\right] \exp\left[-il\varphi\right] \exp\left[-i\left(\Phi_{l,p}(z)+\frac{k\rho^2}{2R(z)}\right)\right], \quad (2.16)$$

with the following definitions:

$$\begin{aligned} C_{l,p}^{LG} &= \sqrt{\tfrac{2^{|l|+1}p!}{\pi(p+|l|)!}} \\ \Phi_{l,p}(z) &= (2p+|l|+1)\tan^{-1}\Big(\tfrac{z}{L_F}\Big) \\ R(z) &= z\Big[1+\tfrac{L_F^2}{z^2}\Big] \\ \omega(z)^2 &= \omega_0^2\Big[1+\tfrac{z^2}{L_F^2}\Big] \\ L_F &= \tfrac{k\omega^2(0)}{2} \end{aligned} \tag{2.17}$$

and $\mathrm{L}_p^{|l|}(x)$ denoting the associated Laguerre polynomials defined as

$$\mathrm{L}_p^l(x) = \frac{e^x x^{-l}}{p!}\frac{\mathrm{d}^p}{\mathrm{d}x^p}\Big(e^{-x}x^{p+l}\Big). \tag{2.18}$$

Note for $p = 0$ it follows

$$\mathrm{L}_{p=0}^l(x) = 1 \quad \forall\,\{x, l\}. \tag{2.19}$$

The Laguerre-Gaussian modes form a complete and orthogonal basis in both indices l and p:

$$\int_0^{2\pi} \mathrm{d}\varphi \int_0^{\infty} \rho\, \mathrm{d}\rho\, u_{l,p}^{LG}(\rho,\varphi,z)\Big[u_{l',p'}^{LG}(\rho,\varphi,z)\Big]^* = \delta_{l,l'}\delta_{p,p'}. \tag{2.20}$$

Thus a general solution to the paraxial wave equation can be written as

$$f(\rho,\varphi,z) = \sum_{l,p} \alpha_{l,p} u_{l,p}^{LG}(\rho,\varphi,z), \tag{2.21}$$

with $\alpha_{l,p}$ denoting the expansion coefficients. In Fig. 2.1 some examples of different LG modes are given.

2.5 The Origin of Orbital Angular Momentum

The formal similarity between the paraxial wave equation 2.14 and the Schrödinger equation [29] may suggest that eigenmodes of the angular momentum operator L_z carry orbital angular momentum of $\ell\hbar$ [30]. The linear momentum density of an electromagnetic field is given by the vector $\mathbf{p} = \varepsilon_0 \mathbf{E} \times \mathbf{B}$. Thus a transverse plane wave in z-direction cannot have an angular momentum density $\mathbf{j} = \mathbf{r} \times \mathbf{p}$ in the same direction. In the following we will show that this is not true for Laguerre-Gaussian modes or more general for light beams within the paraxial wave equation with helical wavefront[31, 32, 33], see Fig. 2.2. Since the helical wave front is dominated by $\exp(i\ell\varphi)$ we write

$$u(r,\varphi,z) = u(r,z)\exp(i\ell\varphi). \tag{2.22}$$

Thus the components of the linear momentum $\mathbf{p}$ for a circularly polarized beam are given by (for details see A.6):

$$\begin{aligned} p_r &= \varepsilon_0 \frac{\omega k r z}{(z_R^2+z^2)}|u|^2, \\ p_\varphi &= \varepsilon_0\left[\frac{\omega\ell}{r} - \frac{1}{2}\omega\sigma\frac{\partial|u|^2}{\partial r}\right], \\ p_z &= \varepsilon_0 \omega k |u|^2 \end{aligned} \tag{2.23}$$

where p_r relates to the spread due to divergence of the beam, p_φ describes the rotation of the linear momentum according to the elliptical polarization σ and the orbital angular momentum ℓ while p_z is the linear momentum density in direction of propagation. The rate of change in the azimuthal

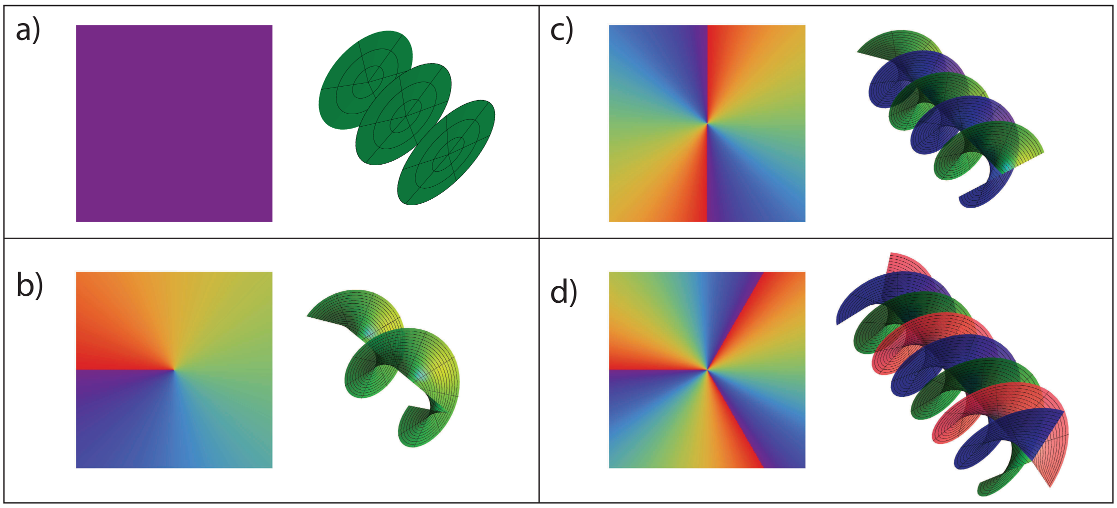

Figure 2.2: Helical phases of different ℓ-values are displayed. Insert **a)** shows a $\ell = 0$ and therefore flat phase. In **b)** one helical twist in a 2π period is shown. Intertwined helices with $\ell = 2, 3$ are shown in c) and d), respectively.

angle of the momentum density Θ with respect to the z-axis is $\frac{\partial\Theta}{\partial z} = \frac{1}{r}\frac{p_\varphi}{p_z}$ and it follows for $\sigma = 0$:

$$\frac{\partial\Theta}{\partial z} = \frac{1}{r}\frac{p_\varphi}{p_z} = \frac{\ell}{kr^2}. \tag{2.24}$$

This result shows the spiraling feature of the linear momentum density for a fixed radius r. However, if the natural divergence (p_r) is taken into account and the propagation along the radius of maximum intensity is calculated (which is also dependent on ℓ), it turns out that the rotation of the linear momentum density is independent of the orbital angular momentum.

The orbital angular momentum density is given by $\mathbf{j} = \mathbf{r} \times \mathbf{p}$ and with the component in direction of z with Eq. 2.23 is given by

$$j_z = \varepsilon_0 \omega \ell \, |u|^2 \, , \tag{2.25}$$

again with $\sigma = 0$. Integration of this quantity over the whole beam and dividing by the energy yields

$$\frac{J_z}{W} = \frac{\int j_z r\mathrm{d}r \, \mathrm{d}\varphi}{\int w_z r\mathrm{d}r \, \mathrm{d}\varphi} = \frac{\ell \int |u|^2 \, r\mathrm{d}r \, \mathrm{d}\varphi}{\omega \int |u|^2 \, r\mathrm{d}r \, \mathrm{d}\varphi} = \frac{\ell}{\omega}. \tag{2.26}$$

Hence, if photons are radiated in units of $\hbar$, their orbital angular momentum also changes with $\ell\hbar$.

Chapter 3

Tools in Linear and Non-linear Optics

In this chapter, the basic tools used in quantum optics are presented. Since the details of the specific elements are well known and described elsewhere, the focus here lies on the mathematical transformations these elements perform on a given input state. The transformations are described in the *creation/ annihilation* operator notation based on the second quantization notation. For simplicity only the considered degree of freedom will be denoted, which in this case is mostly the orbital angular momentum of photons. In this description an orbital angular momentum state of a photon in path a is given by

$$\hat{a}_\ell^\dagger |0\rangle \rightarrow |1_a, \ell\rangle = |\ell\rangle_a \,, \tag{3.1}$$

with $|0\rangle$ denoting the vacuum state and $|1_a, \ell\rangle$ is the Fock-state number state describing 1-photon in mode a with an OAM value of ℓ. Hence, in general

$$\begin{aligned} (\hat{a}_\ell^\dagger)^n |0\rangle &= \sqrt{n+1}\, |n_a, \ell\rangle \\ \hat{a}_\ell |n_b, m\rangle &= \sqrt{n}\delta_{a,b}\delta_{\ell,m} |n_a - 1, \ell\rangle \\ \hat{a}_\ell |0_a, \ell\rangle &= 0 \\ \left[\hat{a}_\ell^\dagger, \hat{a}_m^\dagger\right] &= 0 \\ \left[\hat{a}_\ell, \hat{a}_m\right] &= 0 \\ \left[\hat{a}_\ell, \hat{b}_m^\dagger\right] &= \delta_{a,b}\delta_{\ell,m}, \end{aligned} \tag{3.2}$$

with $[\cdot,\cdot]$ denoting the bosonic commutation relations. Finally, the number operator is defined as $N_\ell(a) := \hat{a}_\ell^\dagger \hat{a}_\ell$ with the property

$$N_\ell(a)(\hat{a}_l^\dagger)^n |0\rangle = n(\hat{a}_l^\dagger)^n |0\rangle \,, \tag{3.3}$$

thus the creation operator is an eigenstate of the number operator.

3.1 Linear Optical Elements for manipulating Photons

Optical elements that respond linearly to the electric field of the incoming light field are called *linear optical elements*. In this thesis the focus is on orbital angular momentum of light, thus we will mainly discuss optical elements operating on the OAM of light. The simplest such element is a mirror.

Definition 3.1.1. Mirror: Suppose an incoming photon $\hat{a}_l^\dagger |0\rangle$ is reflected at a perfect mirror M, then the photon undergoes the following transformation

$$\hat{a}_\ell^\dagger |0\rangle \xrightarrow{M} i\hat{a}_{-\ell}^\dagger |0\rangle \,. \tag{3.4}$$

Thus, the OAM value ℓ flips to $-\ell$ and the photon acquires a phase shift of $i = \exp(i\pi/2)$.

For simplicity, from now on only the transformation of the operators is given.

Definition 3.1.2. Beamsplitter: A general unitary beam splitter with splitting $\{\eta, 1-\eta\}$ acting between two paths a, b, see Fig. 3.1 denoted by $\mathrm{BS}_\eta(a,b)$ reads

$$\begin{aligned} \hat{a}^\dagger_\ell &\xrightarrow{\mathrm{BS}_\eta(a,b)} i\sqrt{\eta}\hat{a}^\dagger_{-\ell} + \sqrt{1-\eta}\hat{b}^\dagger_\ell, \\ \hat{b}^\dagger_\ell &\xrightarrow{\mathrm{BS}_\eta(a,b)} i\sqrt{\eta}\hat{b}^\dagger_{-\ell} + \sqrt{1-\eta}\hat{a}^\dagger_\ell. \end{aligned} \tag{3.5}$$

If not explicitly denoted otherwise, $\mathrm{BS}(a,b)$ is understood to be $\mathrm{BS}_{1/2}(a,b)$ which describes a 50/50 beam splitter.

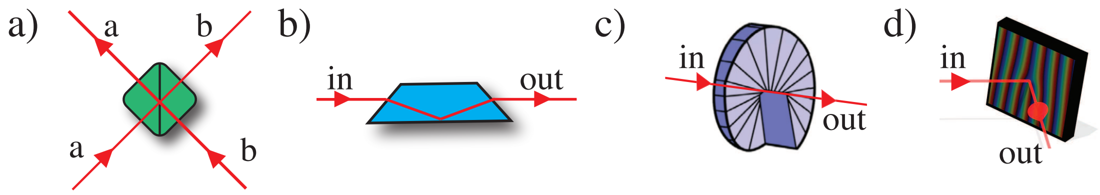

Figure 3.1: Linear optical elements frequently used in quantum and classical OAM setups. **a)** beam splitter: splits up an incoming beam in path a into a superposition of output paths a and b, **b)** Dove prism: changes the sign of the incoming OAM value by (-1) and adds a complex phase according to the OAM value of the incoming photon and the rotation angle of the Dove prism, **c)** a spiral phase plate (SPP) adds a fixed amount of OAM to the incoming beam, **d)** a liquid crystal phase only spatial light modulator (SLM): is capable of changing the incoming beam phase profile arbitrarily.

Definition 3.1.3. Dove Prism: The transformation of a Dove prism $\mathrm{DP}(\alpha)$ at an arbitrary azimuthal rotation angle α is given by

$$\hat{a}^\dagger_\ell \xrightarrow{\mathrm{DP}(\alpha)} i\exp(i2\ell\alpha)\,\hat{a}^\dagger_{-\ell}. \tag{3.6}$$

Definition 3.1.4. Spiral Phase Plate: The spiral phase plate, shown in inset **c)** in Fig. 3.1, is a device to add or subtract OAM from an incoming beam, such that

$$\hat{a}^\dagger_\ell \xrightarrow{\mathrm{SSP}(m)} \hat{a}^\dagger_{\ell+m}, \tag{3.7}$$

holds. Note, these devices usually only support $m \in \mathbb{N}$.

Definition 3.1.5. SLM: With a computer controlled liquid crystal phase-only spatial light modulator (SLM), arbitrary diffraction holograms can be applied to an incoming beam. It thus can be used for arbitrary transformations of the form

$$\hat{a}^\dagger_\ell \xrightarrow{\mathrm{SLM}(\chi)} \hat{a}^\dagger_{\ell+\chi}, \tag{3.8}$$

with χ describing an arbitrary superposition, e.g. $\chi = \gamma_1\ell_1 + \gamma_2\ell_2 + \cdots \gamma_k\ell_k$ and $\sum_i |\gamma_i|^2 = 1$.

Definition 3.1.6. SMF: A single mode optical fiber (SMF) only carries light of a single optical mode efficiently. This is the TEM_{00} mode. Thus the transformation of an SMF reads

$$\hat{a}_\ell^\dagger \xrightarrow{\text{SMF}(m)} \delta(l-m)\hat{a}_m^\dagger, \tag{3.9}$$

thus it only carries the part of the incoming photon which resides in the $\ell = 0$ mode.

Note than an SLM in combination with an SMF can be used to perform arbitrary projection measurements. Apart from the above mentioned elements there exist combinations of these elements exhibiting completely new transformations, e.g. sorting of OAM modes in different paths or cyclic transformations of OAM. These transformations are based on interferometric principles, as explained in detail in section **??**. Here we present the mathematical transformations in brief:

Definition 3.1.7. Mode Sorter: A mode sorter is capable of sorting OAM modes according to their OAM value ℓ parity:

$$\begin{aligned} \hat{a}_\ell^\dagger &\xrightarrow{\text{MS}(a,b)} i\hat{a}^\dagger_{-\ell_{even}} + \hat{b}^\dagger_{\ell_{odd}}, \\ \hat{b}_\ell^\dagger &\xrightarrow{\text{MS}(a,b)} i\hat{b}^\dagger_{-\ell_{even}} + \hat{a}^\dagger_{\ell_{odd}}, \end{aligned} \tag{3.10}$$

hence acting similarly to a polarizing beam splitter.

Definition 3.1.8. Cyclic Transformation: [34] A cyclic transformation (CT) for an element $a_i \in S_k$ reads

$$a_0 \to a_1 \to a_2 \to \ldots \to a_k, \tag{3.11}$$

thus an arbitrary input state with $\ell \in S_k$ is transformed like

$$\hat{a}_\ell^\dagger \xrightarrow{\text{CT}(k)} \hat{a}^\dagger_{\text{mod}(\ell+1,k)}, \tag{3.12}$$

with $\text{mod}(\ell+1,k)$ describing the cycling through all elements in S_k as given by Eq. 3.11.

3.2 Non-Linear Optical Elements for creating Entangled Photon Pairs

In non-linear optics, the interactions of the incoming field with the dielectric polarization of the material become relevant and cannot be neglected. There are several very nice books describing this fascinating topic [35]. In this thesis, non-linear crystals are used for two different purposes. Firstly, the main source of entanglement is a spontaneous parametric down conversion process (SPDC) in a periodically poled potassium titanyl phosphate (ppKTP) crystal. Other non-linear crystals, like BBO, are used in the pump laser source, for details see section 5.2. In an SPDC process, the second order non-linear susceptibility χ^2 leads to the conversion of an incoming pump photon into two down-converted photons called signal and idler. Due to energy and momentum conservation the down-converted signal and idler photon read

$$\begin{aligned} \omega_p &= \omega_s + \omega_i \\ \mathbf{k}_p &= \mathbf{k}_s + \mathbf{k}_i. \end{aligned} \tag{3.13}$$

The second equation is also called the phase matching condition, also see Fig. 3.2. The SPDC process only happens efficiently if the phase matching condition is met. In a non-linear and anisotropic

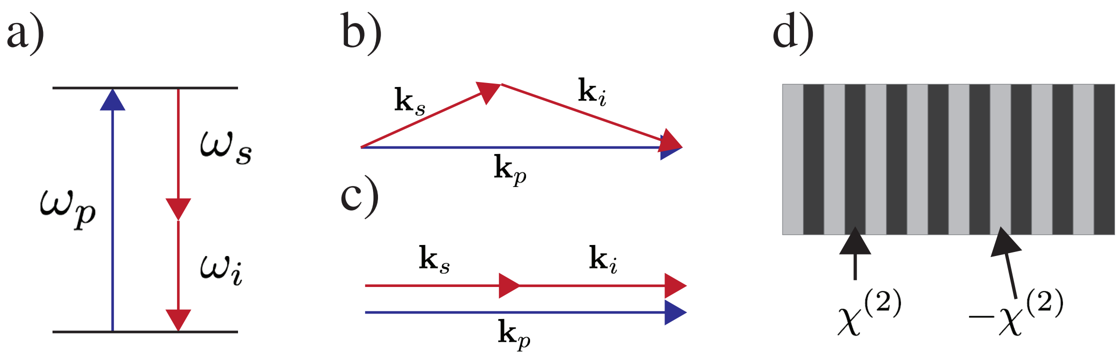

Figure 3.2: Energy and momentum conservation in a SPDC process. Inset **a)** shows the energy splitting of the pump photon into signal and idler photons. In **b)** the phase matching condition is displayed, here shown as matched. Collinear phase matching is shown in **c)**. Part **d)** illustrates an example of a periodically poled crystal.

birefringent crystal, the wave vector **k** is dependent on the direction and polarization of the beam such that

$$\left|\mathbf{k}_j\right| = \frac{\omega n_j(\omega)}{c}, \tag{3.14}$$

with $n_j(\omega)$ denoting the frequency-dependent index of refraction. The phase-matching is called type I if the crystal properties are chosen such that an incoming e polarized light beam is down-converted into two o polarized light beams, while the phase-matching condition is fulfilled in order for the process to happen efficiently. In this thesis, a type II source is used, meaning the crystal is cut such that the phase matching condition is met for an incoming e polarized beam and outgoing o and e polarized beams. More precisely, a periodically poled crystal is used where a quasi phase-matching is achieved by domain inversion, which means that the sign of the nonlinear coefficient changes and an effective phase-matching occurs, see Fig. 3.2. Furthermore, a SPDC process is called collinear if the magnitudes of the the pump photon and the sum of the down-converted photons are equal $\left|\mathbf{k}_p\right| = |\mathbf{k}_s| + |\mathbf{k}_i|$. As shown in [36], OAM is naturally conserved in the SPDC process

$$\ell_p = \ell_s + \ell_i, \tag{3.15}$$

with ℓ_j denoting the pump, signal and idler OAM values. Thus, if the crystal is pumped with a Gaussian beam $\ell_p = 0$, the down-converted state is perfectly anti-correlated $\ell_s = -\ell_i$ and reads

$$|\psi\rangle = \sum_{\ell=0}^{L} c_\ell \Big(|\ell, -\ell\rangle + |-\ell, \ell\rangle \Big), \tag{3.16}$$

with $\sum_{\ell=0}^{L} |c_\ell|^2 = 1$ and the polarization state is omitted for simplicity. The distribution of the c_ℓ coefficients depends on several experimental factors. Miatto *et al.* [37] showed the most important factors are the ratio $\gamma = w_p/w_{s,i}$ between pump and signal, idler waist as well as the ratio $L_R = L/z_r$ between crystal length and the Rayleigh range of the pump beam $z_R = \frac{\pi w_p^2}{\lambda}$. A formula is given

$$c_\ell = \frac{\mathcal{N}}{L_R} \left(\frac{2\gamma^2}{1 + 2\gamma^2} \right)^{|\ell|} \left[\zeta^{|\ell|+1} \Phi_\ell^{L_R,\gamma} - \Phi_\ell^{0,\gamma} \right], \tag{3.17}$$

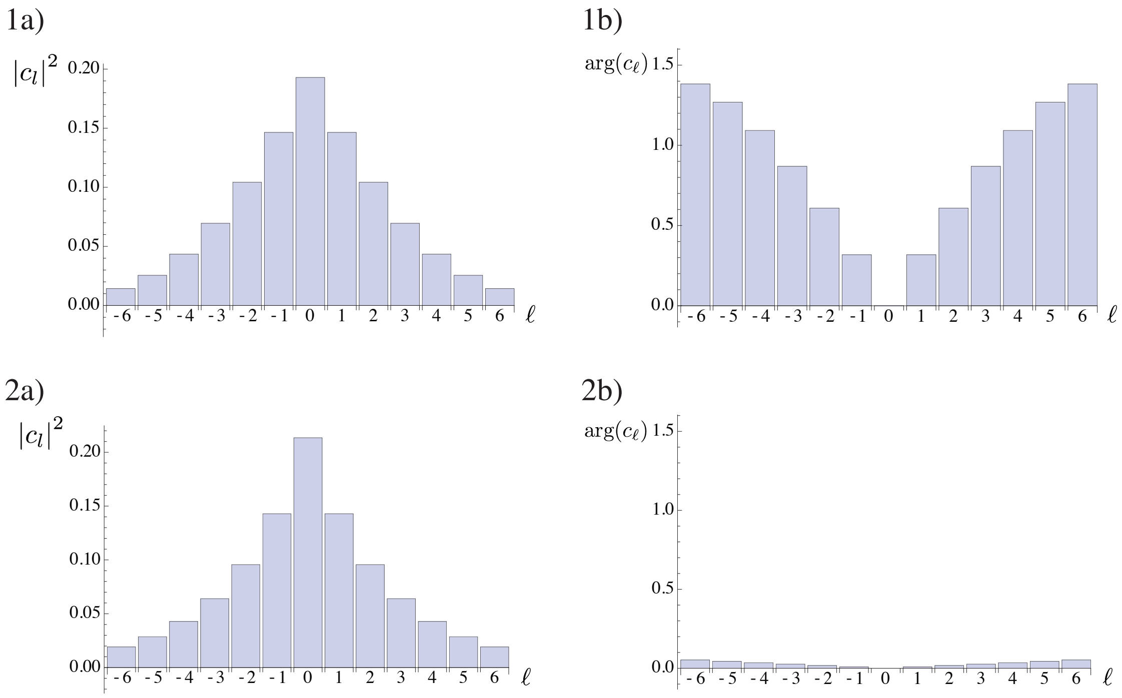

Figure 3.3: Predicted theoretical distribution of the absolute squared values of the coefficients c_ℓ, given by $|c_\ell|^2$ and complex phases $\arg(c_\ell)$ for a down-converted state in a non-linear crystal $|\psi\rangle = \sum_{\ell=0}^{L} c_\ell \Big(|\ell,-\ell\rangle + |-\ell,\ell\rangle \Big)$. Experimentally reasonable values of the ratio between the crystal length and the Rayleigh range of the pump beam L_R with $L_R = 0.0032$ and the ratio of the beam waists of the pump beam and the collection beam γ, with $\gamma = 11$ (in 1) and $\gamma = 1.5$ (in 2). Note, in both cases (1&2) the absolute square values are approximately the same, but the complex phases differ drastically.

with $\Phi_\ell^{L_R,\gamma} = \Phi(-2\gamma^2, 1, |\ell|+1)$ describing the Lerch transcendent function and $\zeta = \frac{i+L_R}{i-2\gamma^2 L_R}$. A plot with reasonable values[1] is given in Fig. 3.3. Both ratios $\gamma_1 = 11$ and $\gamma_2 = 1.5$ give about the same absolute squared value distribution of c_l coefficients. However, there is a significant difference in the complex-phase distribution.

Experimentally, Mair *et al.* [38] showed entanglement of OAM modes for the very first time. Since then a huge effort has been made in increasing the dimensionality. Just recently, OAM-entangled photon pairs in 100-dimensions were confirmed by Krenn *et al.* [8].

[1] $L_R = 0.0032$

Chapter 4

Hong-Ou-Mandel Interference with OAM of Light

The Hong-Ou-Mandel (HOM) effect [10], named after the three physicists who explored this effect, is a two photon interference process. Let us first discuss the classical case. Suppose we have a 50/50 beam splitter as displayed in Fig. 4.1. If two input beams are considered at each port, one would expect to have the four possibilities of outcomes as listed in Fig. 4.1, namely both photons exit in one path (either A or B) and one photon is in path A while the other is in path B. In quantum mechanics, however, this is not the case. With the formalism introduced in section 3.1

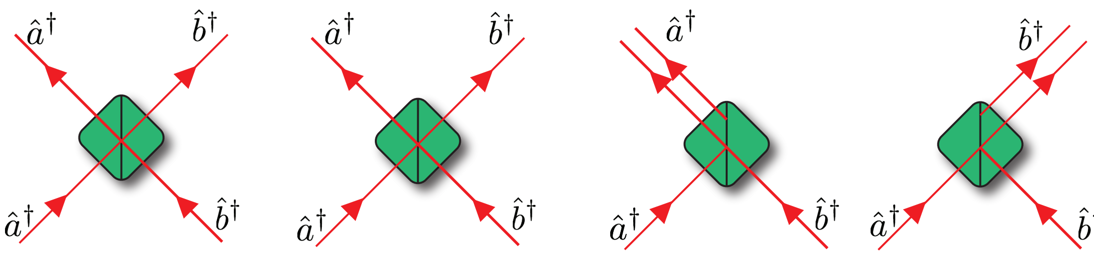

Figure 4.1: Illustration of the HOM effect. Two incoming photons on a beam splitter. Classically one would expect all four possibilities. Quantum mechanically, it turns out that under certain circumstances the photons always stick together. The fundamental reason for that is the bosonic commutation relation.

the problem can be described as follows:

$$\begin{aligned}\hat{a}^\dagger\hat{b}^\dagger|0\rangle \xrightarrow{BS} \frac{1}{2}\left(-\hat{a}^\dagger\hat{b}^\dagger + i\hat{a}^\dagger\hat{a}^\dagger + i\hat{b}^\dagger\hat{b}^\dagger + \hat{b}^\dagger\hat{a}^\dagger\right)|0\rangle &= \frac{i}{2}\left(\hat{a}^\dagger\hat{a}^\dagger + \hat{b}^\dagger\hat{b}^\dagger\right)|0\rangle \\ &= \frac{1}{\sqrt{2}}\left(|2_a,0\rangle + |0,2_b\rangle\right),\end{aligned} \tag{4.1}$$

meaning 2 photons are in mode a or 2 photons are in mode b, but there is **never** one photon in mode a and at the same time one photon in b. Note, that we assumed here[1] $\left[\hat{a}^\dagger, \hat{b}^\dagger\right] = 0$, which assumes the two photons are completely **indistinguishable** and this is not necessarily the case in general. For example, if the two photons carry polarization information, then $\left[\hat{a}_H^\dagger, \hat{b}_V^\dagger\right] \neq 0$ and

[1]Additionally, the state is normalized because $(\hat{a}^\dagger)^n|m\rangle = \sqrt{m+n}\,|m+n\rangle$, and the overall i phase is omitted.

thus the above mentioned state reads

$$\frac{1}{2}\left(i\,|H_a, V_a\rangle + |V_a, H_b\rangle - |H_a, V_b\rangle + i\,|H_b, V_b\rangle\right), \tag{4.2}$$

and thus all the possibilities mentioned in Fig. 4.1 are present and **no** HOM interference takes place. In Eq. 4.1, the final state reads $\frac{1}{\sqrt{2}}\left(|2_a, 0\rangle + |0, 2_b\rangle\right)$ and therefore is a maximally entangled state. As discussed in section 1.2 no entanglement can be created with LOCC operations. Hence, the HOM effect is a non-local effect. In fact, it is a quasi non-local effect since the two photons arriving at the beam splitter have to overlap perfectly in the spatial and temporal domain in order for the HOM effect to occur[2].

Let us discuss a more sophisticated model where the two incoming photons have a spectral bandwidth. Additionally, the two photons must be perfectly overlapped at the beams splitter at the same time. Thus let us use a setup as depicted in Fig. 4.2 a), where one photon is shifted in time with a so-called trombone system. Hence, the incoming photons in modes a, b are now rewritten

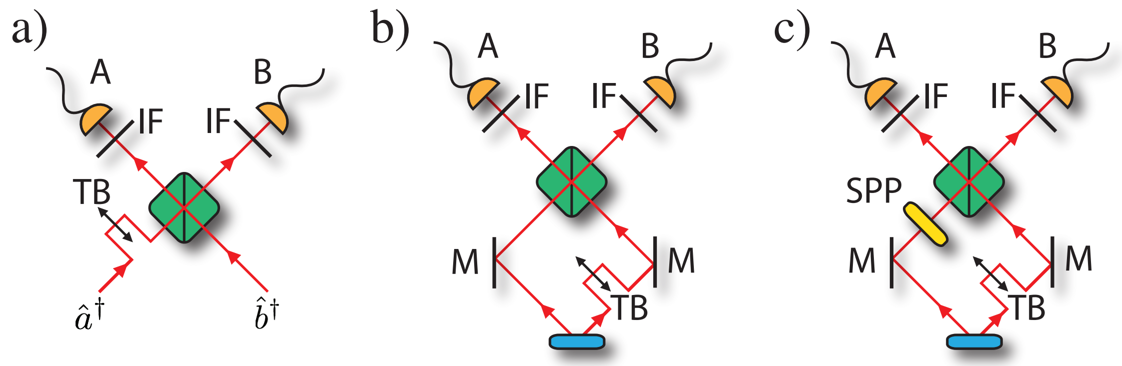

Figure 4.2: Different experimental setups to study the HOM effect. Inset **a)** shows a sketch of the theoretical model studied in the text. **b)** and **c)** depict experimental setups built to study the HOM effect with OAM of light. In this figure, A and B denote detectors, IF are interference filters, TB is the abbreviation for trombone system, SPP is a spiral phase plate and M stands for mirror.

as

$$\hat{a}^\dagger\,|0\rangle \xrightarrow{\text{add bandwidth}} \int \mathrm{d}\omega_1\ \varphi(\omega_1)\hat{a}^\dagger(\omega_1)\,|0\rangle \tag{4.3}$$
$$\hat{b}^\dagger\,|0\rangle \xrightarrow{\text{add bandwidth}} \int \mathrm{d}\omega_2\ \varphi(\omega_2)\hat{b}^\dagger(\omega_2)\,|0\rangle\,,$$

with $\varphi(\omega)$ denoting the spectral distribution of the photons where $\int \mathrm{d}\omega\ |\varphi(\omega)|^2 = 1$. The trombone system, depicted as TB, acts like

$$\hat{a}^\dagger(\omega_1) \xrightarrow{TB} \exp(i\omega_1\tau)\hat{a}^\dagger(\omega_1), \tag{4.4}$$

and thus the state for a reads

$$\int \mathrm{d}\omega_1\ \varphi(\omega_1)\exp(i\omega_1\tau)\hat{a}^\dagger(\omega_1)\,|0\rangle\,. \tag{4.5}$$

The overall state before the beam splitter is thus

$$|\psi\rangle = \int \mathrm{d}\omega_1 \int \mathrm{d}\omega_2\ \varphi(\omega_1)\varphi(\omega_2)\exp(i\omega_1\tau)\hat{a}^\dagger(\omega_1)\hat{b}^\dagger(\omega_2)\,|0\rangle\,. \tag{4.6}$$

[2]The HOM effect can also be used to project onto a maximally entangled state, as will be shown later.

The action of the beam splitter is already discussed in section 3.1. The detailed calculations are given in appendix A.7. The next step is to model the detectors. For now, let us neglect the interference filters and assume perfect detectors with a flat frequency response. Thus, such a detector can be written as

$$\hat{D}_x = \int \mathrm{d}\omega_x\, \hat{x}^\dagger(\omega_x) |0\rangle \langle 0| \hat{x}(\omega_x). \tag{4.7}$$

Thus the expectation value for having one photon in each mode is given by

$$P = \mathrm{Tr}\Big(|\psi\rangle \langle\psi| \hat{D}_a \otimes \hat{D}_a \Big) = \langle\psi| \hat{D}_a \otimes \hat{D}_a |\psi\rangle\,. \tag{4.8}$$

Performing this calculation yields, for details see Appendix A.7

$$P = \frac{1}{2} \int \mathrm{d}\omega_a \int \mathrm{d}\omega_b\ |\varphi(\omega_a)\varphi(\omega_b)|^2 \Big[1 - \mathrm{Cos}((\omega_a - \omega_b)\tau)\Big]. \tag{4.9}$$

The first term in the integral can readily be performed, since $\int \mathrm{d}\omega\ |\varphi(\omega)|^2 = 1$ and hence

$$P = \frac{1}{2} - \frac{1}{2} \int \mathrm{d}\omega_a \int \mathrm{d}\omega_b\ |\varphi(\omega_a)\varphi(\omega_b)|^2\, \mathrm{Cos}[(\omega_a - \omega_b)\tau], \tag{4.10}$$

and the second part is the Cosine transformation of the absolute value squared of the spectral distribution function.

For a Gaussian spectral distribution $\varphi(\omega) = \frac{1}{\sqrt{2\pi\sigma}}\mathrm{Exp}(-\frac{\omega^2}{4\sigma^2})$ the result is

$$P = \frac{1}{2} - \frac{1}{2}\mathrm{Exp}(-\sigma^2\tau^2), \tag{4.11}$$

with σ denoting the standard deviation. A plot of this result is in Fig. 4.3. Thus the shape of the HOM interference curve or HOM dip tells us something about the spectral distribution of the interfering photons.

In most experiments, the two photons are usually from the same SPDC source and are spectrally correlated due to energy conservation, such that the input state reads

$$|\psi\rangle_{\mathrm{SPDC}} = \iint \mathrm{d}\omega_1 \mathrm{d}\omega_2 \Phi(\omega_1, \omega_2) \hat{a}^\dagger(\omega_1) \hat{b}^\dagger(\omega_2) |0\rangle\,, \tag{4.12}$$

with $\Phi(\omega_1, \omega_2)$ describing the joint spectral amplitude (JSA). The JSA is given the product of the pump distribution with the phase matching condition $h(\omega_1, \omega_2)$ of the crystal $\Phi(\omega_1, \omega_1) = \delta(\omega_1 + \omega_2 - \omega_p)h(\omega_1, \omega_2)$, where we assume a delta-like peaked pump laser. After integration over ω_2 and substitution of $\omega' = \omega_1 - \frac{\omega_p}{2}$ yields

$$\int \mathrm{d}\omega' g(\omega') \hat{a}^\dagger(\omega_p/2 + \omega') \hat{b}^\dagger(\omega_p/2 - \omega') |0\rangle\,, \tag{4.13}$$

with ω_p describing the pump beam frequency and we additionally assume a symmetric JSA $h(\omega_1, \omega_2) \to g(\omega')$. With this input state the expectation value to detect two photons simultaneously in A and B is given by

$$P_{\mathrm{SPDC}} = \frac{1}{2} \int \mathrm{d}\omega' \left|g(\omega')\right|^2 \Big[1 - \mathrm{Cos}(2\omega'\tau)\Big]. \tag{4.14}$$

Comparing the previous result given in Eq.4.10 with the SPDC case shows that the cosine transformation differs by a factor of 2. Therefore we expect differently shaped HOM interference curves. For example, the same Gaussian spectral distribution yields for a spectrally correlated source

$$P_{\mathrm{SPDC}} = \frac{1}{2} - \frac{1}{2}\mathrm{Exp}(-2\sigma^2\tau^2). \tag{4.15}$$

Let us compare the two cases with differently shaped spectral distributions of the photons. In the first case where we assumed a factorizable joint spectral amplitude just the two filtering functions need to be known to calculate the HOM dip shape. In the SPDC case the situation is a little more complicated. Typically the phase matching function is a non-linear function of the frequencies ω_i. Thus, an approximation in form of a linearization[3] is performed to derive analytical results. A typical phase-matching function for an SPDC process is a "sinc" function $\mathrm{sinc}(\sigma\omega) = \frac{\sin(\sigma\omega)}{\sigma\omega}$, the respective expectation value of detecting a coincidence between detector A and B is shown in Fig. 4.3.

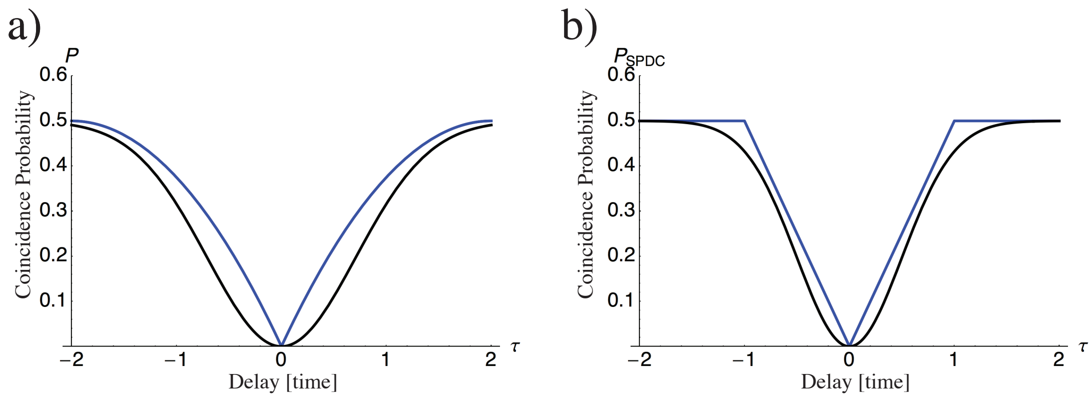

Figure 4.3: Theoretically expected coincidence events detected between detectors A & B according to equations 4.10 and 4.14. For each case, two different spectral distributions are calculated. A Gaussian and a Sinc distribution, where the plot is shown with $\sigma = 1$ in both cases. Note, not only the expected width differs for the correlated case versus the uncorrelated case, but also the shape of the function for non-Gaussian distributions. Inset **a)** shows the uncorrelated case while in **b)** the correlated case with the SPDC source is displayed.

4.1 Different Schemes Exploiting the HOM Effect

So far the OAM degree of freedom of the incoming photons was neglected and it was implicitly assumed that $\ell = 0$ for both photons. In section 3 the state produced in the non-linear crystal was given by

$$|\psi\rangle = \sum_{\ell=0}^{L} c_\ell \Big(|\ell, -\ell\rangle + |-\ell, \ell\rangle \Big), \tag{4.16}$$

where the frequency correlations previously discussed in this section are omitted. For now we will assume that the joint spectrum amplitude (JSA) function is separable and thus the frequency correlations are not present. This assumption will be verified by comparing the expected with the measured dip width, see section 4.3. For the sake of readability we omit the "hat" of the operator and write the OAM value in brackets after the operator $\mathrm{a}^\dagger(\ell)$. Thus the SPDC state now reads, only $\ell \in \{-1, 0, 1\}$ is considered for simplicity

$$|\psi_{\mathrm{SPDC}}\rangle = \Big[\mathrm{a}^\dagger(-1).\mathrm{b}^\dagger(1) + \mathrm{a}^\dagger(0).\mathrm{b}^\dagger(0) + \mathrm{a}^\dagger(1).\mathrm{b}^\dagger(-1)\Big]\,|0\rangle\,. \tag{4.17}$$

[3]Note, the k-vectors in the phase matching function depend on the refraction index $n(\omega_i)$ which depend non-linearly on the frequency. This function $n(\omega_i)$ is linearized in a small region.

Adding a mirror in path A flips the OAM sign in this path (see section 3.1)

$$|\psi_{\mathrm{SPDC}}\rangle \xrightarrow{M(a)} \left[\mathrm{a}^{\dagger}(-1).\mathrm{b}^{\dagger}(-1) + \mathrm{a}^{\dagger}(0).\mathrm{b}^{\dagger}(0) + \mathrm{a}^{\dagger}(1).\mathrm{b}^{\dagger}(1)\right]|0\rangle\,, \tag{4.18}$$

where the overall i phase is omitted. Sending this state onto a beam splitter as depicted in Fig. 4.2 b) yields

$$\begin{aligned}|\psi_{\mathrm{SPDC}}\rangle \xrightarrow{\mathrm{BS}\cdot\mathrm{M(a)}} \frac{1}{2}\Big(& - i\mathrm{a}^{\dagger}(-1).\mathrm{b}^{\dagger}(-1) - i\mathrm{a}^{\dagger}(0).\mathrm{b}^{\dagger}(0) - i\mathrm{a}^{\dagger}(1).\mathrm{b}^{\dagger}(1) \\ & + i\mathrm{b}^{\dagger}(-1).\mathrm{a}^{\dagger}(-1) + i\mathrm{b}^{\dagger}(0).\mathrm{a}^{\dagger}(0) + i\mathrm{b}^{\dagger}(1).\mathrm{a}^{\dagger}(1) \\ & - \mathrm{a}^{\dagger}(-1).\mathrm{a}^{\dagger}(1) - \mathrm{a}^{\dagger}(0).\mathrm{a}^{\dagger}(0) - \mathrm{a}^{\dagger}(1).\mathrm{a}^{\dagger}(-1) \\ & - \mathrm{b}^{\dagger}(-1).\mathrm{b}^{\dagger}(1) - \mathrm{b}^{\dagger}(0).\mathrm{b}^{\dagger}(0) - \mathrm{b}^{\dagger}(1).\mathrm{b}^{\dagger}(-1)\Big)|0\rangle\,.\end{aligned} \tag{4.19}$$

Considering $\ell = 0$ photons only, then the same result as previously calculated occurs. This means that "filtering" the correct terms yields also the HOM type interference. For example, applying an SLM operation of SLM(-1) and additionally using a single mode fiber SMF in both arms A and B results in selecting only modes where $\ell = 1$ in both modes

$$|\psi_{\mathrm{SPDC}}\rangle \xrightarrow{\mathrm{SMF}\cdot\mathrm{SLM}(-1)\cdot\mathrm{BS}\cdot\mathrm{M(a)}} \frac{1}{2}\left(-i\mathrm{a}^{\dagger}(1).\mathrm{b}^{\dagger}(1) + i\mathrm{b}^{\dagger}(1).\mathrm{a}^{\dagger}(1)\right)|0\rangle\,. \tag{4.20}$$

Note that although technically the above state should have $\ell = 0$ everywhere because the photons are physically in this state, here they are written with $\ell = 1$ to make it clear that the interference happened between these modes. The projection into $\ell = 0$ mode with the SLM and the SMF is only to post-select these events. It should be stressed that in any experimental configuration one relies on this kind of selection, also in the $\ell = 0$ case. Therefore, to observe the desired HOM interference the commutator between these two terms $\left[\mathrm{a}^{\dagger}(1), \mathrm{b}^{\dagger}(1)\right]$ must vanish. This is accomplished by overlapping the two photons perfectly in the spatial and temporal domain. The spatial domain is addressed by careful alignment of the incoming beams at the beam splitter, while the temporal domain is dependent on the spectral bandwidth as well as on the arrival time of the two photons at the beam splitter. A trombone system and narrow bandpass filters, as depicted in Fig. 4.2 b), are used to ensure the temporal overlap. This very same procedure also applies to higher order ℓ modes and is demonstrated experimentally, see section 4.3.

In Fig. 4.2 c) another experimental setup is shown. This setup contains an additional spiral phase plate (SPP). For simplicity let us consider here only the $\ell = 0$ modes emitted by the ppKTP crystal. Then the SPP adds an OAM value of $\ell = 2$ in arm A to the state and then we apply the beam splitter operation, thus the state reads

$$\frac{1}{2}\left(-\mathrm{a}^{\dagger}(-2).\mathrm{b}^{\dagger}(0) + \mathrm{b}^{\dagger}(2).\mathrm{a}^{\dagger}(0) + i\mathrm{a}^{\dagger}(-2).\mathrm{a}^{\dagger}(0) + i\mathrm{b}^{\dagger}(2).\mathrm{b}^{\dagger}(0)\right)|0\rangle \tag{4.21}$$

and after another reflection in arm A

$$\frac{1}{2}\left(-i\mathrm{a}^{\dagger}(2).\mathrm{b}^{\dagger}(0) + i\mathrm{b}^{\dagger}(2).\mathrm{a}^{\dagger}(0) - \mathrm{a}^{\dagger}(2).\mathrm{a}^{\dagger}(0) - \mathrm{b}^{\dagger}(2).\mathrm{b}^{\dagger}(0)\right)|0\rangle\,. \tag{4.22}$$

Since only coincidence events between detector A and B are detected, the state can be written as

$$|\chi\rangle = \frac{1}{\sqrt{2}}\Big(|0,2\rangle - |2,0\rangle\Big), \tag{4.23}$$

where the state is properly renormalized. Measuring in the superposition $|0\rangle + |2\rangle$ on both detectors yield a minimum and hence a HOM interference like previously observed is expected. On the contrary, measuring $|0\rangle + |2\rangle$ on detector A and $|0\rangle - |2\rangle$ on detector B yields a maximum, thus resulting in the observation of a HOM interference bump. The expectation value of an operator $\mathcal{P}_{\text{bump}}$ with

$$\begin{aligned}\mathcal{P}_{\text{bump}} &= \frac{1}{4}(|0\rangle + |2\rangle)_A(\langle 0| + \langle 2|)_A \otimes (|0\rangle - |2\rangle)_B(\langle 0| - \langle 2|)_B \\ &= \frac{1}{4}\Big(|00\rangle\langle 00| + |20\rangle\langle 00| + |00\rangle\langle 20| + |20\rangle\langle 20| \\ &\quad - |02\rangle\langle 00| - |22\rangle\langle 00| - |02\rangle\langle 20| - |22\rangle\langle 20| \\ &\quad - |00\rangle\langle 02| - |20\rangle\langle 02| - |00\rangle\langle 22| - |20\rangle\langle 22| \\ &\quad |02\rangle\langle 02| + |22\rangle\langle 02| + |20\rangle\langle 22| + |22\rangle\langle 22| \Big).\end{aligned} \tag{4.24}$$

Thus the expectation value of $\mathcal{P}_{\text{bump}}$ is

$$\langle\chi|\mathcal{P}_{\text{bump}}|\chi\rangle = \frac{1}{2}. \tag{4.25}$$

Note that for a mixed state ρ_χ we would expect

$$\mathrm{Tr}(\rho_\chi \mathcal{P}_{\text{bump}}) = \frac{1}{4}, \tag{4.26}$$

with $\rho_\chi = \frac{1}{2}\Big(|02\rangle\langle 02| + |20\rangle\langle 20| \Big)$. This shows that an expectation value of $\frac{1}{2}$ is indeed a bump with double the expectation value as compared to a mixed state. Additionally, a detailed calculation shows that higher order ℓ terms produced in the SPDC process do not interfere with the derivation shown here. Furthermore, the SPP could take any arbitrary value of ℓ, thus the scheme presented here is a method to create arbitrary states of the from

$$|\chi_\ell\rangle = \frac{1}{\sqrt{2}}\Big(|\ell, 0\rangle - |0, \ell\rangle \Big), \tag{4.27}$$

conditioned on coincidence-events between detector A and B. These states are called $\ell 00 \ell$-states.

4.2 Experimental Setup

The detailed experimental setup is displayed in Fig. 4.4. The central photon source in this thesis is the so-called high-dimensional entanglement photon pair (HDEPP) source, for a detailed characterization and description see section 5.2. Since entanglement is not required for the experiments reported here we omit the details of the source. It is important to know the center wavelength and the FWHM bandwidth of the emitted photons, which is measured to be $\lambda_c = (808 \pm 0.2)$nm and $\Delta\lambda = (7 \pm 0.5)$nm. The average pump power is 360mW of pulsed laser light centered at 404nm. The ppKTP crystal is cut for type II and thus emits horizontally and vertically polarized photon pairs. These pairs are deterministically separated with a polarizing beam splitter (PBS). In order to "erase" the polarization information, a half wave plate (HWP) oriented at 45° is used. To scan for the HOM interference dip, a motorized trombone (TB) system is used. To avoid wave-front disturbances due to propagation, 4f-systems are used in each arm (lenses of the 4f-system are depicted as L6). The spiral phase plate (SPP) add an OAM value of $\ell = 2$ to the transmitting photon. Note, the SPP is only mounted in one experiment. The HOM interference finally occurs at the 50/50 beam splitter (BS). Careful alignment of the incoming beams is crucial to obtain a high visibility. To select and detect certain subspaces of the OAM spectra, a spatial light modulator (SLM) in

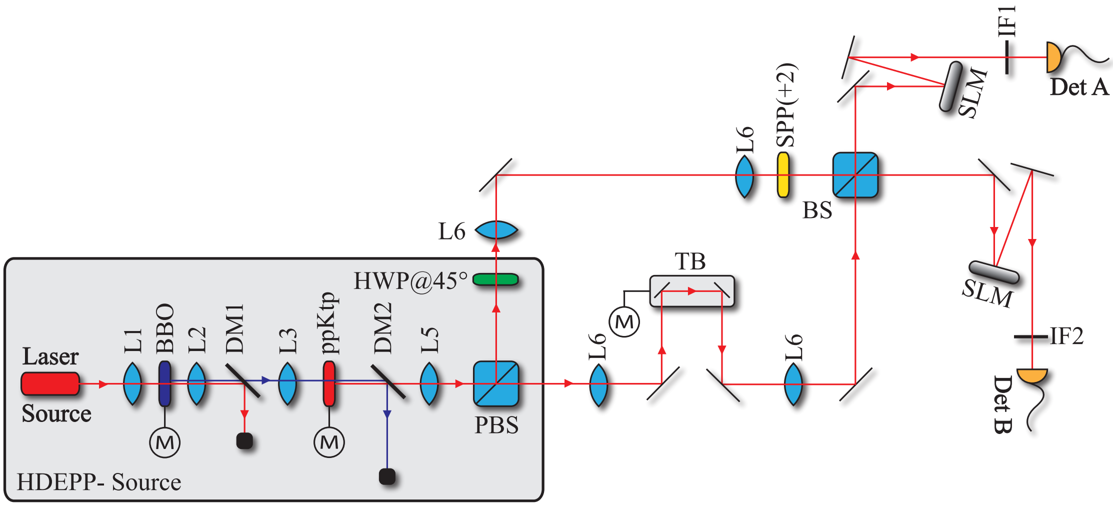

Figure 4.4: Detailed experimental setup. A high-dimensional entangled photon pair (HDEPP) source is used. For details of this source see section 5.2. Lenses annotated with L6 depict 4f-systems to compensate for long distance propagation. The trombone (TB) system is operated with a computer controlled motorized stage. The spiral phase plate (SPP) is only mounted when explicitly mentioned i.e. the last experiment reported here. The spatial light modulators (SLM) in combination with single mode fibers and narrow-band interference filters (IF) build up the detection unit. The photons are finally detected in avalanche photodiodes and coincidence events are recorded in fast counting electronics.

combination with a single mode fiber (SMF) is used. Additionally, narrow band interference filters extend the coherence length of the HOM interference dip. Finally, the SMF guides the projected photons to a single-photon avalanche photodiode (APD). The TTL signal created by the APDs is compared in a home made coincidence logic with a coincidence time window of approximately 1.5ns.

4.3 Data Analyzation and Results

Here the experimental results are presented and the data analyzation procedures used are explained. First an overview of the experimental results is given. The measured data for the first set of experiments is shown in Fig. 4.5. This data represents the results corresponding to the experiment depicted in Fig. 4.2 b) (without SPP inserted). Detailed experimental settings for each measurement result is given in the following:

(i) $\ell = 0$: Two interference filters with $IF_A = 1$nm and $IF_B = 1.2$nm are inserted. Measurement time is 1 second per measurement point.

(ii) $\ell = 1$: Two interference filters with $IF_A = 1$nm and $IF_B = 1.2$nm are inserted. Measurement time is 1 second per measurement point.

(iii) $\ell = 2$: Two interference filters with $IF_A = 1$nm and $IF_B = 1.2$nm are inserted. Measurement time is 10 seconds per measurement point.

(iv) $\ell = 3$: Two interference filters with $IF_A = 1$nm and $IF_B = 1.2$nm are inserted. Measurement time is 1 second per measurement point.

(v) $\ell = 4$: Two interference filters with $\mathrm{IF}_A = 1\mathrm{nm}$ and $\mathrm{IF}_B = 3\mathrm{nm}$ are inserted. Measurement time is 5 seconds per measurement point.

(vi) $\ell = 5$: Two interference filters with each $\mathrm{IF}_A = 1\mathrm{nm}$ and $\mathrm{IF}_B = 1.2\mathrm{nm}$ are inserted. Measurement time is 1 second per measurement point.

The measured visibilities and the corresponding HOM interference widths are displayed in Table 4.1.

Table 4.1: Measured visibilities V and estimated HOM interference dip widths σ. Errors are calculated using Gaussian error propagation with Poissonian distribution of counting statistics.

OAM	Visibility V	σ [mm]
$\ell = 0$	0.845 ± 0.013	$0.16 \pm .01$
$\ell = 1$	0.94 ± 0.014	$0.17 \pm .01$
$\ell = 2$	0.925 ± 0.006	$0.18 \pm .01$
$\ell = 3$	0.944 ± 0.02	$0.16 \pm .01$
$\ell = 4$	0.82 ± 0.03	$0.18 \pm .012$
$\ell = 5$	0.91 ± 0.02	$0.17 \pm .01$

From the theoretical treatment of the HOM interference effect two different dip-widths are expected in principle. The first one according to the spectrally uncorrelated case Eq. 4.11 and the second one the spectrally correlated (SPDC) case. Note, as argued previously narrow-band filtering should suppress the spectral correlations. In order to verify this claim these two theoretical predictions are compared here. The experimental results in Fig. 4.5 are given with respect to the movement of the trombone system in mm. The theoretical treatment on the other hand is units of seconds, thus the time τ is given by $\tau = \frac{x}{c}$ with x giving the position of the trombone system. The two filters with slightly different bandwidths (see Fig. [ref]) result in an effective bandwidth of

$$\sigma_{\text{eff}} = \sqrt{\frac{2{\sigma_1}^2{\sigma_2}^2}{{\sigma_1}^2 + {\sigma_2}^2}}. \tag{4.28}$$

This is the result of comparing the cosine transform of two different functions $\varphi_1(\sigma_1), \varphi_2(\sigma_2)$ in Eq. 4.11 with Eq. 4.10. The measured bandwidth of the two filters are

$$\begin{aligned} \sigma_1 &= 0.3\text{nm} \\ \sigma_2 &= 0.36\text{nm} \\ \sigma_{\text{eff}} &= 0.33\text{nm}, \end{aligned} \tag{4.29}$$

according to the theoretical definition of $\varphi(\omega)$ and note that these values convert to the frequency bandwidth according to

$$\Delta\nu = \frac{c}{\lambda^2}\Delta\lambda \tag{4.30}$$

with $\Delta\nu$, $\Delta\lambda$ denoting the respective σ widths and c is the speed of light in vacuum. Since the dip-width is not dependent on the OAM value ℓ, we do not expect the dip width to vary with higher order ℓ modes. Even though the spectral filtering determines the dip-width it does not affect the theoretically expected visibility. Thus even for a very broad spectrum we expect a visibility equal to 1. This is due to the specific assumption made in the theoretical derivation. For example, taking a non 50/50 beam splitter into account leads to a theoretically expected visibility

$$V = \frac{(1-\alpha)\alpha}{3(\alpha-1)\alpha+1}, \tag{4.31}$$

with α denoting the sorting efficiency of the beam splitter according to

$$\mathrm{BS}(\alpha)\cdot \hat{a}^{\dagger} \rightarrow \sqrt{\alpha}\hat{b}^{\dagger} + i\sqrt{1-\alpha}\hat{a}^{\dagger}. \tag{4.32}$$

Typical values of modern beam splitters with a distinction ratio of 1:100 yields a theoretically expect visibility of $V \approx 0.99$. Additionally, the spatial overlap is assumed to be perfect. This is a fair assumption for HOM interference in fibers for example. Here the HOM interference is taking place in free space. Thus perfect overlap cannot be guaranteed at the beam splitter. The experimentally observed visibilities given in Table 4.1 show a clear trend that higher order ℓ modes result in a higher visibility. For $\ell = 4$, the experiment was performed with a different alignment and thus cannot directly be compared to the other measurements. A possible explanation for this is that the spatial light modulator is acting as a spatial filter for the higher order ℓ modes. Since the transformation of any ℓ mode to the $\ell = 0$ mode depends on the position of the incoming beams to the SLM and the hologram displayed on it. Thus it seems to be reasonable to think of the SLM as a spatial filter for higher order ℓ modes.

The second experiment performed as depicted in Fig. 4.2 c). As explained in the previous section, the inserted spiral phase plate adds an OAM value of $\ell = 2$ to one path. This results in a $\ell 00 \ell$ state with $\ell = 2$

$$|\chi_2\rangle = \frac{1}{\sqrt{2}}\Big(|2,0\rangle - |0,2\rangle\Big), \tag{4.33}$$

conditioned on coincidence events between detector A and B. Given this state, one can observe a HOM interference for specific measurement settings. Two different measurement settings have been used to explore HOM dip and bump interference:

$$\begin{aligned} &\text{Dip-settings:} \quad \text{det A} : |0\rangle + |2\rangle \quad \text{det B} : |0\rangle + |2\rangle \\ &\text{Bump-settings:} \quad \text{det A} : |0\rangle + |2\rangle \quad \text{det B} : |0\rangle - |2\rangle\,. \end{aligned} \tag{4.34}$$

In Fig. 4.6 the HOM dip and bump interference is presented. The observed visibilities are

$$V_{\mathrm{Dip}} = 0.82 \pm 0.03 \tag{4.35}$$

$$V_{\mathrm{Bump}} = 0.66 \pm 0.04 \tag{4.36}$$

with a FWHM width of $W_{\mathrm{Dip}} = (0.3 \pm 0.02)$mm and $W_{\mathrm{Bump}} = (0.32 \pm 0.04)$mm. The values for calculating the visibilities are taken from the fit, for details see appendix A.8. The error bars shown in Fig. 4.5 are due to counting statistics i.e. according to Poissonian statistics given by $\Delta N = \sqrt{N}$ if N is the number of counts. The fitted curve is weighted[4] with the inverse of the variance, given by $1/(\Delta N)^2$. The detailed fit values and the corresponding standard deviations for each plot are given in Appendix A.8. A Gaussian function is used to fit the HOM dip

$$\mathrm{FitF}(x, \Delta x, \sigma) = A - B\exp\left(-\left(\frac{\Delta \mathrm{x} + x}{\sigma}\right)^2\right). \tag{4.37}$$

[4]using the `NonlinearModelFit` function in `Mathematica 9.0`

The visibility is calculated according to

$$V = \frac{\max - \min}{\max + \min}, \tag{4.38}$$

where the max- and min- values are defined as

$$\begin{aligned} \max &= \lim_{x\to\infty} \text{FitF}(x, \Delta x, \sigma) \to A \\ \min &= \lim_{\Delta x, x \to 0} \text{FitF}(x, \Delta x, \sigma) \to A - B, \end{aligned} \tag{4.39}$$

and thus the visibility in terms of the fit values A, B reads

$$V = \frac{B}{2A - B}. \tag{4.40}$$

The error in the visibility is estimated with Gaussian error propagation

$$\Delta f(x, y, \cdots) = \sqrt{\left(\frac{\partial f}{\partial x}\right)^2 \Delta x^2 + \left(\frac{\partial f}{\partial y}\right)^2 \Delta y^2 + \cdots}, \tag{4.41}$$

with $\Delta x, \Delta y, \cdots$ denoting the errors of the respective argument. Hence, for the visibility it follows

$$\Delta V = \sqrt{\frac{4B^2 \Delta \mathrm{A}^2}{(2A - B)^4} + \Delta \mathrm{B}^2 \left(\frac{B}{(2A - B)^2} + \frac{1}{2A - B}\right)^2}. \tag{4.42}$$

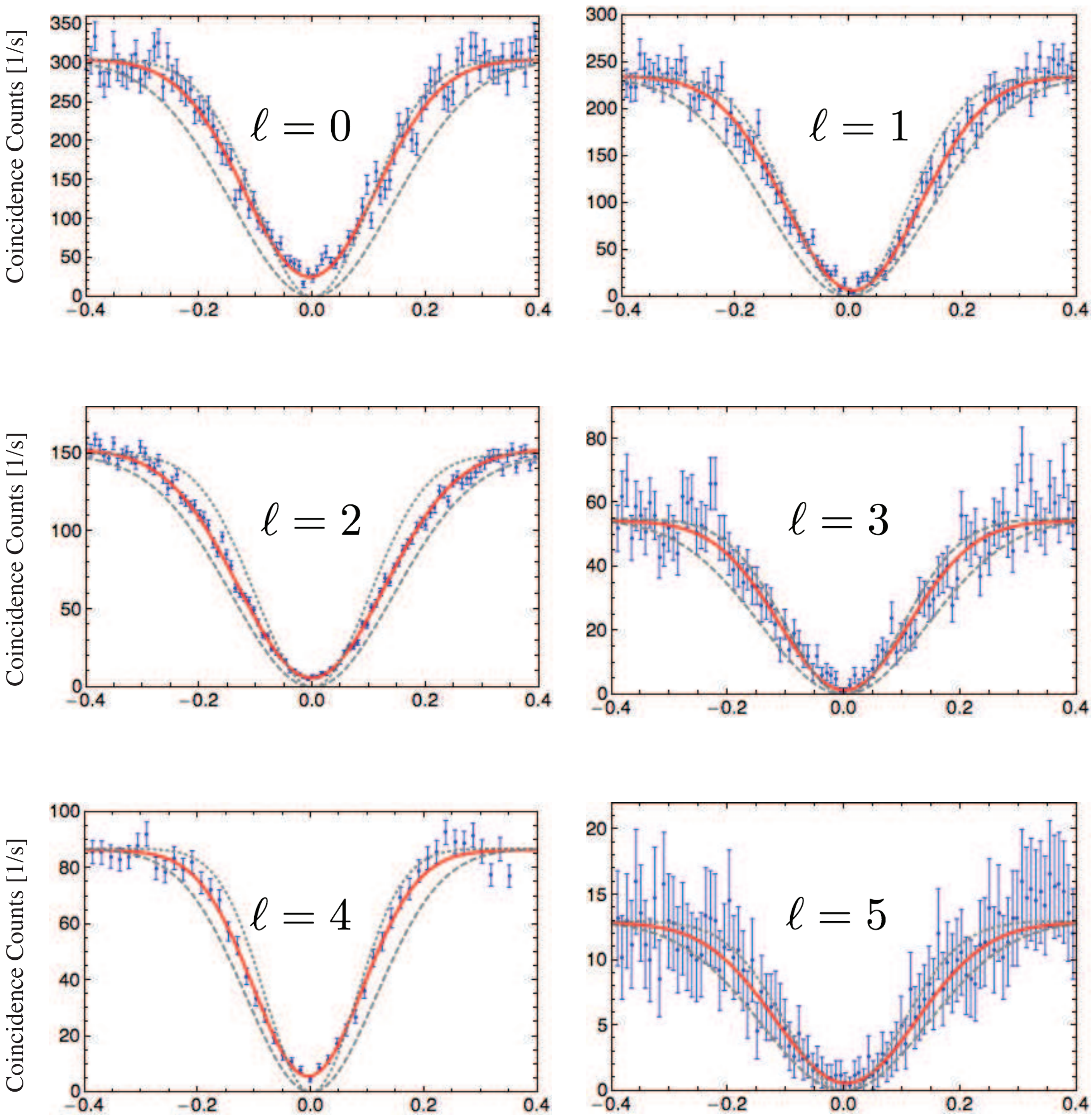

Figure 4.5: Experimental data showing the HOM interference effect for different ℓ-modes. Count rates are displayed per second, actual integration time does vary ($\ell = \{0, 1, 3, 5\} \rightarrow \tau_{\text{int}} = 1s$, $\ell = 2 \rightarrow \tau_{\text{int}} = 10s$ and $\ell = 4 \rightarrow \tau_{\text{int}} = 5s$). The light gray dotted and dashed theory functions correspond to the correlated and uncorrelated dip-width expectation, respectively. Error bars are due to Poissonian counting statistics. The abscissa depicts the position of the trombone system in mm.

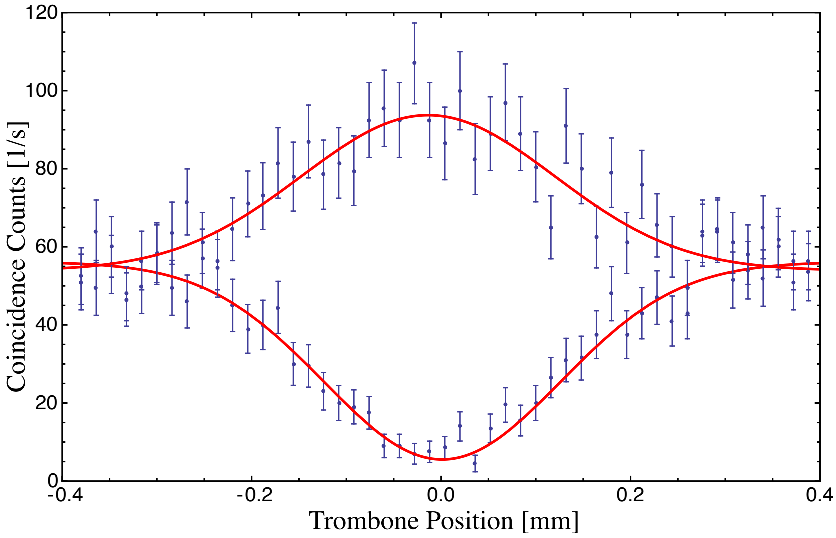

Figure 4.6: Hong-Ou-Mandel dip and bump interference for the $\ell 00\ell$ state with $\ell = 2$. The dip can be observed for a diagonal superposition measurement on both detectors A and B: $|0\rangle + |2\rangle$. The bump can be observed for a diagonal superposition at detector A: $|0\rangle+|2\rangle$, and an anti-diagonal superposition measurement on detector B: $|0\rangle - |2\rangle$. This property arises due to the anti-symmetric $\ell 00\ell$-state with $\ell = 2$: $|\chi_2\rangle = \frac{1}{\sqrt{2}}\Big(|2,0\rangle - |0,2\rangle\Big)$.

Chapter 5

A High-Dimensional Quantum State Router

This chapter is based on a yet unpublished article. A short introduction is given followed by additional information on techniques used.

High-dimensional states as information carriers promise very exciting applications in both classical and quantum information science. In classical communication technology for example, record-breaking data transmission rates of greater than 200 TBit/s have been achieved [39]. In quantum information theory, quantum entanglement plays a central role. For example, in quantum key distribution (QKD) scenarios not only the amount of data being sent can be increased by raising the number of dimensions, but also the degree of security. As shown by Durt *etal* [40] high-dimensional quantum states, so called qudits, offer a higher resistance against errors and at the same time enhance the security in the protocol.

A natural choice as a physical information carrier for high-dimensional information is the orbital angular momentum of light (OAM). The OAM of photons is due to their helical wavefront, typically given by $\exp(i\ell\varphi)$. The number of twists ℓ in a 2π period describes the OAM in units of $\hbar$. In principal this degree of freedom spans a discrete unbounded space which has proven to be very useful in experimental quantum optics as well as in classical optics.

Quantum entanglement of OAM states was shown for the first time by Mair *etal* in 2001 [38]. There has been a huge effort in increasing the dimensionality, until recently even 100 dimensionally entangled photon pairs have been confirmed [8]. In the present work we will show how to route a two photon d-dimensionally entangled state between three parties (Alice, Bob and Carol) with a device called "HD router". Thereby the two-photon ($d = m + n$)-dimensionally entangled state $|\psi\rangle$ is routed into a m-dimensionally entangled state $|\alpha\rangle$ shared between Alice and Bob and a n dimensionally entangled state $|\pi\rangle$ shared between Alice and Carol, see Fig. 5.1 and the following equation

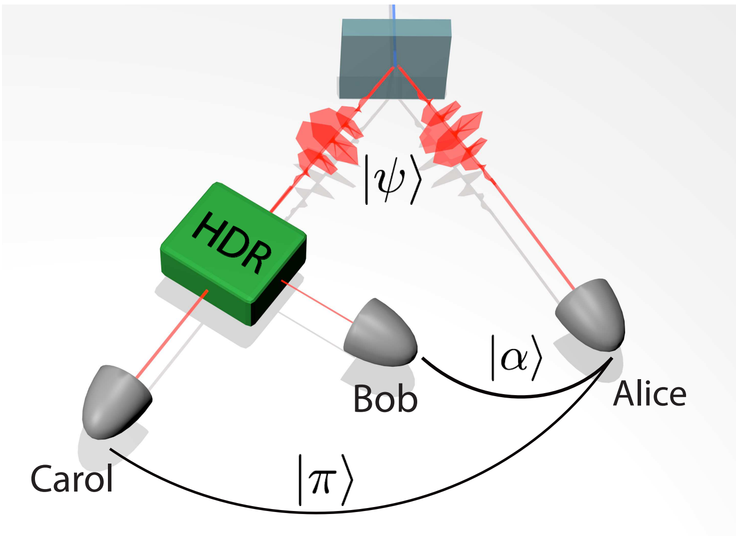

Figure 5.1: A two photon d-dimensionally entangled state $|\psi\rangle$ is routed to three parties. The high-dimensional router (**HDR**) routes the *even/odd* part of $|\psi\rangle$ to the two parties Bob and Carol. Alice and Bob then share the m-dimensional state $|\alpha\rangle$, while Alice and Carol share the n-dimensional state $|\pi\rangle$.

$$|\alpha\rangle = \sum_{\ell \in \mathrm{EVEN}} c_\ell |-\ell, \ell\rangle$$

$$|\psi\rangle = \sum_{\ell=-L}^{L} c_\ell |-\ell, \ell\rangle$$

$$|\pi\rangle = \sum_{\ell \in \mathrm{ODD}} c_\ell |-\ell, \ell\rangle$$

Figure 5.2: Entanglement routing displayed with explicit states. The high-dimensionally entangled initial state $|\psi\rangle$ is routed into two high-dimensionally entangled states $|\alpha\rangle$ and $|\pi\rangle$. As depicted in Fig. 5.1, the two routed states $|\alpha\rangle$ and $|\pi\rangle$ are shared between spatially dislocated participants Bob and Carol.

The basic idea behind the HD router is simple. It is a device capable of sending even ℓ-modes to Bob and odd ℓ-modes to Alice, or vice versa. Now the question that arises is: what happens if one photon of a high-dimensionally entangled two-photon quantum state is sent through this device? Are the non-classical correlations destroyed or weakened? If the entanglement survives this routing operation, is it still high-dimensionally entangled? In this article we will show that a high-dimensional quantum state does indeed survive this routing operation. Additionally, we show a fast switching capability meaning sending *even/odd* or *odd/even* modes to Alice or Bob can be changed quickly and in a well controlled fashion. We also demonstrate a passive control of the HD router to achieve a high distinction ratio between *even/odd* modes over several hours of continuous data sampling. This is especially important if one considers using this device in a multi-photon experiment [41], which heavily rely on high precision and a very stable long-term operation.

5.1 Idea and Physical Principal of Operation

The physical principle of this HD router is based on interferometry. As already shown by Leach *etal* [42], a modified Mach-Zehnder interferometer can be used to sort even and odd modes of OAM. Here the focus is on routing high-dimensionally entangled quantum states, rather than sorting OAM states of single photons. Consider a simple Mach-Zehnder interferometer with a dove prism inserted in each of the two arms (*upper/lower*) with a relative angle of 90° with respect to each other. A dove prism rotates the helical phase-front depending on the orientation angle α and the orbital angular momentum of the incoming photon. The transformation law reads $|\ell\rangle \rightarrow \exp(\pm 2i\ell\alpha)|-\ell\rangle$, with α describing the relative angle between the two dove prisms. The rel-

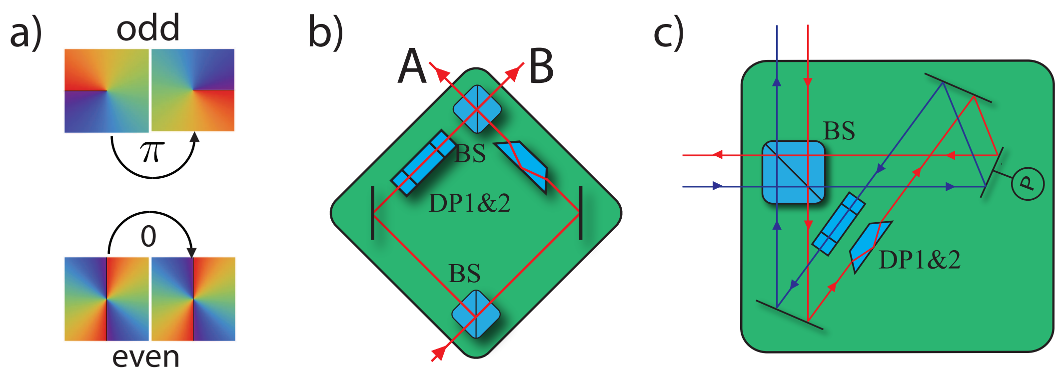

Figure 5.3: Interferometric working principle of the HD router. A Mach-Zehnder interferometer with two Dove-prisms (DP) inserted, shown in **b)**, is used to route *even/odd* parts of the input state $|\psi\rangle$. The relative angle of 90° between the two DPs leads to a π rotation of the phase, shown in inset **a)**. This leads to destructive interference for odd modes and constructive interference (invariant under π rotation) for even modes in output **A**. Inset **c)** shows the actual technical implementation. A folded double-path Sagnac interferometer is used because of the intrinsic stability of this configuration. Additionally, to actively adjust and precisely align the interferometer a computer controlled piezo actuator (P) is mounted on one mirror. This piezo actuator is also used to switch the routing direction of the HD router.

ative angle between the dove prisms in the upper and lower path of the interferometer effectively rotates the phase front of incoming photons with *odd* OAM values by π. Therefore, recombining these two paths results in destructive interference. Even OAM valued photons are effectively invariant under this specific arrangement of dove prisms. Hence, even valued incoming photons exhibit constructive interference. By changing the relative path length by $\pi/2$, the sorting direction can be changed.

However, this also means that for a stable operation of the HD-router the relative path length needs to be very stable. The Sagnac configuration offers such an intrinsically stable design. A Sagnac type configuration is achieved by replacing the output beam splitter of the Mach-Zehnder interferometer with a mirror. Hence, the input beam is split into two beams at the input beam splitter and the two beams are now counter propagating on exactly the same path. Thus path length stability is guaranteed. A double-path Sagnac configuration offers the possibility to insert a dove prism in each path. Although the beams in the double path configuration are not propagating on exactly the same paths, this configuration is still significantly more stable than a Mach-Zehnder configuration. The reason is that for a small separation distance between the two paths, mechanical disturbances are still changing both paths approximately in the same way. Hence, path length fluctuations due to mechanical stresses or vibrations cancel out. As shown in Fig. 5.4 (Setup B) a folded double path Sagnac configuration is used. This special folded design offers two advantages. First, mirrors work more efficiently for smaller enclosed angles. Note, in this configuration it is necessary to use at least three mirrors, since a two mirror configuration does not lead to a double path geometry as shown in Fig. 5.4. Second advantage is that one of the mirrors could be replaced with a reflective spatial light modulator (SLM) to add additional transformations on the OAM degree of freedom. Since very high stability is a crucial requirement of the HD router, a piezo actuator (P) is mounted on one of the mirrors, see Fig. 5.4. Changing the voltage of the piezo actuator slightly changes the angle and thus the relative path length. This feature can now be used for passive stabilization and precise alignment to achieve a very high distinction ratio between even and odd modes. Furthermore, changing the relative path length of the interferometer by $\pi/2$ switches the output configuration from *even/odd* to *odd/even* configuration. This feature is used to demonstrate the fast and precisely controlled switching capability of the HD router.

5.2 Experimental Realization

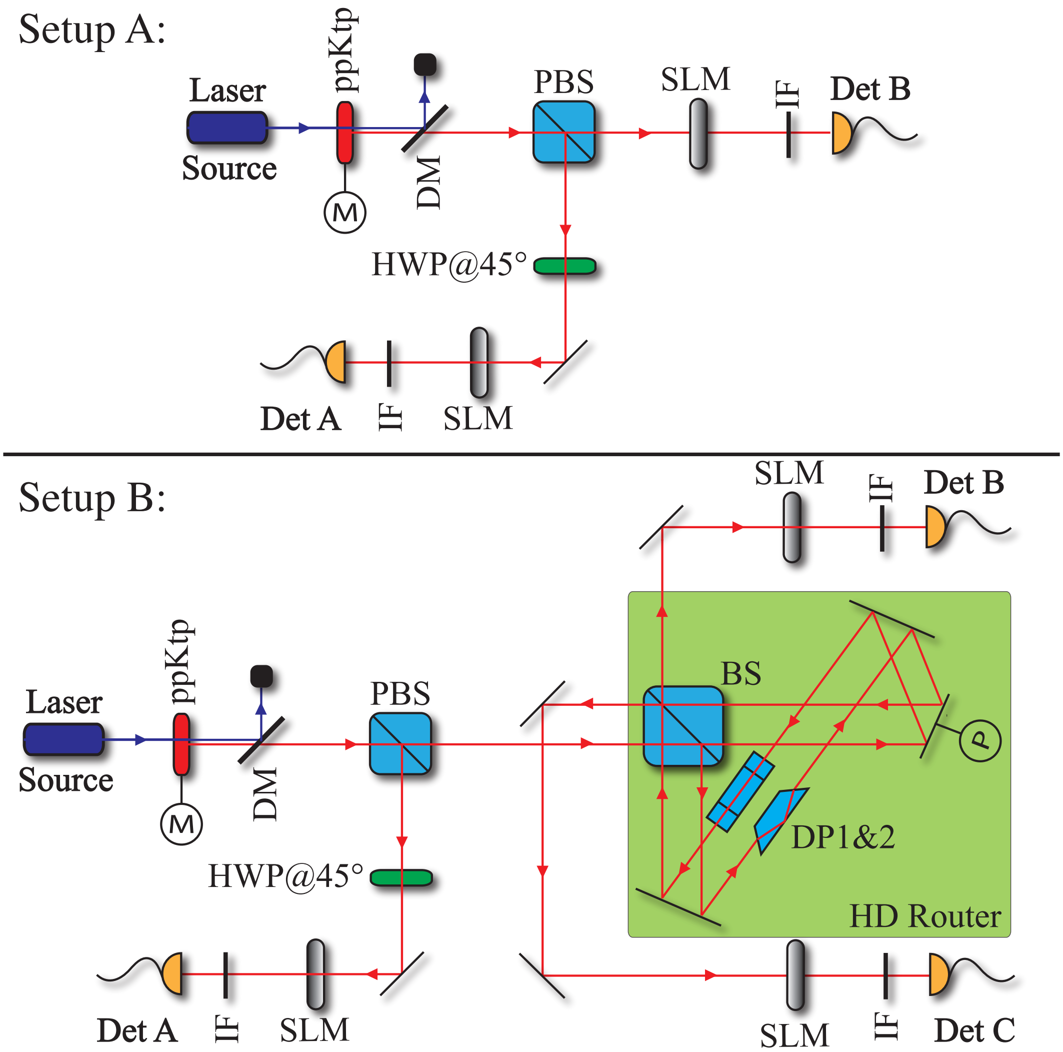

Figure 5.4: Setup A shows the detailed experimental setup for verifying a high-dimensionally entangled input state $|\psi\rangle$. In setup B the HD router is placed into path B to demonstrate high-dimensional entanglement routing. A pulsed laser source operating at 404nm pumps a non-linear ppKTP crystal, type II collinearly phase matched, to produce high-dimensionally entangled two-photon states at a wavelength of 808nm. A dichroic mirror (DM) passes the 808nm photons to a polarizing beam splitter (PBS), where the photon pairs are deterministically separated. The HD router is displayed in the green shaded region. Spatial light modulators (SLM) in combination with single mode fibers and single photon detectors are used to measure the photonic quantum state. With this measurement scheme only projective measurements can be performed. Interference filters (IF) ensure a narrow bandwidth.

Two different experimental setups are used in this work. Setup A displayed in Fig. 5.4 is used to demonstrate a high-dimensionally entangled input state $|\psi\rangle$. In setup B the high-dimensional entanglement router is implemented to verify the proposed routing operation. In order to create high-dimensionally entangled photon pairs, a periodically poled potassium titanyl phosphate (ppKTP) crystal, cut for Type II phase matching, is used. The laser source consist of a pulsed Ti:sapph laser with 140fs pulse length and 80 MHz repetition rate operating at a wavelength of 808nm. A second harmonic generation non-linear process in a beta barium borate (BBO) crystal produces the 404nm laser light. The average power at the 1mm thick ppKTP crystal is 360mW with a beam waist of approximately 240μm. The beam waist is chosen such that the distribution of OAM values is very broad, see Fig. 5.6. Note, the width of the distribution not only depends on the pump beam waist, but also on the collection beam waist given by the detection system.

In order to fulfill the collinear phase-matching condition, the crystal is constantly kept at 120.1°C. The two collinearly propagating entangled photons are deterministically separated with a polarizing beam splitter. The reflected photon A is Alice's photon and thus propagates directly to the detector. The detection system consists of a spatial light modulator, a single mode fiber and a single photon detector. This detection system is only capable of performing projective measurements. To understand this fact, suppose we have an incoming photon with OAM value $\ell = 1$. To measure this photon, the conjugated hologram (in this case $\ell = -1$) is displayed on the SLM to project this photon onto the fundamental Gaussian mode $\ell = 0$. Only the fundamental Gaussian mode can efficiently propagate in a single mode optical fiber to the single photon detector. Thus, only projections displayed at the SLM can be measured. The spatial light modulator is polarization sensitive and only operates on horizontally polarized photons, hence a half-wave-plate (HWP) oriented at 45° rotates the vertically polarized photon A.

In setup B, the HD routing device is inserted in beam path B. Thus path B is split into two paths B and C. The HD router is realized as a folded double-path Sagnac interferometer with two dove prisms inserted. To adjust the sorting efficiency (*even/odd*) with high precision, a piezo actuator (P) is mounted on one of the mirrors. Thus, computer controlled recalibration of the HD router is possible by simultaneously measuring $\ell = 0$ coincidences between detector A-B and A-C while maximizing one of these coincidence counts with the piezo actuator. Additionally, the piezo actuator also enables automated switching between routing directions.

5.3 High-Dimensional Entanglement Verification

First, we verify the entanglement dimensionality of the input state $|\psi\rangle$. In order to prove high-dimensional entanglement, a fidelity witness developed in [43] is used. The fidelity is calculated between a theoretically expected d-dimensional entangled target state $|\varphi_d\rangle = \sum_{\ell=-L}^{L} c_\ell |-\ell, \ell\rangle$ and the measurement data ρ_M, with $d = 2L + 1$. If this fidelity exceeds a certain bound $\mathcal{B}(d)$ for a d-dimensional entangled state, then the measurement data can only be explained with a $d + 1$ dimensional entangled state. As theoretically predicted in section 3.2 and shown in Fig. 5.6, the correlations of the measured states shown in the computational basis are unequally distributed. The peaked distribution of the OAM values ℓ directly shows the unequal amplitudes c_ℓ for different ℓ values. Thus, it seems advantageous to find a target state $|\varphi_d\rangle$ which is close to the observed distribution. On the other hand, the d-dimensional entanglement bound $\mathcal{B}(d) = \sum_{i=0}^{d-1} \lambda_i$ is dependent on the Schmidt coefficients λ_i of the target state $|\varphi_d\rangle$. Note, the Schmidt coefficients are sorted such that $\lambda_0 > \lambda_1 > ... > \lambda_{d-1}$. Hence, always the smallest Schmidt-coefficient is neglected in the entanglement bound $\mathcal{B}(d)$. Since the size of the smallest Schmidt coefficient is directly connected to the smallest probability amplitude in the target state, this entanglement bound $\mathcal{B}(d)$ approaches one as the probability to observe a high OAM value ℓ goes to zero. Therefore, to find the optimal balance we define a parameter $\xi = F_{exp} - \mathcal{B}(d)$ measuring the distance between the experimental fidelity $F_{exp} = \mathrm{Tr}[|\varphi_d\rangle\langle\varphi_d|\rho_M]$ and the entanglement bound $\mathcal{B}(d)$. By maximizing ξ we find the entanglement dimensionality d represented by the measured density matrix ρ_M. From the definition of F_{exp} it can be seen that only the theoretically expected density matrix elements have to be measured. As explained in the previous section, our measurement scheme only allows us to perform projective measurements. This means we decompose all the necessary high-dimensional measurements into two-dimensional subspace measurements. Diagonal elements can be measured directly while the off-diagonal elements require 16 two-dimensional projective measurements, for details see Appendix A.9 & A.10. The entanglement dimensionality verification for the input state $|\psi\rangle$ yields at least 10-dimensional entanglement. The detailed estimated values are given in table 5.1. Thus this 10-dimensional entanglement source is perfectly suited to test the HD router.

5.4 Bipartite High-Dimensional Entanglement Source

In this section additional experimental details about the high-dimensional entanglement source are presented. The experimental results of this thesis show complex valued coefficients c_ℓ for the OAM distributions in various different experimental setups. As argued in the theory section 3.2, the pump beam vs collection beam waist ratio γ could cause such complex phases. We will show, however, that this explanation does not fit with our experimental results. Additional evidence comes from the fact that no complex phases were observed in another high-dimensional bipartite entanglement source with the same experimental ratio of beam waists. The two main differences between these two experimental setups are that a pulsed source and an elliptical pump beam was used in our case. In the following section the elliptical-Gaussian pump waist will be discussed. As depicted in Fig. 5.4 and explained in section 5.2, a pulsed Ti:sapph laser with 140fs pulse length and 80 MHz repetition rate operating at a wavelength of 808nm is used to pump an SHG process. The spatial profile of this up-converted beam is of the form of an elliptical-Gaussian shape, for details see Appendix A.11. This ellipticity may cause problems in the down-converted spectrum, more precisely in the complex phase of the c_ℓ coefficients in the down converted state. The reconstructed density matrix of a 15 dimensional measurement is shown in Fig. 5.5 a) (for details see Appendix A.12). Note, only the theoretically expected non-zero elements of the density matrix are displayed. The theoretically expected density matrix for $\gamma = 11$ and $L = 0.032$ is depicted in inset b). The L value is determined by experimental parameters and chosen to match our setup. The γ ratio is chosen such that the absolute values of the measured density matrix and the predicted density matrix match. Although the absolute values match, the real and imaginary part of the density matrix do not. Thus the complex phases are most likely not due to the γ-ratio, describing the ratio between beam waist and collection waist. For the purpose of this thesis the complex phases are actually not relevant, because the entanglement measures developed here are not sensitive to complex phases. In fact, only the absolute values matter for the entanglement witnesses used here. To date, the origin of these surprising complex phases has not been understood. A numerical simulation of the SPDC process involving an elliptical pump beam could help to further understand this issue.

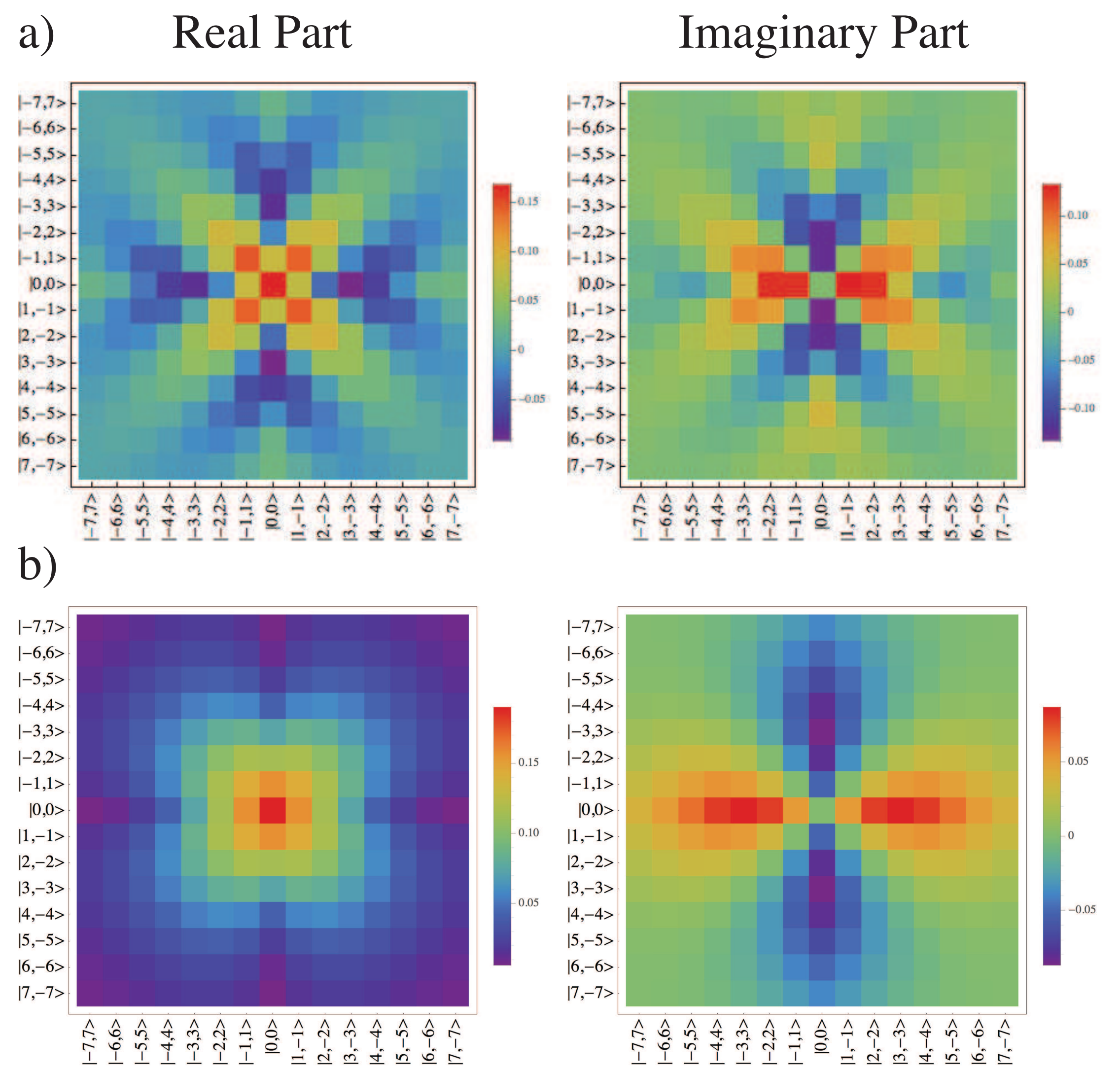

Figure 5.5: Inset a) shows the experimentally measured density matrix of a high-dimensionally entangled state created in a non-linear process in the ppKtp crystal. Only the theoretically expected elements are displayed. Figure b) depicts the theoretical prediction for a γ ratio between pump and collection beam waist of $\gamma = 11$, and the ratio between crystal length and Rayleigh range of the pump beam $L_R = 0.0032$ according to section 3.2. The γ ratio has been chosen such that the absolute values of the theoretical predicted density matrix and the experimentally measured one matches.

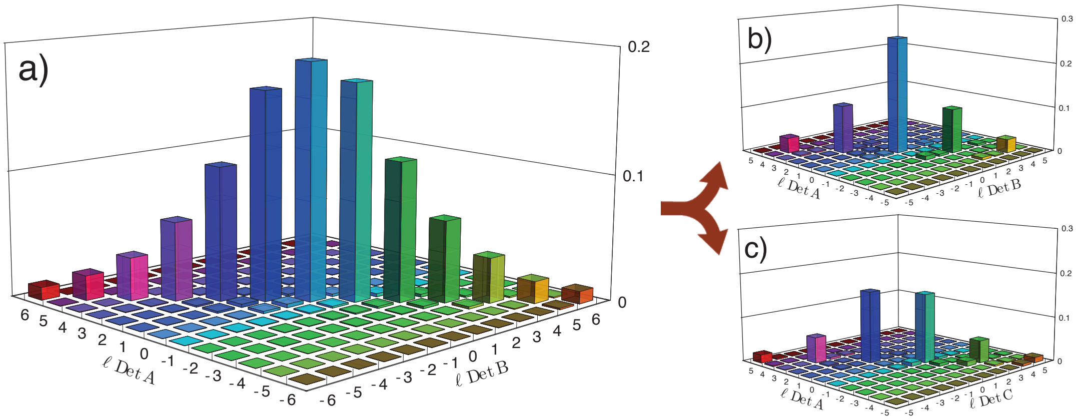

Figure 5.6: Correlation matrices showing the OAM of one photon with respect to the OAM of the other displayed in the computational basis. Inset **a)** shows the correlations measured for the input state $|\psi\rangle$. Inset **b), c)** shows the correlation measurements for the $|\alpha\rangle, |\pi\rangle$ states, respectively. The *even/odd* part of the input state $|\psi\rangle$ is routed to Bob and Carol. These probabilities are directly proportional to the diagonal elements of the states $|\psi\rangle, |\alpha\rangle$and$|\pi\rangle$.

5.5 Experimental Results

Table 5.1: Measured fidelity F_{exp} and estimated entanglement bounds $\mathcal{B}(d)$. Errors are calculated using Monte Carlo simulation with Poissonian distribution of counting statistics.

State	F_{exp}	Bound $\mathcal{B}(d)$	Dimensionality d
$\|\psi\rangle$	0.692 ± 0.003	0.649	10
$\|\alpha\rangle$	0.937 ± 0.004	0.843	5
$\|\pi\rangle$	0.956 ± 0.004	0.898	6

Passing the input state through the HD router yields two states, the $|\alpha\rangle$ state containing only *even* modes and the $|\pi\rangle$ state containing only *odd* modes. The $|\alpha\rangle$ state with the *even* modes is shared between Alice and Bob. Estimating the entanglement dimensionality of this states results in at least 5-dimensional entanglement. The $|\pi\rangle$ state shared between Alice and Carol containing only *odd* modes is at least 6-dimensionally entangled, see table 5.1 for details.

The presented results give rise to an immediate question. How can a 10-dimensionally entangled input state be split up into a 5 and 6 dimensionally entangled state? The answer is that the input state is very close to the bound of being 11 dimensionally entangled. Additionally, the HD router acts like a filter for *even/odd* modes. This means the cross talk between *even/odd* modes is lowered and therefore the visibility in the respective measurements increases. Long term measurements carried out over 39 hours of continuous fidelity measurements are shown in Fig. 5.7. Both states are well above the entanglement bound for their respective entanglement dimensionality. During the 39 hours, the HD router is calibrated every 26 minutes with the piezo crystal to ensure a high visibility in sorting the *even/odd* modes. The results of the first measurements were taken to estimate the optimal target state $|\varphi_d\rangle$. The following fidelities are computed with respect to this first optimal target state. Although the HD router is continuously re-calibrated, the experimental fidelities decrease steadily. At the same time, the count rates in the correlation matrix measurement decrease. The reason for this is gray tracking of the ppKTP crystal over the 39 hours

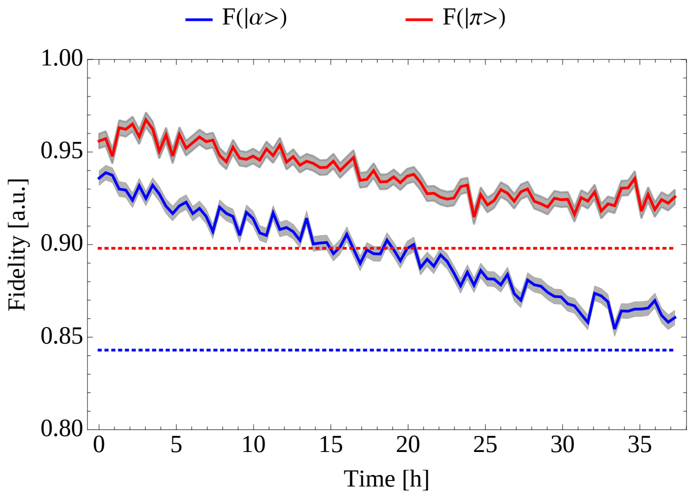

Figure 5.7: Long term measurement of the experimental fidelity F_{exp}. The straight lines represent the respective dimensionality bound. The shaded area displays the error from counting statistics. This error is simulated via a Monte Carlo simulation with Poissonian statistics.

measurement time. This also affects the higher order OAM mode correlations and thus lowers the experimental fidelity over time.

Finally we report the switching capability of the HD router. By changing the relative path length of the interferometer with the piezo crystal it is possible to choose whether Bob or Carol receive *even* or *odd* modes and thus the $|\alpha\rangle$ or the $|\pi\rangle$ state. In Fig. 5.8 the recorded coincidence counts for a $|0\rangle + |2\rangle$ superposition of OAM values are displayed. Every point corresponds to an integration time of 5ms, thus the coincidence counts are displayed in counts/(5ms). The elapsed time between two measurement points is 31ms. The piezo motor is programmed such that it switches back and forth between two voltages ($V_1 = 31.5V, V_2 = 51.4V$). The limitation on the switching time here is mainly due to low count rates. The average visibility of the switching process is 0.97 ± 0.02. In summary, we have reported the development of a high-dimensional quantum

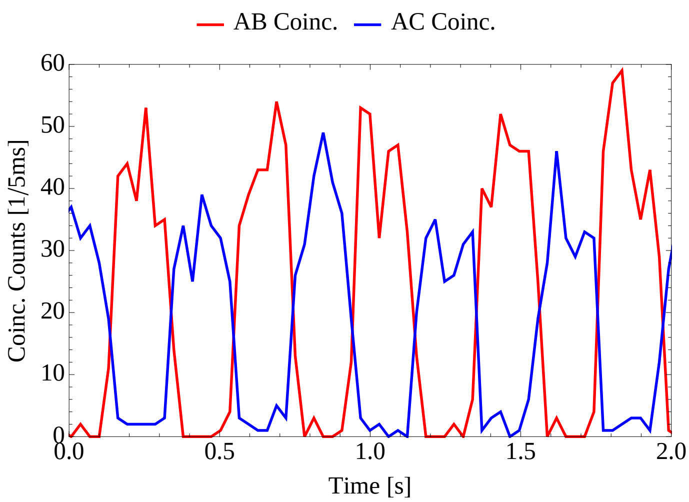

Figure 5.8: Switching of *even/odd* modes via changing the phase in the interferometer. Here the coincidence counts of a $|0\rangle + |2\rangle$ superposition of OAM values are displayed.

state router. We showed that a two-photon high-dimensionally entangled input state can indeed be routed to three spatially different locations while maintaining its high-dimensional non-classical correlations. Due to its intrinsic stable design as a folded double-pass Sagnac-type interferometer with passive stabilization, the HD router is capable of routing high-dimensional quantum states over several days without realigning the optical system. This is especially important for multi-partite and high-dimensional entanglement experiments. Furthermore, the switching capability of the HD router was demonstrated. The switching frequency is only limited by the signal strength and the phase-shifting device.

Chapter 6

Experimental Creation of a (3,3,2) Entangled State

This chapter is largely based on a recently published article by Malik *et al.* [41]. The idea to create a (3,3,2) high-dimensional multi-partite entangled state arose in the process of developing an experimental setup to create a 3-dimensional GHZ state. `Melvin`, a computer algorithm developed by Krenn *et al.* [44] found several different experimental setups to create higher-dimensional multi-partite entangled states, among them a (3,3,2) entangled state.

6.1 Physical Principal of Operation

In our experiment, we aim to create a state which has the form

$$|\Psi\rangle_{332} = \frac{1}{\sqrt{3}}[\,|0\rangle_A\,|0\rangle_B\,|0\rangle_C + |1\rangle_A\,|1\rangle_B\,|1\rangle_C + |2\rangle_A\,|2\rangle_B\,|1\rangle_C\,]. \tag{6.1}$$

Notice that the first two photons, A and B, live in a three-dimensional space, while the third photon, C, lives in a two-dimensional space. The dimensionality of this state is given by a vector of three numbers $(3, 3, 2)$. Specifically, these are the ordered ranks of the single particle reductions of the state density operator:

$$\mathrm{rank}(\rho_A) = 3, \qquad \mathrm{rank}(\rho_B) = 3, \qquad \mathrm{rank}(\rho_C) = 2, \tag{6.2}$$

where $\rho_i = \mathrm{Tr}_{\bar{i}}\,|\Psi\rangle_{332}\,\langle\Psi|_{332}$ is the state of system $i \in (A, B, C)$. Only certain combinations of these three ranks are allowed, leading to a rich structure of possible asymmetric high-dimensional multipartite entangled states[45]. States such as these lie at the frontier of quantum entanglement and have not yet been realized in the laboratory. Their experimental creation would extend this frontier, allowing fundamentally new types of entanglement to be investigated in the laboratory.

The entanglement of three photons was first achieved by combining two pairs of polarization-entangled photons in such a way that it became impossible, even in principle, to know which pair one of the detected photons belonged to[46]. The workhorse of such experiments is the polarizing beam-splitter (PBS), which was designed to separate a light beam into its horizontal and vertical polarization components. Interestingly, a PBS can also be used to mix the polarizations of two input photons from independent polarization-entangled pairs in such a manner that an output photon contains polarization components from both input photons. In this manner, information about their origin is erased, producing a four-photon, two-dimensional GHZ state[46]. The largest such state created thus far used seven PBSs to entangle eight photons in their polarization[47].

In order to manipulate the high-dimensional space of OAM, one would need a device akin to the PBS, but operating on a photon's spatial wavefunction as opposed to its polarization.

In our experiment, we use the high-dimensional entanglement router as a OAM parity sorter. We use this device as a two-input, two-output "OAM beam splitter" that reflects photons with odd OAM values and transmits even ones. In this manner, an outgoing photon contains a superposition of odd and even values of OAM from two independent input photons.

Our procedure for generating the high-dimensional tripartite state uses two independent entangled photon pairs created in two non-linear crystals (NL1 and NL2). Suppose that the two pairs are in the state

$$\begin{aligned} |\Psi\rangle_{ABCD} = &\frac{1}{\sqrt{3}}(\,|1\rangle_A\,|\text{-}1\rangle_B + |0\rangle_A\,|0\rangle_B + |\text{-}1\rangle_A\,|1\rangle_B\,) \\ &\otimes\frac{1}{\sqrt{3}}(\,|1\rangle_C\,|\text{-}1\rangle_D + |0\rangle_C\,|0\rangle_D + |\text{-}1\rangle_C\,|1\rangle_D\,), \end{aligned} \tag{6.3}$$

which is a tensor product of two OAM-entangled photons pairs (A, B and C, D) of dimension $d = 3$ each (OAM quantum number $\ell \in \{-1, 0, 1\}$). At this stage, mixing these two states results in nine possible four-photon amplitudes. Photons B and C are then incident on the two inputs of the OAM beam splitter. Since this device reflects odd values of OAM and transmits even ones, a coincidence detection between the two outputs can only arise when photons B and C are both carrying either odd or even values of OAM. This projects the state from Eq. (6.3) onto a subspace spanned by the five terms $(|1\rangle_A\,|\text{-}1\rangle_B\,|1\rangle_C\,|\text{-}1\rangle_D)$, $(|1\rangle_A\,|\text{-}1\rangle_B\,|\text{-}1\rangle_C\,|1\rangle_D)$, $(|0\rangle_A\,|0\rangle_B\,|0\rangle_C\,|0\rangle_D)$, $(|\text{-}1\rangle_A\,|1\rangle_B\,|1\rangle_C\,|\text{-}1\rangle_D)$, and $(|\text{-}1\rangle_A\,|1\rangle_B\,|\text{-}1\rangle_C\,|1\rangle_D)$. Photon D is then measured in a superposition state given by $|P\rangle_D^{0,\text{-}1} = \frac{1}{\sqrt{2}}(|0\rangle_D + |\text{-}1\rangle_D)$ via a mode-projection carried out by a spatial light modulator (SLM) and a single-photon detector (T). This acts as a trigger for the three-photon entangled state:

$$|\Psi\rangle_{\text{exp}} = \frac{1}{\sqrt{3}}[\,|1\rangle_A\,|\text{-}1\rangle_B\,|1\rangle_C + |0\rangle_A\,|0\rangle_B\,|0\rangle_C + |\text{-}1\rangle_A\,|1\rangle_B\,|1\rangle_C\,]. \tag{6.4}$$

Note that this state has the same form as equation 6.1, except photons A and B are in a three-dimensional space given by the OAM quantum numbers (-1, 0, 1), while photon C is in a two-dimensional space given by (0, 1).

6.2 HOM Interference and Experimental Constraints

In order to ensure that these three terms are in a coherent superposition (as opposed to an incoherent mixture), we perform superposition measurements in a two-dimensional subspace spanned by the second and third terms in equation 6.4. Measuring photon A in a superposition state given by $|M\rangle_A^{0,\text{-}1} = \frac{1}{\sqrt{2}}(|0\rangle_A - |\text{-}1\rangle_A)$ projects the three-photon state into:

$$\frac{1}{\sqrt{3}}\,|\mathrm{M}\rangle_A^{0,\text{-}1}\,(|\mathrm{P}\rangle_B^{0,1}\,|\mathrm{M}\rangle_C^{0,1} + |\mathrm{M}\rangle_B^{0,1}\,|\mathrm{P}\rangle_C^{0,1}), \tag{6.5}$$

where $|P\rangle_{B/C}^{0,1} = \frac{1}{\sqrt{2}}(|0\rangle_{B/C} + |1\rangle_{B/C})$ and $|M\rangle_{B/C}^{0,1} = \frac{1}{\sqrt{2}}(|0\rangle_{B/C} - |1\rangle_{B/C})$. The terms $|\mathrm{P}\rangle_B^{0,1}\,|\mathrm{P}\rangle_C^{0,1}$ and $|\mathrm{M}\rangle_B^{0,1}\,|\mathrm{M}\rangle_C^{0,1}$ are missing because of two-photon destructive interference at the OAM beam splitter, which only occurs when photons B and C are indistinguishable[10]. Note that this requires both two-photon and one-photon interference (for two different photons) to occur at the OAM beam splitter, which proved to be an experimental challenge.

The use of narrowband interference filters (IF2) before detectors B and C blurs out the temporal correlations of the photons with their entangled partners to a certain extent, ensuring that they

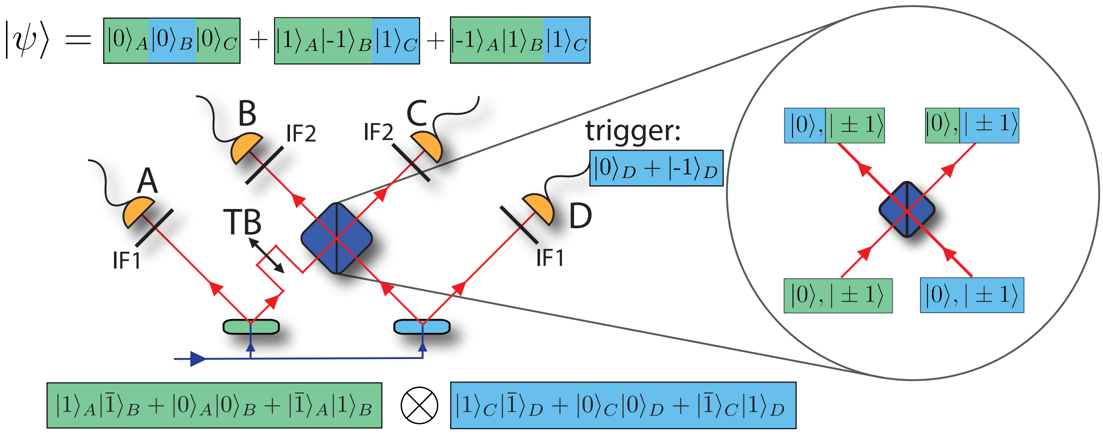

Figure 6.1: A blue laser pulse creates two pairs of OAM-entangled photons in two nonlinear crystals (NL1 and NL2). A moving trombone prism ensures that a photon from each pair arrives simultaneously at the OAM beam splitter. The OAM beam splitter reflects odd components of OAM and transmits even ones, mixing the OAM components of two input photons. A coincidence at detectors B and C can only arise when both detected photons have the same mode parity. This projects photons at detectors A, B, and C into an asymmetric three-photon entangled state that is entangled in $3 \times 3 \times 2$ dimensions of its OAM. The detection of a trigger photon at detector D heralds the presence of this state.

cannot be distinguished based on their time of arrival[48]. We look for destructive interference between photons B and C by projecting them into states $|\mathrm{M}\rangle_B^{0,1}$ and $|\mathrm{M}\rangle_C^{0,1}$, and scanning the trombone prism shown in Fig. 6.1. At the zero-delay position, both photons arrive at the first beam splitter (BS1) at precisely the same time and interfere destructively, leading to a drop in coincidence counts between detectors B and C, conditioned on photons A and D being detected in states $|\mathrm{M}\rangle_A^{0,\text{-}1}$ and $|\mathrm{P}\rangle_D^{0,\text{-}1}$ respectively.

As mentioned above, the interference of two photons at the OAM beam splitter critically depends on the indistinguishability of the two particles involved. Since the presence of the interfering photons is indicated by the trigger detection events of their respective partner photons, we effectively observe four-photon coincidence events. The interference visibility strongly depends on the physical properties of these four photons, as well as the process by which they are created. This particular phenomenon has been studied in great detail[48] and the theoretically expected visibility is calculated to have the form

$$V' = \left[2 \frac{\sqrt{\sigma_T^2 + \sigma_P^2}\sqrt{\sigma_S^2 + \sigma_P^2 + \sigma_S^2 \sigma_P^2 \tau_J^2}}{\sigma_P \sqrt{\sigma_S^2 + \sigma_T^2 + \sigma_P^2}} - 1 \right]^{-1}. \tag{6.6}$$

Here, σ_P, σ_S, and σ_T are the gaussian spectral widths of the pump, signal, and trigger photons respectively (in units of frequency). σ_S and σ_T are determined by the widths of narrowband interference filters IF2 and IF1, respectively. τ_J has units of time and refers to the relative timing jitter between the two crystals, which arises due to the group velocity mismatch between the 404nm pump pulse and the 808nm down-converted photons in the ppKTP crystals. Additionally, due to the finite pulse width of the 404nm pump beam, a second relative timing jitter between the two crystals is also present. In our experiment, the sum of these two timing jitters is approximately 1ps [49].

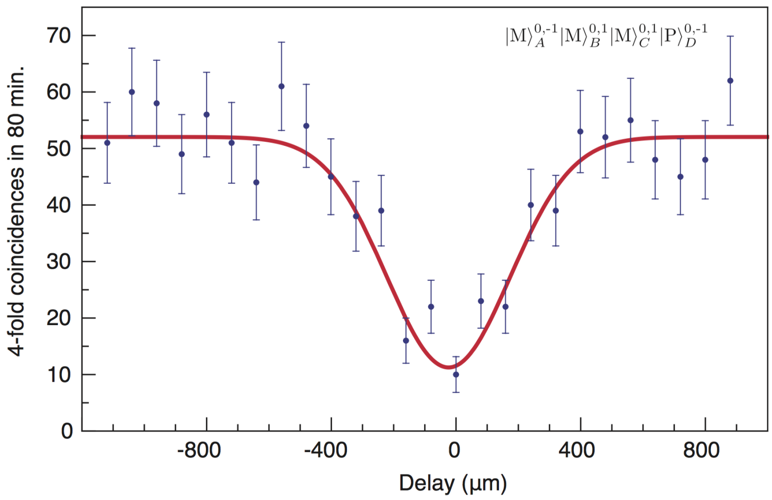

Figure 6.2: **Three-photon coherent superposition.** Experimental data showing the result of measuring photons A, B, and C in states $|\mathrm{M}\rangle_A^{0,-1}$, $|\mathrm{M}\rangle_B^{0,1}$, and $|\mathrm{M}\rangle_C^{0,1}$ respectively, conditioned on measuring photon D in state $|\mathrm{P}\rangle_D^{0,-1}$. The drop in coincidence counts at the position of zero delay results from interference between photons B and C. This indicates that the 3-photon state from equation 6.4 is in a coherent superposition. A Gaussian fit is calculated based on the spectral shape of our narrowband filters and has a full-width at half-maximum of 473μm and a visibility of 63.5%.

In addition to spectral distinguishability, the spatial and temporal distinguishability of the two photons both play an important role in the interference visibility. The moving trombone system of mirrors (TB) is used to find the position of zero-delay when photons from both crystals arrive at the OAM beam splitter at the same exact time. The spatial-mode distinguishability of the two input photons at the OAM beam splitter has a further detrimental effect on the total interferometric visibility. We use a $4f$ imaging system of lenses (L6) in order to compensate for the extra propagation that the photon from NL1 undergoes with respect to the photon from NL2. Nonetheless, the mode overlap of the two photons at the OAM splitter is not perfect, and reduces the two-photon interference visibility in the following way:

$$V = \frac{\eta^2 V'}{1 + V'(1-\eta^2)}. \tag{6.7}$$

Here, $\eta = \eta_{\mathrm{OAM}} \times \eta_{\mathrm{SP}}$ is the product of the sorting efficiency η_{OAM} of the OAM beam splitter and the spatial mode overlap η_{SP} of the two input photons. Inserting our measured/estimated experimental parameters (σ_P = 3.67THz, σ_T = 588GHz, σ_S = 184GHz, τ_J = 1ps, $\eta_{\mathrm{OAM}} = 0.99$ and $\eta_{\mathrm{SP}} = 0.9$) into the above formula yields a two-photon interference visibility of $V = 0.64$, which is very close to the experimental visibility observed in Fig. 6.2. The visibility critically depends on the spectral width σ_S of the two interfering photons. A smaller σ_S greatly improves the interference visibility at the cost of lowering the four-photon count rates. It is therefore important to find an optimal value that provides both sufficiently high visibility and practical count rates. In our experiment, we found this value to be σ_S = 184GHz. Assuming a Gaussian spectral distribution, the theoretical

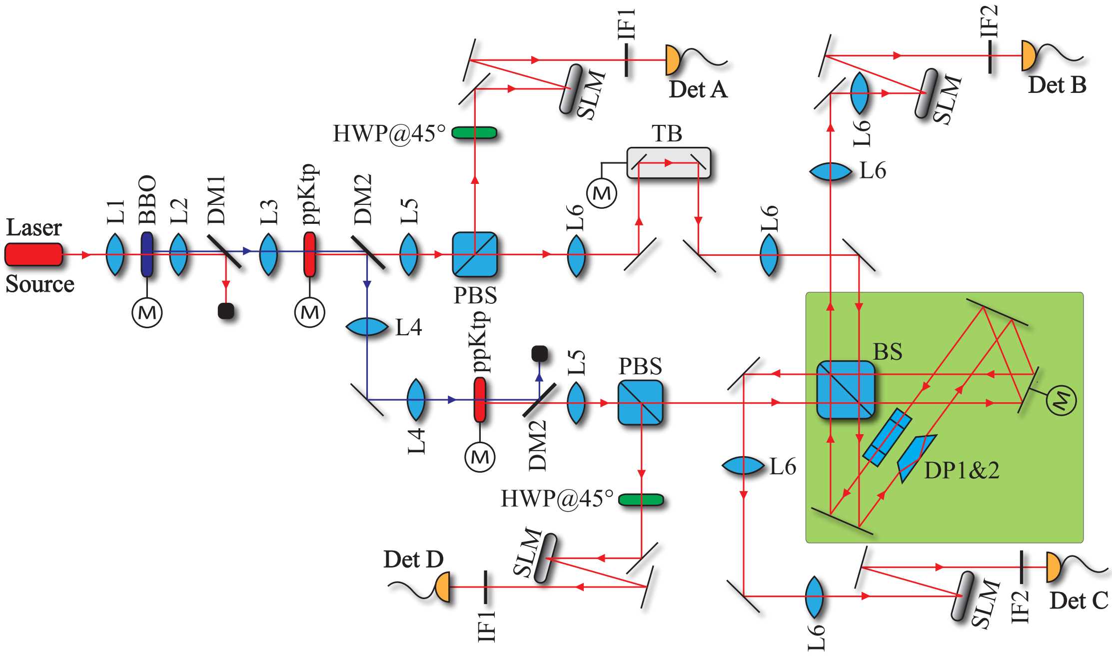

Figure 6.3: **Detailed Experimental Setup.** For a detailed description see main text. L...Lens; BBO...β-Barium Borate crystal; DM...dichroic mirror; ppKtp...periodically poled potassium titanyl phosphate crystal; PBS...polarizing beam splitter; HWP...half-wave-plate; TB...trombone system; SLM...spatial light modulator; IF...interference filter; Det...detector;

full-width at half-maximum (FWHM) of the two-photon interference dip is then given by

$$L_{\text{dip}} = \frac{c}{\pi}\sqrt{\frac{2\ln 2}{\sigma_P^{-2} + \sigma_S^{-2} + \tau_J^2}}. \tag{6.8}$$

Inserting the corresponding values from above leads to a expected FWHM dip-width of 624μm, which is close to our experimentally observed value of 473μm in Fig. 6.2. It is clear from equations (6) and (7) that the spatial mode overlap η_{SP} has a drastic effect on the interference visibility, and hence on the fidelity of our state. Since the experiment was run over a long time, we suspect that the air flow in the laboratory had a direct impact on the time-averaged spatial mode overlap at the OAM-BS. We believe that this can be improved by more effectively isolating the beam paths from the laboratory environment.

The characteristic dip in Fig. 6.2 has a width of 473μm that matches what we expect from the bandwidth of our filters and the thickness of our crystals.

6.3 Detailed Experimental (3,3,2) Setup

As shown in extended data Fig. 1, a 140 femtosecond pulsed Ti:Sapphire laser with a repetition rate of 80 MHz (Coherent Chameleon Ultra II) and a center wavelength of 808nm is focused by lens L1 into a β-Barium Borate crystal (BBO) to generate blue pump pulses at 404nm via the process of second-harmonic generation. The BBO crystal is incrementally moved by a motor (M) in order to avoid damage to it. The generated pump pulses (average power of 820mW) are re-collimated by lens L2 and separated from the 808nm light by a dichroic mirror (DM1). They are then focused with lens L3 onto two periodically poled potassium titanyl phosphate (ppKTP) crystals (NL1 and NL2) with dimension 1mm × 2mm × 1mm and poling period 9.55μm for type-II phase matching. Two independent photon pairs entangled in their orbital angular momentum (OAM) are generated in the two crystals via spontaneous parametric down-conversion (SPDC) of the same pump pulse. The crystals are spatially oriented so that down-conversion occurs when the pump pulses are vertically polarized. In order to conform to the phase-matching conditions for producing wavelength-degenerate photon pairs at 808nm, NL1 (NL2) is heated to 119.1°C (121.9°C). A $4f$ imaging system composed of two lenses (L4) between between the two crystals ensures that the waist of the pump pulse is approximately 240μm at both crystals. The pump waist is chosen such that generation rate of $l = 0$ photons is approximately twice that of the $l = \pm 1$ photons in the two OAM-entangled photon pairs. Note that the OAM state distributions in equation (6.3) are flat, while our experimentally generated distributions are not. We account for this by unbalancing the trigger photon (D) state superposition to $|P\rangle_D^{0,-1} = 0.51\,|0\rangle_D + 0.86\,|\text{-}1\rangle_D$, which surprisingly lowers our average four-fold count rates only by 6%. Two dichroic mirrors (DM2) separate the 404nm pump pulses from the entangled photon pairs. Due to the high pump power, the Kerr-lensing effect cannot be neglected and adds an equivalent lens with 1m focal length into the optical path. This is compensated by carefully aligning the $4f$ imaging system (L4). To avoid gray-tracking due to the high pump power, the ppKTP crystals are also moved incrementally in steps of 200μm with motors (M). Movement of the BBO and ppKTP crystals shows slight variation in the count rates, which is compensated for by averaging over several periods of movement within each measurement interval. Two polarizing beam splitters (PBS) deterministically separate both photon pairs such that all four photons are propagating in different directions.

The single photon projective measurements are performed in the following way. Two additional $4f$ imaging systems (L6) image the output of the OAM beam splitter onto two holographic spatial light modulators (SLMs). These are liquid-crystal devices that can impart an arbitrary 2D phase pattern onto a photon. We use these devices to perform projection measurements of OAM. These measurements are carried out by flattening the phase of incident photons such that they couple into a single-mode optical fiber[38]. The scheme is based on the fact that a single-mode fiber (SMF) only carries spatial modes with $\ell = 0$. In order to detect a photon with $\ell = 1$, a hologram with $\ell = -1$ displayed on the SLM projects the photon into mode $\ell = 0$. The photon then couples efficiently to an SMF and is guided to an single photon avalanche photodiode (Excelitas SPCM-AQRH-14-FC). The same procedure also applies to projective measurements of mode superpositions. Note that in our experiment, phase-only holograms are used, which take only the vortex phase structure $e^{i\ell\varphi}$ of a Laguerre-Gaussian mode into account, and not its amplitude. This results in an imperfect mode overlap at the SMF [50] and leads to lowered coupling efficiencies for modes with $\ell = \pm 1$. This drop in efficiency can be somewhat compensated by adding a mode-dependent quadratic phase to these holograms, which changes the effective coupling mode-waist.

6.4 Entanglement Verification

Fully reconstructing our quantum state via quantum tomography would be impractical, even with the use of modern techniques as such compressive sensing[51]. Instead, we have developed a new method for certifying high-dimensional multipartite entanglement using a minimum number of measurements.

This method relies on proving that the measured (332)-state cannot be decomposed into entangled states of a smaller dimensionality structure [9, 43], such as a (322)-state or a two-dimensional GHZ/(222)-state. As shown in Fig. 6.4(a), these states take on a "Russian nesting doll" structure of concentric subsets embedded in the set of (332)-states, and can be ruled out as follows. First,

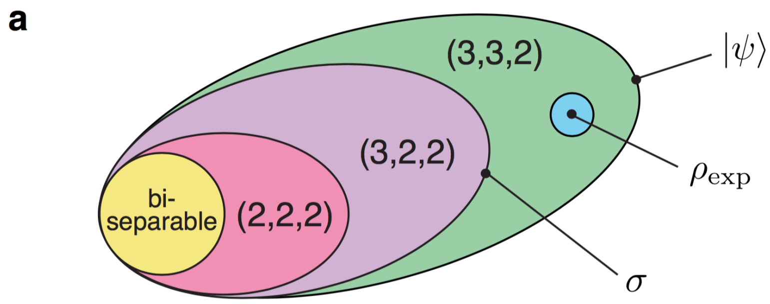

Figure 6.4: In order to verify that our three-photon state is entangled in $3 \times 3 \times 2$ dimensions, we have to show that it cannot be decomposed into entangled states of a smaller dimensionality structure. First, we calculate the best achievable overlap of a (322)-state σ with an ideal target (332)-state $|\Psi\rangle$ to be $F_{\max} = 2/3$. Next, we calculate the overlap $F_{\exp}$ of our experimentally generated state $\rho_{\exp}$ with the target state $|\Psi\rangle$.

we find the best achievable overlap $F_{\max}$ of a (322)-state σ with an ideal (332)-state $|\Psi\rangle$. Next, we calculate the overlap $F_{\exp}$ of our experimentally generated state $\rho_{\exp}$ with an ideal (332)-state. If $F_{\exp} > F_{\max}$, our state is certified to be entangled in $3 \times 3 \times 2$ dimensions.

In order to prove that the state is indeed a (332)-type entangled state we have to prove that it cannot be decomposed into states of a smaller dimensionality structure. We thus have to show that it lies outside the (322)-set of states, that is the convex hull of all states that can be decomposed into 322 and 232 states. From the measured data we can extract the fidelity to the ideal state

$$|\Psi\rangle = \frac{1}{\sqrt{3}} \left(|0,0,0\rangle + |1,-1,1\rangle + |-1,1,1\rangle\right) , \tag{6.9}$$

which we will denote as $F_{\exp} := \mathrm{Tr}(\rho_{\exp}|\Psi\rangle\langle\Psi|)$. We thus need to compare the experimental fidelity with the best achievable fidelity of a (322)-state, i.e.

$$F_{\max} := \max_{\sigma\in(322)} \mathrm{Tr}(\sigma|\Psi\rangle\langle\Psi|) . \tag{6.10}$$

If $F_{\exp} > F_{\max}$, we can conclude that the experimentally certified fidelity cannot be explained by any state in (322) and thus the underlying state is certified to have an entangled dimensionality structure of (332). To calculate $F_{\max}$ it is useful to observe that it is convex in the set of states, i.e. the maximum will always also be reachable by a pure state. Furthermore, since the set (322) is the convex hull of 322 and 232, we can write the following

$$F_{\max} = \max_{|\Phi\rangle\in(322)} |\langle\Psi|\Phi\rangle|^2 = \max[\max_{|\Phi\rangle\in 322} |\langle\Psi|\Phi\rangle|^2, \max_{|\Phi\rangle\in 232} |\langle\Psi|\Phi\rangle|^2] . \tag{6.11}$$

Now for a fixed rank vector xyz, these fidelities can be bounded by noticing that

$$\max_{|\Phi\rangle\in xyz} |\langle\Psi|\Phi\rangle|^2 \leq \min[\max_{rank(\mathrm{Tr}_{23}|\Phi\rangle\langle\Phi|)=x} |\langle\Psi|\Phi\rangle|^2, \max_{rank(\mathrm{Tr}_{13}|\Phi\rangle\langle\Phi|)=y} |\langle\Psi|\Phi\rangle|^2, \max_{rank(\mathrm{Tr}_{12}|\Phi\rangle\langle\Phi|)=z} |\langle\Psi|\Phi\rangle|^2] . \tag{6.12}$$

Now inserting (6.12) in (6.11) we can compute each of the appearing terms using a previously published theorem [43]. It states that if a state has a Schmidt decomposition across a cut $A|\overline{A}$ given by $|\Psi\rangle = \sum_{i_0}^{r-1} \lambda_i |v_A^i\rangle \otimes |v_{\bar{A}}^i\rangle$, we can compute the maximal overlap with a state of bounded rank across this partition as

$$\max_{rank(\mathrm{Tr}_{\bar{A}}|\Phi\rangle\langle\Phi|)=x} |\langle\Psi|\Phi\rangle|^2 = \sum_{i=0}^{x-1} \lambda_i^2 \,, \tag{6.13}$$

where we assumed ordered Schmidt coefficients, i.e. $\lambda_i \geq \lambda_{i+1}$. Now all we need are the coefficients for the Schmidt decompositions for our target state for all three partitions. For 3|12 they are $\{\frac{\sqrt{2}}{\sqrt{3}}, \frac{1}{\sqrt{3}}\}$ and for 2|13 and 1|23 we get $\{\frac{1}{\sqrt{3}}, \frac{1}{\sqrt{3}}, \frac{1}{\sqrt{3}}\}$. Inserting these numbers we find that the maximum overlap of the target state (6.9) with a (322) state is given by

$$F_{\max} = \frac{2}{3} \,. \tag{6.14}$$

6.5 Measurement Results

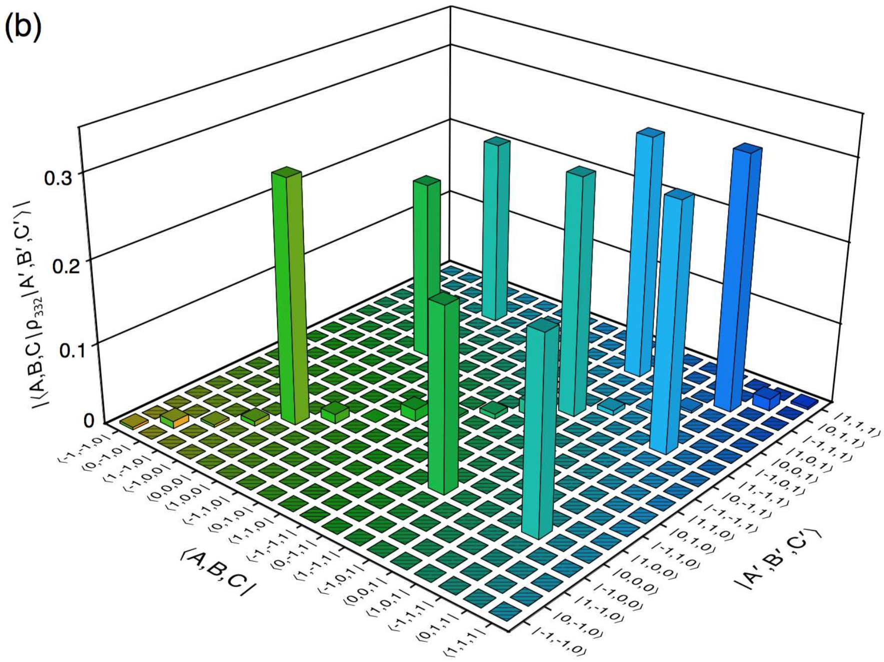

Figure 6.5: The 18 diagonal and 3 unique off-diagonal elements of ρ_{exp} that are measured in order to calculate a value of $F_{\text{exp}} = 0.801 \pm 0.018$ (elements not measured are filled in with crossed lines). This is above the bound of $F_{\max} = 0.667$ by 7 standard deviations and verifies that the generated state is genuinely multipartite entanglement in $3 \times 3 \times 2$ dimensions of its orbital angular momentum. F_{exp} does not reach its maximal value of 1 because the state superstition is not perfectly coherent. Theoretical values are shown by empty bars.

The experimental fidelity $F_{\text{exp}} := \mathrm{Tr}(\rho_{\text{exp}}|\Psi\rangle\langle\Psi|)$ determines which measurements are required. The projector $|\Psi\rangle\langle\Psi|$ projects only onto the theoretically expected non-zero diagonal and off-diagonal elements contained in the density matrix ρ_{exp}. Additionally, for the purpose of normalization, it is necessary to measure all other diagonal elements in ρ_{exp}. This results in 18 diagonal and 3 unique off-diagonal elements that need to be measured in order to calculate F_{exp}. In our experiment, we can only perform projective measurements with SLMs. A diagonal element is given by one single projection $\langle ijk|\rho|ijk\rangle = \frac{C(ijk)}{C_T}$, with $C_T := \sum_{i=-1,0,1}\sum_{j=-1,0,1}\sum_{k=0,1} C(ijk)$ containing all diagonal elements for normalization. Out of the six off-diagonal elements, only three are unique and need to be measured: $\langle 000|\rho|1\text{-}11\rangle$, $\langle 000|\rho|\text{-}111\rangle$ and $\langle \text{-}111|\rho|1\text{-}11\rangle$. Note that the last off-diagonal element is only in a two-particle superposition. Hence, it can be measured in the standard way that two-particle two-dimensional states are usually measured. In order to measure the other two off-diagonal elements with projective measurements, we decompose them into σ_{x} and σ_{y} measurements. The real and imaginary part of each element can be written in analogy to section A.9 as

$$\begin{gathered}
\Re[\langle ijk|\rho|lmn\rangle] = \\
= \left\langle \sigma_{\mathrm{x}}^{\mathrm{i,l}} \otimes \sigma_{\mathrm{x}}^{\mathrm{j,m}} \otimes \sigma_{\mathrm{x}}^{\mathrm{k,n}} \right\rangle - \left\langle \sigma_{\mathrm{y}}^{\mathrm{i,l}} \otimes \sigma_{\mathrm{y}}^{\mathrm{j,m}} \otimes \sigma_{\mathrm{x}}^{\mathrm{k,n}} \right\rangle - \left\langle \sigma_{\mathrm{y}}^{\mathrm{i,l}} \otimes \sigma_{\mathrm{x}}^{\mathrm{j,m}} \otimes \sigma_{\mathrm{y}}^{\mathrm{k,n}} \right\rangle - \left\langle \sigma_{\mathrm{x}}^{\mathrm{i,l}} \otimes \sigma_{\mathrm{y}}^{\mathrm{j,m}} \otimes \sigma_{\mathrm{y}}^{\mathrm{k,n}} \right\rangle \\
\Im[\langle ijk|\rho|lmn\rangle] = \\
= \left\langle \sigma_{\mathrm{y}}^{\mathrm{i,l}} \otimes \sigma_{\mathrm{y}}^{\mathrm{j,m}} \otimes \sigma_{\mathrm{y}}^{\mathrm{k,n}} \right\rangle - \left\langle \sigma_{\mathrm{x}}^{\mathrm{i,l}} \otimes \sigma_{\mathrm{x}}^{\mathrm{j,m}} \otimes \sigma_{\mathrm{y}}^{\mathrm{k,n}} \right\rangle - \left\langle \sigma_{\mathrm{x}}^{\mathrm{i,l}} \otimes \sigma_{\mathrm{y}}^{\mathrm{j,m}} \otimes \sigma_{\mathrm{x}}^{\mathrm{k,n}} \right\rangle - \left\langle \sigma_{\mathrm{y}}^{\mathrm{i,l}} \otimes \sigma_{\mathrm{x}}^{\mathrm{j,m}} \otimes \sigma_{\mathrm{x}}^{\mathrm{k,n}} \right\rangle,
\end{gathered} \tag{6.15}$$

where $\sigma_{\mathrm{x}}^{\mathrm{a,b}} = |a\rangle\langle b| + |b\rangle\langle a|$ and $\sigma_{\mathrm{y}}^{\mathrm{a,b}} = i\,|a\rangle\langle b| - i\,|b\rangle\langle a|$. The $\sigma_{x,y}$ operators here can be measured in an identical procedure as given in section A.10. In summary, this leads to 64 projection measurements required for measuring each of the two off-diagonal elements $\langle 000|\rho|1\text{-}11\rangle$ and $\langle 000|\rho|\text{-}111\rangle$. Only 16 projection measurements are required for the off-diagonal element $\langle \text{-}111|\rho|1\text{-}11\rangle$ since it involves only one dimension for photon C. Summing up these measurements as well as the 18 diagonal elements leads to 162 measurements in total. The results of these are given in extended data table 1. From these measurements, the overlap between the generated state ρ_{exp} and the ideal state (332)-state $|\Psi\rangle$ is calculated to be

$$F_{\mathrm{exp}} = 0.801 \pm 0.018. \tag{6.16}$$

This is the main result of this thesis. It proves the first multi-photon high-dimensionally entangled state. With a violation of the fidelity witness by 7 standard deviations it clearly demonstrates the experimental creation of a quantum state with a SRV of $(3, 3, 2)$. The error in the overlap is calculated by propagating the Poissonian error in the photon-counting rates by performing a Monte Carlo simulation of the experiment.

Chapter 7

Conclusion

The seemingly simple quote from Schrödinger:

"Best possible knowledge of a whole does not include best possible knowledge of its parts – and that is what keeps coming back to haunt us."

states the very essence about entanglement, but still doesn't quite give an impression of what wonderful and strange types of entanglement there can exist in complex quantum systems. To introduce the reader of this thesis to this fascinating topic we started in Chapter 1 with the simplest possible system of two particles in two dimensions. Then, a new theoretical classification tool for entanglement of more general quantum systems in terms of the Schmidt-Rank-Vector (SRV) for multiple particles in high-dimensions was introduced. The SRV for an n-partite system is a vector with $2^{n-1} - 1$ entries, where each entry describes the Schmidt-Rank of the reduced density matrix with respect to the possible bipartite decompositions. A given quantum state is called genuinely multi-partite and high-dimensionally entangled iff all entries of the SRV are strictly bigger than one and at least one of them is strictly bigger than two. Furthermore, different aspects about entanglement, e.g. the amount of entanglement in a given system or the usefulness of this entanglement for certain tasks, were discussed. As the title of this thesis *Experimental Multi-Partite High-Dimensional Entanglement* suggests, the main body of the work at hand is about the experimental realization of such multi-partite high-dimensionally entangled states.

The experimental goal of this thesis was to create such a multi-partite high-dimensionally entangled state for the very first time. Strictly speaking, the aim was to create a three-partite entangled state in high dimensions. In our case this is a state with a SRV = $(3, 3, 2)$, meaning two bipartitions have dimensionality three and one bipartition has dimensionality two. As a physical carrier of information, photons have proven to be very useful. The reason is that photons don't interact with their environment easily, but still can be manipulated very precisely and in a highly controlled fashion. A natural high-dimensional degree of freedom is given by the orbital-angular-momentum (OAM) of photons. Therefore, the OAM of photons is used in this work to experimentally create a (3,3,2) entangled state. The tools needed to create such a state experimentally have been developed during the course of this work.

One of the key elements to create multi-partite entanglement is the so-called Hong-Ou-Mandel (HOM) effect. To the best of my knowledge, this effect has been shown with the OAM of photons for the first time in this work. The resulting very high visibilities of approximately 90 percent for $\ell = 1, 2, 3, 4, 5$ show the ability to handle this specific degree of freedom very well technically. Not only has the HOM effect itself been shown experimentally, a new protocol to generate so-called $\ell 00 \ell$-states has been found in addition. In principle, this protocol can produce arbitrarily high ℓ-values of $\ell 00\ell$-states. The 2002-state created in this work showed a HOM-dip visibility of 82 percent and a HOM-bump visibility of 66 percent. These two visibilities are a measure of the purity of the created 2002-state.

The second tool developed in this work is the high-dimensional entanglement router (HDR). Based on an interferometric principle, this device is capable of splitting up even ($\ell = 0, 2, 4, ...$) and odd ($\ell = 1, 3, 5, ...$) OAM modes. It was found that that the HD router is not only capable of splitting up even and odd modes, but also to split up a high-dimensionally entangled state into two smaller but still high-dimensionally entangled states: $|\psi\rangle_{AB}^{\text{even/odd}} \xrightarrow{HDR} |\alpha\rangle_{AB}^{\text{even}} + |\pi\rangle_{AC}^{\text{odd}}$. In our experiment we have been able to show the routing of an at least 10-dimensionally entangled input state $|\psi\rangle$ into a 5-dimensionally entangled state $|\alpha\rangle$ and a 6-dimensionally entangled state $|\pi\rangle$. The experimental challenge to stabilize the interferometer was addressed by using an intrinsically stable interferometer design (folded double-path Sagnac-Type-Interferometer) with an active piezo control. With this configuration we have been able to show a long term stability of more than 35 hours continuous data sampling without manual adjustments. The long-term stability of this device is a necessary condition for multi-photon experiments, since the measurement time for such experiments can reach several days.

Finally, to create a multi-partite high-dimensionally entangled state experimentally, all these tools have been generalized and merged in one setup. Two high-dimensionally entangled states produced in two non-linear crystals are overlapped at the HDR to exploit a HOM effect in certain OAM modes. Thus the HDR in combination with the HOM effect in the OAM degree of freedom is used to create a multi-partite high-dimensionally entangled state from two bipartite high-dimensionally entangled states. One of the four photons created is used as a *trigger*-photon, which means that if this photon is detected in a certain state given a four-fold detection event, the other three photons are in the desired (3,3,2) state. The four-photon HOM effect in the OAM degree of freedom at the HDR exploited in this setup showed an experimental visibility of 63.5 percent. The reduced visibility observed here is analyzed in detail. The theoretical estimations of the spectral properties and the spatial overlap of the freely propagating photons result in an expected visibility close to the experimentally observed one. Furthermore, we have experimentally verified the creation of a (3,3,2) state with a fidelity of $F_{exp} = 0.801 \pm 0.018$. This violates the fidelity witness bound of $F = 2/3$ for a SRV=(3,3,2) state by more than 7 standard deviations, thus demonstrating the first experimental creation of a multi-photon high-dimensionally entangled quantum state [41].

In conclusion, this thesis showed the possibility of creating multi-photon, high-dimensionally entangled states experimentally with the OAM of photons. Additionally, it also demonstrated the ability of the OAM of photons to serve as a testing bed for more complex entanglement structures in future. The creation of a three-dimensional Greenberger-Horne-Zeilinger state is one possible application stemming from the methods developed in this thesis, allowing us to further investigate fundamental questions in quantum physics. Furthermore, technological applications like quantum cryptography in hierarchical-layered communication schemes [41] constitute other interesting directions of research that could be investigated with the tools developed in this work.

Acknowledgments

First and foremost, I would like to thank Prof. Anton Zeilinger for giving me the chance to work together with him and his fantastic group. It was, and still is a great pleasure to work in this inspiring place with so many talented and gifted people.

Especially, I would like to thank Mehul Malik, Mario Krenn, Robert Fickler, Nora Tischler and Radek Lapkiewicz for welcoming me in the *"high-dim subgroup"*. Without the countless hours spent together with Mehul in the lab, this thesis would have never been possible. Not only have I learned a lot of tricks in the lab from Mehul, he also proofread my thesis, which I'm sure took him a very long time! Thank you a thousand times for that Mehul! Also a special thanks to Mario for sharing his knowledge and enthusiasm for physics, artificial intelligence and all kinds of science with me!

A special thanks goes to my girlfriend Katharina, my parents Gertrud and Kurt, my brother Alexander, all my family (aunts, uncles and grandparents) my roommate and best friend Moritz, my best friend Bernhard and all my other friends all over the world for their love, moral and financial support, friendship and just time we spent together. THANK YOU!!!

Finally, I would like to thank the Austrian state and the people living in Austria. Without the financial support from the federal aid system for students by the Austrian state, it would not have been possible for me to study physics.

This project was supported by the Austrian Academy of Sciences (ÖAW), the European Research Council (SIQS Grant No. 600645 EU-FP7-ICT), the Austrian Science Fund (FWF) with SFB F40 (FOQUS).

Appendix A

Appendix

A.1 Schmidt-Decomposition

Consider a state $|\psi\rangle$ with a bi-orthogonal decomposition $|\psi\rangle = \sum_i \alpha_i |a_i\rangle |b_i\rangle$, where $\alpha_i \in \mathbb{C}$ and $\left\langle a_i \middle| b_j \right\rangle = \delta_{i,j}$. The density matrix of $|\psi\rangle$ thus reads

$$\rho = |\psi\rangle \langle\psi| = \sum_{i,j} \alpha_i \alpha_j^* |a_i\rangle |b_i\rangle \left\langle a_j \right| \left\langle b_j \right| = \sum_{i,j} \alpha_i \alpha_j^* |a_i\rangle \left\langle a_j \right| \otimes |b_i\rangle \left\langle b_j \right|. \tag{A.1}$$

The partial trace over subsystem A yields

$$\mathrm{Tr}_A(\rho) = \sum_{i,j} \alpha_i \alpha_j^* \mathrm{Tr}_A \left(|a_i\rangle \left\langle a_j \right| \right) \otimes |b_i\rangle \left\langle b_j \right|, \tag{A.2}$$

with $\mathrm{Tr}_A \left(|a_i\rangle \left\langle a_j \right| \right) = \delta_{ij}$. Hence,

$$\mathrm{Tr}_A(\rho) = \sum_i \alpha_i \alpha_i^* |b_i\rangle \langle b_i| = \sum_i |\alpha_i|^2 |b_i\rangle \langle b_i|, \tag{A.3}$$

with $\sum_i |b_i\rangle \langle b_i|$ denoting a diagonal matrix. The entries of a diagonal matrix correspond to the eigenvalues of this matrix. This result shows that for a bi-orthogonal state decomposition the partial trace over one subsystem leads to the sum of eigenvalues. Additionally, this also proofs that the rank of the reduced density matrix corresponds to the Schmidt rank of the pure state $|\psi\rangle$.
□

A.2 Entropy of Entanglement Proof

Schmidt decomposition of a pure bipartite qudit state:

$$|\psi_{AB}\rangle = \sum_i \lambda_i |a_i\rangle |b_i\rangle \tag{A.4}$$

where $|a_i\rangle, |b_i\rangle$ form a basis of $\mathcal{H}_A$ and $\mathcal{H}_B$ respectively.

$$\begin{aligned} \rho_A \quad = \mathrm{Tr}_B(\rho_{AB}) \quad &= \sum_{i,j} \lambda_i \lambda_j^* |a_i\rangle \langle a_j| \mathrm{Tr}\left(|b_i\rangle \langle b_j| \right) \\ &= \sum_i \lambda_i \lambda_i^* |a_i\rangle \langle a_i| \end{aligned} \tag{A.5}$$

If ρ_{AB} is separable, there is only one non-vanishing λ and therefore $S(\rho_A) = 0$. The same calculation can be done for ρ_B. □

A.3 Solving the Paraxial Equation in Cartesian Coordinates

The following sections are about solving the paraxial equation and follow the treatment in Ref. [52]. The paraxial approximation of the Helmholtz equation has the same structure as the Schrödinger equation. Hence it is worth reminding ourselves that spherical waves are the solutions of the Schrödinger equation. We take this as the motivation for our Ansatz.

$$\begin{aligned}\frac{e^{ikr}}{r} = \frac{e^{ik\sqrt{x^2+y^2+z^2}}}{\sqrt{x^2+y^2+z^2}} &= \frac{e^{ikz\sqrt{1+(x^2+y^2)/z^2}}}{z\sqrt{1+(x^2+y^2)/z^2}} \\ &\approx \frac{e^{-ikz}e^{-ik(x^2+y^2)/2z}}{z},\end{aligned} \tag{A.6}$$

where we substitute $\rho^2 = x^2 + y^2$. The "quadratic" form of this approximate solution suggests looking for an axially symmetric solution of the form:

$$E_G(\rho, z) = A_G \exp[-iP(z)]\exp[\frac{-ik\rho^2}{2q(z)}]. \tag{A.7}$$

Simply substituting this in Eq. 2.15 yields:

$$\frac{k\exp\left(-\frac{1}{2}i\left(\frac{k(x^2+y^2)}{q(z)} + 2P(z)\right)\right)}{q(z)^2}\left(k\left(x^2+y^2\right)(q'(z)-1) - 2q(z)\left(q(z)P'(z)+i\right)\right) = 0. \tag{A.8}$$

In order to satisfy the equation above, the following two equations must hold:

$$q'(z) - 1 = 0 \tag{A.9}$$

$$q(z)P'(z) + i = 0. \tag{A.10}$$

These equations can simply be solved by integration, which leads to

$$q(z) = z + q_0 \tag{A.11}$$

$$P(z) = i\ln(z + q_0) \tag{A.12}$$

For convenience, we compare these results with the standard representation of Gaussian beams and find

$$\frac{1}{q(z)} = \frac{1}{z+q_0} = \frac{1}{R(z)} + \frac{-2i}{k\omega^2(z)}, \tag{A.13}$$

where $R(z)$ is the radius of curvature and $\omega(z)$ is the width of the beam. In order to obtain the integration constant q_0 we assume a plane wavefront at an arbitrary point $z = 0$. Thus, $R(0) \to \infty$ and

$$\frac{1}{q_0} = \frac{-2i}{k\omega(0)^2} \Rightarrow q_0 = \frac{ik\omega_0^2}{2} = iL_F, \tag{A.14}$$

where we call L_F Fresnel length or diffraction parameter. Substituting q_0 into Eq. A.13 and equating the real and imaginary parts yields

$$R(z) = z\Big[1 + \frac{L_F^2}{z^2}\Big] \tag{A.15}$$

$$\omega(z)^2 = \omega_0^2\Big[1 + \frac{z^2}{L_F^2}\Big] \tag{A.16}$$

The Ansatz in Eq. A.7 can also be motivated from a mathematical point of view, which clearly shows its origin. If we set the boundary conditions of the differential equation to be

$$E_G(x, y, z = 0) = A_G \exp[-ik(x^2 + y^2)/2a], \tag{A.17}$$

where A_G and a are constants. Thus the boundary condition is set to be a Gaussian distribution of the intensity. This is especially the case for paraxial beams, e.g. laser beams. We don't know how the beam profile in the transverse plane scales with the distance z from the origin. Hence, we scale the exponent with an unknown function $q(z)$. The same is true for the propagation in z-direction. We may use another unknown function $P(z)$ as a trial function. Putting all these together yields Eq. A.7, the Ansatz for solving the paraxial approximation of the Helmholtz equation. Note, that so far the two coordinates x and y are *not* independent of each other! We will study this case in the next section.

A.4 Generaliztion of the Gaussian Beam Solution

A more general approach to solving the paraxial approximation of the Helmholtz equation is to assume that the two coordinates x and y are independent of each other. To take this into account, we modify the Ansatz given in Eq. A.7 as follows:

$$E(x, y, z) = F(x, y, z)E_G(x, y, z) \tag{A.18}$$

where $F(x, y, z) = f(\frac{x}{\omega(z)})g(\frac{y}{\omega(z)}) \exp[-i\Phi(z)]$. This equation describes the electric field, where the two coordinates x and y are scaled with a real valued function $\omega(z)$ which is dependent on the z-coordinate. Furthermore, the phase is modulated with a function also dependent on z, called $\Phi(z)$. Substituting this Ansatz in Eq. 2.15 yields

$$\begin{aligned}
\left(\nabla_\perp^2 + 2ik\partial_z\right)F(x, y, z)E_G(x, y, z) &= 0 \qquad (A.19)\\
\nabla_\perp(\nabla_\perp FE) + 2ik((\partial_z F)E + F(\partial_z E)) &= 0\\
\nabla_\perp\left((\nabla_\perp F)E + F(\nabla_\perp E)\right) + 2ik((\partial_z F)E + F(\partial_z E)) &= 0\\
(\nabla_\perp^2 F)E + 2(\nabla_\perp F)(\nabla_\perp E) + F(\nabla_\perp^2 E) + 2ik((\partial_z F)E + F(\partial_z E)) &= 0,
\end{aligned}$$

and we note that $F\left(\nabla_\perp^2 E + \partial_z E\right) = 0$ is already satisfied. Thus, the only these terms are left

$$(\nabla_\perp^2 F)E + 2(\nabla_\perp F)(\nabla_\perp E) + 2ik(\partial_z F)E) = 0. \tag{A.20}$$

Inserting the definition of $F(x, y, z)$ in the last equation yields

$$\frac{1}{\omega^2}\left(\frac{f''}{f} + \frac{g''}{g}\right) + 2\left(-\frac{ik}{q}\right)\left(\frac{f'gx}{\omega} + \frac{fg'y}{\omega}\right) + 2ik\left(\frac{f'gx\omega'}{\omega^2} + \frac{fg'y\omega'}{\omega^2} + ifg\Phi'\right) = 0, \tag{A.21}$$

where $f' = \partial_x f$, $f'' = \partial_x^2 f$, $g' = \partial_y g$, $g'' = \partial_y^2 g$, $\omega' = \partial_z\omega$, $\Phi' = \partial_z\Phi$, $q = q(z)$ and $\omega = \omega(z)$. This was calculated using

$$\nabla_\perp^2 F = \tfrac{\exp[-i\Phi(z)]}{\omega^2}\left(f''g + fg''\right) \tag{A.22}$$

$$\nabla_\perp F = \tfrac{\exp[-i\Phi(z)]}{\omega}\begin{pmatrix} f'g \\ g'f \end{pmatrix} \tag{A.23}$$

$$\nabla_\perp E = E\tfrac{-ik}{q(z)}\begin{pmatrix} x \\ y \end{pmatrix} \tag{A.24}$$

$$\partial_z f = \tfrac{x}{\omega(z)^2}\tfrac{\partial f}{\partial x}\tfrac{\partial\omega(z)}{\partial z}. \tag{A.25}$$

Further simplifying of Eq. A.21 leads to

$$\frac{f''}{f} + \frac{g''}{g} + 2ikx\frac{f'}{f}\Big(\frac{\partial\omega}{\partial z} - \frac{\omega}{q}\Big) + 2iky\frac{g'}{g}\Big(\frac{\partial\omega}{\partial z} - \frac{\omega}{q}\Big) \\ -2k\omega^2\Phi'(z) = 0 \tag{A.26}$$

From Eq. A.15 we see that

$$\frac{\partial\omega}{\partial z} - \frac{\omega}{q} = \frac{\omega}{R} - \Big(\frac{\omega}{R} - \frac{2i}{k\omega}\Big) \tag{A.27}$$

holds. Thus, Eq. A.21 further simplifies to

$$\frac{f''}{f} + \frac{g''}{g} - 4\frac{x}{\omega}\frac{f'}{f} - \frac{y}{\omega}\frac{g'}{g} - 2k\omega^2\Phi'(z) = 0, \tag{A.28}$$

where we see that

$$\frac{1}{f}\Big(f'' - 2\xi f'\Big) = -2m \tag{A.29}$$

satisfies a Hermite differential equation, which reads

$$\partial_\tau^2 u - 2\tau\partial_\tau u - 2tu = 0. \tag{A.30}$$

The solutions of this equation are the so called Hermite-polynoms $H_t(\tau)$. The definition is

$$H_t(\tau) = (-1)^t e^{\tau^2}\frac{d^t}{d\tau^t}e^{-\tau^2}. \tag{A.31}$$

From Eq. A.29 we see that the last term in Eq. A.28 must satisfy the following equation

$$-2m - 2n - 2k\omega^2\Phi'(z) = 0, \tag{A.32}$$

where we already assumed that $f = H_m(\xi)$ and $g = H_n(\chi)$, where $\xi = \sqrt{2}\frac{x}{\omega}$ and $\chi = \sqrt{2}\frac{y}{\omega}$. Note, the rescaling by $\sqrt{2}$ is due to the derivative. Integration of the equation above yields

$$\Phi(z) = -\frac{m+n}{k\omega_0^2}L_F\arctan\Big(\frac{z}{L_F}\Big). \tag{A.33}$$

Hence, the generalized solution of the paraxial approximation of the Helmholtz equation is

$$E_{H-G}^{m,n}(x,y,z) = A_{H-G}^{m,n}H_m\Big(\sqrt{2}\frac{x}{\omega(z)}\Big)H_n\Big(\sqrt{2}\frac{y}{\omega(z)}\Big)\exp\Big[-i\Phi_{m,n}(z)\Big]\exp\Big[-iP(z)\Big]\exp\Big[-\frac{ik(x^2+y^2)}{2q(z)}\Big], \tag{A.34}$$

where $A_{H-G}^{m,n}$ is a normalization constant.

A.5 Generalized Solution in Cylindrical Coordinates, LG-Modes

The solution of the paraxial approximation of the Helmholtz equation 2.15 in cylindrical coordinates follows the same procedure as given in the previous section for cartesian coordinates. The transverse Laplacian in cylindrical coordinates reads

$$\nabla_\perp^2 = \frac{1}{\rho}\frac{\partial}{\partial\rho}\Big(\rho\frac{\partial f}{\partial\rho}\Big) + \frac{1}{\rho^2}\frac{\partial^2 f}{\partial\varphi^2}, \tag{A.35}$$

where $\rho^2 = x^2 + y^2$ and $\varphi = \arctan(\frac{y}{x})$. The Ansatz is slightly modified and now reads

$$E(\rho, \varphi, \omega) = g(\rho/\omega) \exp\Big[- i\Phi(z)\Big] \exp\Big[- i\Big(P + \frac{k}{2q}\rho^2 + l\varphi\Big)\Big]. \tag{A.36}$$

We spare out the detailed calculation, and just present the result here. For the function g we find

$$g(\frac{\rho}{\omega}) = \Big(\sqrt{2}\frac{\rho}{\omega}\Big)^l L_p^l(2\frac{\rho^2}{\omega^2}), \tag{A.37}$$

where L_p^l denotes the generalized Laguerre polynomial, and p and l are the radial and the angular mode numbers, respectively. The phase shift is again dependent on the mode number and reads in the case of cylindrical coordinates

$$\Phi_{l,p}(z) = (2p + |l| + 1)\arctan\Big(\frac{z}{L_F}\Big). \tag{A.38}$$

Collecting all the results leads to the general solution in cylindrical coordinates, and reads

$$E_{L-G}^{l,p}(\rho, \varphi, z) = A_{L-G}^{l,p}\Big(\sqrt{2}\frac{\rho}{\omega}\Big)^l L_p^l(2\frac{\rho^2}{\omega^2}) \exp\Big[- i\Phi(z)\Big] \exp\Big[- i\Big(P + \frac{k}{2q}\rho^2 + l\varphi\Big)\Big], \tag{A.39}$$

where again $A_{L-G}^{l,p}$ is a normalization constant.

A.6 Linear Momentum Density of a Helical Beam

The vector potential of a linearly polarized laser mode in the Lorentz gauge is given by

$$\mathbf{A} = \mathbf{x}u(x, y, z)e^{-ikz}, \tag{A.40}$$

with $\mathbf{x}$ denoting the unit vector in x-direction and $u(x, y, z)$ is a complex scalar function. In the Lorentz gauge the electric and magnetic field can be expressed as

$$\begin{aligned} \mathbf{B} &= \nabla \times \mathbf{A} \\ \mathbf{E} &= -\nabla\varphi - ik\mathbf{A} = -(i/k)\nabla\,(\nabla \cdot \mathbf{A}) - ik\mathbf{A}, \end{aligned} \tag{A.41}$$

and thus the electric and magnetic field can be written as

$$\begin{aligned} \mathbf{E} &= \tfrac{e^{ikz}}{k}\begin{pmatrix} -i\left(k^2u(x, y, z) + u^{(2,0,0)}(x, y, z)\right) \\ -iu^{(1,1,0)}(x, y, z) \\ ku^{(1,0,0)}(x, y, z) - iu^{(1,0,1)}(x, y, z) \end{pmatrix} \\ \mathbf{B} &= e^{ikz}\begin{pmatrix} 0 \\ u^{(0,0,1)}(x, y, z) + iku(x, y, z) \\ -u^{(0,1,0)}(x, y, z) \end{pmatrix}, \end{aligned} \tag{A.42}$$

with $u^{(x,y,z)}$ denoting the number of partial derivatives with respect to the respective coordinate. Neglecting second derivatives and the product of first derivatives yields

$$\begin{aligned} \mathbf{E} &= \tfrac{e^{ikz}}{k}\begin{pmatrix} -ik^2u(x, y, z) \\ 0 \\ ku^{(1,0,0)}(x, y, z) \end{pmatrix} \\ \mathbf{B} &= e^{ikz}\begin{pmatrix} 0 \\ u^{(0,0,1)}(x, y, z) + iku(x, y, z) \\ -u^{(0,1,0)}(x, y, z) \end{pmatrix}. \end{aligned} \tag{A.43}$$

The time averaged real part of the linear momentum density $\varepsilon_0 \mathbf{E} \times \mathbf{B}$ is evaluated to

$$\begin{aligned} \langle \Re\left[\mathbf{p}(t)\right] \rangle_t = \langle \Re\left[\varepsilon_0 \mathbf{E}(t) \times \mathbf{B}(t)\right] \rangle_t &= \frac{\varepsilon_0}{2} \left\langle \Re\left[\mathbf{E}e^{i\omega t} + \mathbf{E}^* e^{-i\omega t}\right] \times \Re\left[\mathbf{B}e^{i\omega t} + \mathbf{B}^* e^{-i\omega t}\right] \right\rangle_t \\ &= \Re\left[\frac{\varepsilon_0}{2T} \int_0^T \mathrm{d}t \left(\mathbf{E} \times \mathbf{B}^* + \mathbf{E} \times \mathbf{H} e^{i2\omega t}\right)\right] = \frac{\varepsilon_0}{2}\left(\mathbf{E}^* \times \mathbf{B} + \mathbf{E} \times \mathbf{B}^*\right). \end{aligned} \tag{A.44}$$

With the electric and magnetic fields given in Eq. A.43 the expression

$$\frac{\varepsilon_0}{2}\left(\mathbf{E}^* \times \mathbf{B} + \mathbf{E} \times \mathbf{B}^*\right) = i\frac{\varepsilon_0}{2}\left(u^* \nabla u - u \nabla u^*\right) + k\varepsilon_0 \, |u|^2 \, \mathbf{z}, \tag{A.45}$$

can be calculated. This expression can now be used to calculate the linear momentum density in the regime of the paraxial approximation.

A.7 HOM Interference Theory Details

Starting from Eq. 4.6 we will show here how to calculate Eq. 4.10:

$$|\psi\rangle \xrightarrow{BS} |\psi'\rangle = \frac{1}{2} \iint \mathrm{d}\omega_1 \mathrm{d}\omega_2 \, \varphi(\omega_1)\varphi(\omega_2)\exp(i\omega_1\tau)[i\hat{a}^\dagger(\omega_1) + \hat{b}^\dagger(\omega_1)][i\hat{b}^\dagger(\omega_2) + \hat{a}^\dagger(\omega_2)] \, |0\rangle \, . \tag{A.46}$$

According to Eq. 4.8 the expectation value of detecting a coincidence event is given by

$$P = \langle\psi| \, \hat{D}_a \otimes \hat{D}_b \, |\psi\rangle \, , \tag{A.47}$$

with

$$\langle\psi| = \frac{1}{2} \langle 0| \iint \mathrm{d}\omega_1' \mathrm{d}\omega_2' \, \varphi^*(\omega_1')\varphi^*(\omega_2')\exp(-i\omega_1'\tau)[-i\hat{a}(\omega_1') + \hat{b}(\omega_1')][-i\hat{b}(\omega_2') + \hat{a}(\omega_2')] \tag{A.48}$$

and

$$\hat{D}_a \otimes \hat{D}_b = \int \mathrm{d}\omega_a \, \mathrm{d}\omega_b \, \hat{a}^\dagger(\omega_a)\hat{b}^\dagger(\omega_b) \, |0\rangle \langle 0| \, \hat{a}(\omega_a)\hat{b}(\omega_b). \tag{A.49}$$

Inserting the last two equations into Eq. A.47 yields

$$\begin{aligned} P = \frac{1}{4} \langle 0| \iint \mathrm{d}\omega_1' \mathrm{d}\omega_2' \, \varphi^*(\omega_1')\varphi^*(\omega_2')\exp(-i\omega_1'\tau)[-i\hat{a}(\omega_1') + \hat{b}(\omega_1')][-i\hat{b}(\omega_2') + \hat{a}(\omega_2')] \times \\ \times \int \mathrm{d}\omega_a \int \mathrm{d}\omega_b \, \hat{a}^\dagger(\omega_a)\hat{b}^\dagger(\omega_b) \, |0\rangle \langle 0| \, \hat{a}(\omega_a)\hat{b}(\omega_b) \times \\ \times \int \mathrm{d}\omega_1 \int \mathrm{d}\omega_2 \, \varphi(\omega_1)\varphi(\omega_2)\exp(i\omega_1\tau)[i\hat{a}^\dagger(\omega_1) + \hat{b}^\dagger(\omega_1)][i\hat{b}^\dagger(\omega_2) + \hat{a}^\dagger(\omega_2)] \, |0\rangle \, . \end{aligned} \tag{A.50}$$

Equations like these are solved as follows. We may recognize that there are actually two expectation values involved:

$$\langle 0| \cdots \quad \cdots |0\rangle \langle 0| \cdots \quad \cdots |0\rangle \tag{A.51}$$

and in each of them are the creation and annihilation operators. Lets take the first expectation value as an example. There are two creation operators acting on the vacuum $\hat{a}^\dagger(\omega_a)\hat{b}^\dagger(\omega_b) \, |0\rangle$. The aim is to get rid of all creation and annihilation operators. This can be done by reordering (also called normal ordering) of the operators, such that all annihilation operators are far right acting on the vacuum ket $|0\rangle$. Then the annihilation operator is acting on the vacuum and this will be zero.

In order to do so, the two creation operators have to be moved to the very left of the equation. This can be achieved by using the commutator relations defined in section 3:

$$[\hat{a}(\omega_x), \hat{a}^\dagger(\omega_y)] = \delta(\omega_x - \omega_y)$$
$$[\hat{b}(\omega_x), \hat{b}^\dagger(\omega_y)] = \delta(\omega_x - \omega_y). \tag{A.52}$$

Expanding the square brackets in the first expectation value yields

$$\Big[-i\hat{a}(\omega_1)\hat{a}(\omega_2) - \hat{a}(\omega_1)\hat{b}(\omega_2) + \hat{b}(\omega_1)\hat{a}(\omega_2) - i\hat{b}(\omega_1)\hat{b}(\omega_2)\Big]\hat{a}^\dagger(\omega_a)\hat{b}^\dagger(\omega_b)\,|0\rangle\,. \tag{A.53}$$

Whenever there are two terms in the same mode, e.g. $\hat{b}(\omega_1)\hat{b}(\omega_2)$, the creation operator $\hat{a}^\dagger(\omega_a)$ can be interchanged with these terms because they commute and thus $\langle 0|\,\hat{a}^\dagger(\omega_a) = 0$. So these terms do not contribute. The other two terms left in the equation yield:

$$\Big[\delta(\omega_2 - \omega_a)\delta(\omega_1 - \omega_b) - \delta(\omega_1 - \omega_a)\delta(\omega_2 - \omega_b)\Big]\,|0\rangle\,. \tag{A.54}$$

Since there are no more operators left in the expectation value $\langle 0|\cdots\quad\cdots|0\rangle$ and with $\langle 0|0\rangle = 1$ follows for the first part

$$\iiiint \mathrm{d}\omega_a \mathrm{d}\omega_b \mathrm{d}\omega_1' \mathrm{d}\omega_2' \varphi^*(\omega_1')\varphi^*(\omega_2')\exp(-i\omega_1'\tau)\Big[\delta(\omega_2' - \omega_a)\delta(\omega_1' - \omega_b) - \delta(\omega_1' - \omega_a)\delta(\omega_2' - \omega_b)\Big]. \tag{A.55}$$

Evaluating the two integrals $\iint \mathrm{d}\omega_1'\mathrm{d}\omega_2'$ results in

$$\iint \mathrm{d}\omega_a \mathrm{d}\omega_b \varphi^*(\omega_a)\varphi^*(\omega_b)\Big[\exp(-i\omega_b\tau) - \exp(-i\omega_a\tau)\Big]. \tag{A.56}$$

Repeating the same calculation for the second part gives

$$\iint \mathrm{d}\omega_a \mathrm{d}\omega_b \varphi(\omega_a)\varphi(\omega_b)\Big[\exp(i\omega_b\tau) - \exp(i\omega_a\tau)\Big], \tag{A.57}$$

where the integrals in the above two equations are over both expressions, hence

$$\iint \mathrm{d}\omega_a \mathrm{d}\omega_b\, |\varphi(\omega_a)\varphi(\omega_b)|^2 \Big[\exp(-i\omega_b\tau) - \exp(-i\omega_a\tau)\Big]\Big[\exp(i\omega_b\tau) - \exp(i\omega_a\tau)\Big]. \tag{A.58}$$

Simplifying and substitution into the equation for the expectation value P yields the final result:

$$P = \frac{1}{4}\iint \mathrm{d}\omega_a \mathrm{d}\omega_b\, |\varphi(\omega_a)\varphi(\omega_b)|^2 \Big[2 - 2\mathrm{Cos}((\omega_a - \omega_b)\tau)\Big]. \tag{A.59}$$

A.8 HOM Interference Supplementary Data

Data for $\ell = 0$:

	Estimate	Standard Error	t-Statistic	P-Value
Δx	0.00452409	0.0016068	2.8156	0.00590874
A	305.283	7.36987	41.423	0
σ	0.163756	0.00493086	33.2105	0
B	279.79	7.29734	38.3415	0

(A.60)

Data for $\ell = 1$:

	Estimate	Standard Error	t-Statistic	P-Value
Δx	−0.00643404	0.00128128	−5.02158	2.361533^-6
A	235.506	6.52007	36.1201	0
σ	0.166037	0.00480536	34.5525	0
B	228.615	6.48255	35.2662	0

(A.61)

Data for $\ell = 2$:

	Estimate	Standard Error	t-Statistic	P-Value
Δx	0.00168968	0.000510236	3.31155	0.00130848
A	153.046	1.77636	86.1571	0
σ	0.18132	0.00217809	83.2473	0
B	147.102	1.75855	83.6494	0

(A.62)

Data for $\ell = 3$:

	Estimate	Standard Error	t-Statistic	P-Value
Δx	−0.000202158	0.00200002	−0.101078	0.919699
A	54.2777	2.15611	25.1739	0
σ	0.157575	0.0066269	23.7781	0
B	52.9281	2.15	24.6177	0

(A.63)

Data for $\ell = 4$:

	Estimate	Standard Error	t-Statistic	P-Value
Δx	−0.00122533	0.00351524	−0.348577	0.728998
A	56.1218	3.0633	18.3207	0
σ	0.17667	0.0124797	14.1566	0
B	50.5842	2.9881	16.9286	0

(A.64)

Data for $\ell = 5$:

	Estimate	Standard Error	t-Statistic	P-Value
Δx	−0.00353906	0.00200383	−1.76615	0.0805501
A	12.8785	0.514283	25.0416	0
σ	0.171916	0.00752344	22.8507	0
B	12.2874	0.50903	24.1387	0

(A.65)

Data for dip measurement of a superposition of $\ell = 0$ and $\ell = 2$:

	Estimate	Standard Error	t-Statistic	P-Value
Δx	−0.00122533	0.00351524	−0.348577	0.728998
A	56.1218	3.0633	18.3207	0
σ	0.17667	0.0124797	14.1566	0
B	50.5842	2.9881	16.9286	0

(A.66)

Data for bump measurement of a superposition of $\ell = 0$ and $\ell = 2$:

	Estimate	Standard Error	t-Statistic	P-Value
Δx	0.0137063	0.00906623	1.5118	0.137424
A	53.9051	2.14421	25.1398	0
σ	0.189422	0.0198024	9.56557	0
B	−39.8251	3.02491	−13.1657	0

(A.67)

A.9 2-Dimensional Subspace Measurements

Let us assume a general two particle d-dimensional pure state reads

$$|\psi\rangle = \sum_{i,j=0}^{d-1} a_{ij} |ij\rangle \tag{A.68}$$

with $a_{ij} \in \mathbb{C}$, $\sum_{i,j=0}^{d-1} \left|a_{ij}\right|^2 = 1$ and $\{ |ij\rangle \}$ forming a bi-orthonormal basis in d-dimensions. Thus the corresponding density matrix is given by

$$\rho = |\psi\rangle \langle\psi| = \sum_{i,j,k,l=0}^{d-1} a_{ij} a_{kl}^* |ij\rangle \langle kl| . \tag{A.69}$$

We define the Pauli matrices in analogy to the two-dimensional ones as

$$\begin{aligned} \sigma_x^{i,j} &= |i\rangle \langle j| + |j\rangle \langle i| \\ \sigma_y^{i,j} &= i\,|i\rangle \langle j| - i\,|j\rangle \langle i| , \end{aligned} \tag{A.70}$$

with i outside the ket denoting the imaginary unit. Thus for a two party system the tensor product of two Pauli matrices is given by

$$\begin{aligned} \sigma_x^{m,n} \otimes \sigma_x^{o,p} &= \Big(|m\rangle \langle n| + |n\rangle \langle m| \Big) \otimes \Big(|o\rangle \langle p| + |p\rangle \langle o| \Big) = \\ &|mo\rangle \langle np| + |no\rangle \langle mp| + |mp\rangle \langle no| + |np\rangle \langle mo| \\ \sigma_y^{m,n} \otimes \sigma_y^{o,p} &= -|mo\rangle \langle np| + |no\rangle \langle mp| + |mp\rangle \langle no| - |np\rangle \langle mo| \\ \sigma_x^{m,n} \otimes \sigma_y^{o,p} &= i\,|mo\rangle \langle np| + i\,|no\rangle \langle mp| - i\,|mp\rangle \langle no| - i\,|np\rangle \langle mo| \\ \sigma_y^{m,n} \otimes \sigma_x^{o,p} &= i\,|mo\rangle \langle np| - i\,|no\rangle \langle mp| + i\,|mp\rangle \langle no| - i\,|np\rangle \langle mo| . \end{aligned} \tag{A.71}$$

The expectation value of these operators is then given by

$$\begin{aligned} &\mathrm{Tr}\Big(\rho \sigma_x^{m,n} \otimes \sigma_x^{o,p}\Big) = \\ &= \mathrm{Tr}\Big(\textstyle\sum_{i,j,k,l=0}^{d-1} a_{ij} a_{kl}^* |ij\rangle \langle kl| \left(|mo\rangle \langle np| + |no\rangle \langle mp| + |mp\rangle \langle no| + |np\rangle \langle mo| \right)\Big) = \\ &= \mathrm{Tr}\Big(\textstyle\sum_{i,j,k,l=0}^{d-1} a_{ij} a_{kl}^* (\delta_{k,m}\delta_{l,o} |ij\rangle \langle np| + \delta_{k,n}\delta_{l,o} |ij\rangle \langle mp| + \delta_{k,m}\delta_{l,p} |ij\rangle \langle no| + \delta_{k,n}\delta_{l,p} |ij\rangle \langle mo|)\Big) = \\ &= \mathrm{Tr}\Big(\textstyle\sum_{i,j,k,l=0}^{d-1} a_{ij} a_{kl}^* (\delta_{k,m}\delta_{l,o}\delta_{i,n}\delta_{j,p} + \delta_{k,n}\delta_{l,o}\delta_{i,m}\delta_{j,p} + \delta_{k,m}\delta_{l,p}\delta_{i,n}\delta_{j,o} + \delta_{k,n}\delta_{l,p}\delta_{i,m}\delta_{j,o})\Big) = \\ &= a_{np} a_{mo}^* + a_{mp} a_{no}^* + a_{no} a_{mp}^* + a_{mo} a_{np}^* = \\ &= 2\Re\Big(\langle np| \rho |mo\rangle \Big) + 2\Re\Big(\langle mp| \rho |no\rangle \Big) \end{aligned} \tag{A.72}$$

where we used in the second row $\langle kl|mo\rangle = \delta_{k,m}\delta_{l,o}$ and in the third row that the trace yields $\mathrm{Tr}(|ij\rangle \langle np|) = \delta_{i,n}\delta_{j,p}$. Calculating the other three expectations values results in

$$\begin{aligned} \mathrm{Tr}\Big(\rho \sigma_y^{m,n} \otimes \sigma_y^{o,p}\Big) &= -2\Re\Big(\langle np| \rho |mo\rangle \Big) + 2\Re\Big(\langle mp| \rho |no\rangle \Big) \\ \mathrm{Tr}\Big(\rho \sigma_x^{m,n} \otimes \sigma_y^{o,p}\Big) &= -2\Im\Big(\langle np| \rho |mo\rangle \Big) + 2\Im\Big(\langle mp| \rho |no\rangle \Big) \\ \mathrm{Tr}\Big(\rho \sigma_y^{m,n} \otimes \sigma_x^{o,p}\Big) &= -2\Im\Big(\langle np| \rho |mo\rangle \Big) - 2\Im\Big(\langle mp| \rho |no\rangle \Big). \end{aligned} \tag{A.73}$$

Hence, a general element of the d-dimensional bipartite density matrix ρ is given in terms of the above introduced generalization of the Pauli-matrices by

$$\begin{aligned} \Re\Big(\langle mp| \rho |no\rangle \Big) &= \tfrac{1}{4}\mathrm{Tr}\Big(\rho(\sigma_x^{m,n} \otimes \sigma_x^{o,p} + \sigma_y^{m,n} \otimes \sigma_y^{o,p})\Big) \\ \Im\Big(\langle mp| \rho |no\rangle \Big) &= \tfrac{1}{4}\mathrm{Tr}\Big(\rho(\sigma_y^{m,n} \otimes \sigma_x^{o,p} - \sigma_x^{m,n} \otimes \sigma_y^{o,p})\Big). \end{aligned} \tag{A.74}$$

A.10 Measuring Generalized Pauli Matrices with Projective Measurements

As mentioned in the main text, with the experimental apparatus available in our setup, only projective measurements can be performed. A projective measurement $\widehat{\mathcal{P}}$ is decomposable in the following way

$$\widehat{\mathcal{P}} = |p\rangle\langle p|, \tag{A.75}$$

and $|p\rangle$ can be any arbitrary normalized superposition $|p\rangle = \alpha_1 |p_1\rangle + \alpha_2 |p_2\rangle + \cdots + \alpha_k |p_k\rangle$. Thus the generalized Pauli matrices introduced in the previous section A.9 are non-projective measurements. Given the definition of the generalized Pauli matrices and projective measurements, it is straightforward to find a recipe to decompose the generalized Pauli matrices into projective measurements. Let us start with some definitions

$$\begin{aligned}
\widehat{\mathcal{P}}_+(a,b) &= |+\rangle\langle +|_{(a,b)} = |a\rangle\langle a| + |b\rangle\langle b| + |a\rangle\langle b| + |b\rangle\langle a| \\
\widehat{\mathcal{P}}_-(a,b) &= |-\rangle\langle -|_{(a,b)} = |a\rangle\langle a| + |b\rangle\langle b| - |a\rangle\langle b| - |b\rangle\langle a| \\
\widehat{\mathcal{P}}_{+i}(a,b) &= |+i\rangle\langle +i|_{(a,b)} = |a\rangle\langle a| + |b\rangle\langle b| - i\,|a\rangle\langle b| + i\,|b\rangle\langle a| \\
\widehat{\mathcal{P}}_{-i}(a,b) &= |-i\rangle\langle -i|_{(a,b)} = |a\rangle\langle a| + |b\rangle\langle b| + i\,|a\rangle\langle b| - i\,|b\rangle\langle a|,
\end{aligned} \tag{A.76}$$

where $|+\rangle_{(a,b)} = |a\rangle + |b\rangle$, $|-\rangle_{(a,b)} = |a\rangle - |b\rangle$, $|+i\rangle_{(a,b)} = |a\rangle + i\,|b\rangle$ and $|-i\rangle_{(a,b)} = |a\rangle - i\,|b\rangle$. Thus the generalized Pauli matrices now read

$$\begin{aligned}
\sigma_{\mathrm{x}}^{\mathrm{a,b}} &= \frac{1}{2}\left(\widehat{\mathcal{P}}_+(a,b) - \widehat{\mathcal{P}}_-(a,b)\right) \\
\sigma_{\mathrm{y}}^{\mathrm{a,b}} &= \frac{1}{2}\left(\widehat{\mathcal{P}}_{-i}(a,b) - \widehat{\mathcal{P}}_{+i}(a,b)\right).
\end{aligned} \tag{A.77}$$

Hence, in order to measure one generalized Pauli operator on one subsystem, two projective measurements need to be performed in the actual experiment. Furthermore, to measure the real and imaginary part of one off-diagonal element according to Eq. A.74, 16 projective measurements need to be performed in the experiment.

A.11 Details of the SHG beam

The pump beam intensity profile is depicted in Fig. A.1. The abscissa and ordinate represent pixels of the camera. The major axis of the elliptical Gaussian is given by 370μm and the minor axis is 231μm. These results in an ellipticity of approximately $\varepsilon \approx 0.61$. This could potentially be the

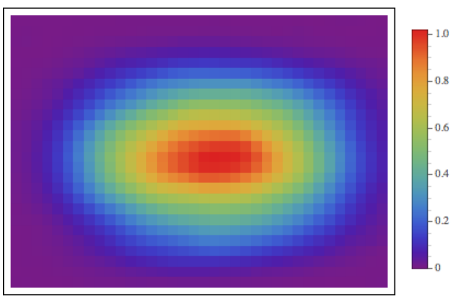

Figure A.1: Intensity plot of the pump beam for the SPDC process created in a BBO SHG process.

reason for the complex phases introduces in the down-converted state, see Fig. 5.5 for example. However, this has not been verified yet.

A.12 Density Matrix Elements Reconstruction

Here we describe in detail how the reconstruction of density matrix elements is performed. In section A.9 the measurement procedure is given in terms of generalized Pauli matrices. The projective measurement to be performed for each Pauli matrix is explained in section A.10. As an illustrative example let us reconstruct one specific element of the 10-dimensionally entangled state shown in Fig. 5.5. We choose $|-3,3\rangle\langle 0,0|$, thus the real and imaginary part is given by

$$\begin{aligned}\Re\Big(\langle -3,3|\,\rho\,|0,0\rangle\Big) &= \tfrac{1}{4}\mathrm{Tr}\Big(\rho(\sigma_x^{-3,0}\otimes\sigma_x^{0,3}+\sigma_y^{-3,0}\otimes\sigma_y^{0,3})\Big) \\ \Im\Big(\langle -3,3|\,\rho\,|0,0\rangle\Big) &= \tfrac{1}{4}\mathrm{Tr}\Big(\rho(\sigma_y^{-3,0}\otimes\sigma_x^{0,3}-\sigma_x^{-3,0}\otimes\sigma_y^{0,3})\Big),\end{aligned} \tag{A.78}$$

and furthermore the projective measurements are given by

$$\begin{aligned}\sigma_{\mathrm{x}}^{\mathrm{a,b}} &= \tfrac{1}{2}\left(\widehat{\mathcal{P}}_{+}(a,b)-\widehat{\mathcal{P}}_{-}(a,b)\right) \\ \sigma_{\mathrm{y}}^{\mathrm{a,b}} &= \tfrac{1}{2}\left(\widehat{\mathcal{P}}_{-i}(a,b)-\widehat{\mathcal{P}}_{+i}(a,b)\right).\end{aligned} \tag{A.79}$$

with the definitions of $\widehat{\mathcal{P}}$ given in Eq. A.76. From the equation for the real and imaginary part of the density matrix element, it can be seen that the $\{-3,0\}$ and $\{0,3\}$ subspaces span the space of the corresponding density matrix element. The definitions of the projective measurements $\widehat{\mathcal{P}}$ yield that all mutually unbiased bases in these two-dimensional subspace have to be measured. This is the computational basis, the diagonal and anti-diagonal basis and the left/right basis. In the following some sample data is given: In Fig. A.2 the different subspace measurement results are

[-3], [3]	[0], [3]		[-3], [3]	[0], [3]
[-3], [0]	[0], [0]		[-3], [0]	[0], [0]
1645	21		1625	15
21	5456		15	5496
[-3]+[0], [0]+[3]	[-3]-[0], [0]+[3]		[-3]+i[0], [0]+[3]	[-3]-i[0], [0]+[3]
[-3]+[0], [0]-[3]	[-3]-[0], [0]-[3]		[-3]+i[0], [0]-[3]	[-3]-i[0], [0]-[3]
580	4291		1029	3863
4458	579		3901	1086
[-3]+i[0], [0]+i[3]	[-3]-i[0], [0]+i[3]		[-3]+[0], [0]+i[3]	[-3]-[0], [0]+i[3]
[-3]+i[0], [0]-i[3]	[-3]-i[0], [0]-i[3]		[-3]+[0], [0]-i[3]	[-3]-[0], [0]-i[3]
618	4280		3934	1034
4095	608		1139	3766

Figure A.2: Sample data to demonstrate the reconstruction of an off-diagonal matrix element.

given. Comparison of the total counts in each subspace surprisingly yields different results. For example, the total counts in the computational basis are $1654 + 21 + 21 + 5456 = 7143$, while the counts in the A,D basis yields $580 + 4291 + 4458 + 579 = 9908$. Since the total counts in a two-dimensional subspace are necessarily conserved in any mutually unbiased basis, we "renormalize" the total counts in any basis to the total counts in the computational basis. Note, however, this does definitely not result in a higher visibility in the subspaces that would in turn result in higher fidelity. In fact, with this method we account for imperfections in superposition measurements.

Furthermore, there is no clear trend in the observed data meaning sometimes the computational basis yields higher total counts and sometimes the superposition basis (A,D,L,R) result in higher total counts. We can attribute this to the fact that we do not measure exactly Laguerre-Gaussian modes with the SLMs, but close approximations to them [50].

A.13 Extended Data Table (3,3,2) State

⟨A,B,C| \ |A',B',C'⟩	|-1,-1,0⟩	|0,-1,0⟩	|1,-1,0⟩	|-1,0,0⟩	|0,0,0⟩	|1,0,0⟩	|-1,1,0⟩	|0,1,0⟩	|1,1,0⟩	|-1,-1,0⟩	|0,-1,1⟩	|1,-1,1⟩	|-1,0,1⟩	|0,0,1⟩	|1,0,1⟩	|-1,1,1⟩	|0,1,1⟩	|1,1,1⟩
⟨-1,-1,0|	0.003																	
⟨0,-1,0|		0.009																
⟨1,-1,0|			0.003															
⟨-1,0,0|				0.006														
⟨0,0,0|					0.296						0.190 - i 0.133				0.178 - i 0.129			
⟨1,0,0|						0.011												
⟨-1,1,0|							0.000											
⟨0,1,0|								0.014										
⟨1,1,0|									0.003									
⟨-1,-1,0|										0.006								
⟨0,-1,1|											0.017							
⟨1,-1,1|				0.190 + i 0.133								0.290			0.297 - i 0.026			
⟨-1,0,1|													0.006					
⟨0,0,1|														0.003				
⟨1,0,1|															0.003			
⟨-1,1,1|				0.178 + i 0.129							0.297 + i 0.026					0.313		
⟨0,1,1|																	0.014	
⟨1,1,1|																		0.003

Figure A.3: Numerical values of the measured density matrix elements. Note that here we show the real and imaginary parts of the elements.

The density matrix elements displayed in Fig. A.3 show significant complex phases in the off-diagonal elements. From the theory, we would not expect complex phases. Due to the entanglement detection scheme used here the complex phases do not matter, since only the absolute value of the off-diagonal elements is accounted for. Nevertheless, it is interesting to investigate the source of these imaginary parts of the off-diagonal elements. In section 5.4 we show that the state created in one crystal already contains significant imaginary parts in certain off-diagonal elements. A possible issue here could be the elliptical pump beam discussed in section A.11.

A.14 Pulsed vs. CW Pump Laser Source

In this section the use of pulsed vs. continuous wave (cw) laser sources in multi-photon experiments will be discussed. In this thesis and in several other experiments multiple entangled photon pairs are combined in such a way that a genuinely entangled multi-partite state is created. In order to coherently overlap two photons from two independently created pairs, these photons must be indistinguishable and- within their coherence time. The coherence time is governed by the spectral bandwidth of the down converted photon pairs. Typically, the bandwidth of photon pairs created in an SPDC process is on the order of several nanometers. Assuming a Gaussian shaped spectral distribution with a FWHM on the order of nanometers the coherence time is on the order of picoseconds. This means that the four-fold coincidence detection window must be on the order of picoseconds to ensure that only photons that are created within their coherence time are detected. Such a method is called an ultracoincidence detection technique and was implemented experimentally by Halder *et al.* [53] in 2007. The niobium nitride (NbN) superconducting single-photon detector used in their experiment has a resolution of 74ps. With 10pm narrowband filters centered at a wavelength of 1560nm the coherence time results in 350ps, which is much larger than the detection resolution. With this technique Halder *et al.*demonstrated quantum interference of two independently created photon pairs created with a continuous wave laser source.

A different approach used in most multiphoton entanglement experiments (for a comprehensive review on the topic see e.g. [54]) is to create the photon pairs with a pulsed laser source. The big advantage of this technique is the commercial availability of femtosecond pulsed Ti:Sapph laser sources. The femtosecond pulses with a repetition rate of roughly 80MHz relaxes the stringent condition on the detection time window. If we assume that the photon pairs are created within the same pulse, then a nanometer spectral filtering is sufficient to ensure that the independently created photon pairs are within their coherence time. The repetition rate of 80MHz allows for a detection window of several nanoseconds.

A.15 Power Dependence and Statistics of Four-Fold-Events

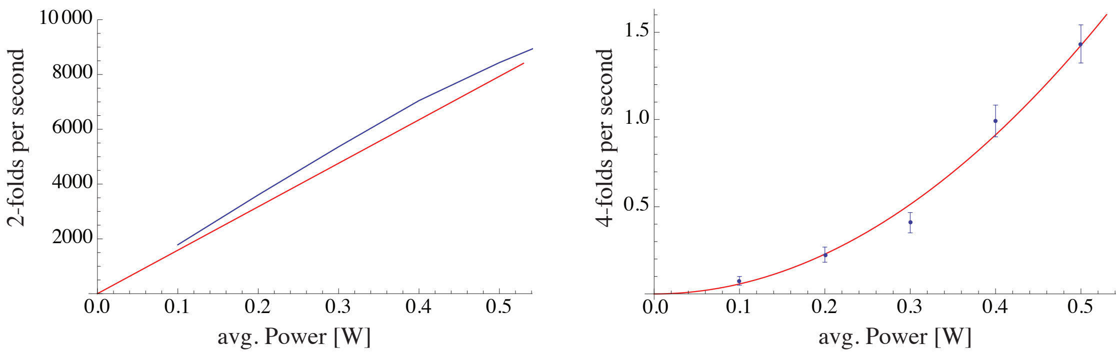

Figure A.4: Two and four-fold dependence on the average pump power P. The experimental data is depicted in blue, while the linear and quadratic fit is displayed in red. The linear dependence of the two-folds on the average pump power is clearly shown. Additionally, the quadratic dependence of the four-folds on the pump power is shown. The error bars depicted are due to counting statistics. Note that the integration time for the four-fold counts is 120 seconds.

As depicted in Fig. A.4 the 2-fold coincidences in the spontaneous parametric down conversion process are linearly dependent on the pump power. The pump laser used in this experiment is a pulsed Ti:Sapph laser with 80MHz repetition rate and a pulse length of 140fs. The maximal output power is approximately 3.8W at 808nm wavelength. Due to the short pulses (Fourier-limit) the spectral bandwidth is approximately 20nm. With a second harmonic process in a β-barium-borate

(BBO) crystal the 808nm laser light is transformed to 404 nm. The pump power shown in Fig. A.4 varies from 0.1W to 0.5W. The number of photons contained in each pulse is given by

$$\mathcal{N}_{pp} = \frac{P\lambda}{2\pi c\hbar R}, \tag{A.80}$$

where P is the average power, λ the center wavelength, c the speed of light, $\hbar$ the reduced Planck constant and R the repetition rate of the laser. Thus for 0.5W there are approximately 10^{10} photons. Let us describe the linear dependence of the 2-fold coincidences with [55]

$$C_{2f} = R\mu\eta^2 \tag{A.81}$$

with μ denoting the average pair number created in a pulse and η describing the overall efficiency. The overall efficiency is given by

- Detector: 65%
- SLM: 85%
- Reflection and absorption: 95%
- Single mode fiber coupling: 60%
- Narrowband filtering (3nm): 30%

which leads to an overall efficiency of approximately 10%. This yields an average photon pair number of $\mu = 0.01$ per pulse at 0.5W pump power. The expected N pair emission of the SPDC process is of order [55]

$$C_{2N} = R\mu^N\eta^{2N}. \tag{A.82}$$

For the case of 2 pairs created simultaneously this ($N = 2$) this results in a quadratic dependence of the mean photon number μ:

$$C_{4f} = R\mu^2\eta^4, \tag{A.83}$$

and inserting the above numbers yield 0.8 four-fold coincidences per second as an estimate. The four-fold measurement results in Fig. A.4 clearly shows the quadratic dependence on the power, hence the mean pair number per pulse.

A.16 Higher Order Effects

Higher-order effects. There are two kinds of higher order effects that need to be addressed in our experiment. The expected output from down-conversion in the OAM basis can be written as $(|0\rangle|0\rangle + |\text{-}1\rangle|1\rangle + |1\rangle|\text{-}1\rangle + |\text{-}2\rangle|2\rangle + |2\rangle|\text{-}2\rangle + |\text{-}3\rangle|3\rangle + |3\rangle|\text{-}3\rangle ...)$. We only use the first three terms in our experiment, because they have the largest amplitudes that give us the largest count rates. If a higher-order mode ($|\ell| > 1$) is created in the first crystal NL1, the trigger T would not fire (because it only triggers for mode 0 and -1). Thus, these higher-order modes do not contribute to the state. As we consider only the 3×3-dimensional space spanned by $\ell \in \{-1, 0, 1\}$, higher-order modes from the second crystal NL2 also do not contribute to our measured state, as in that case photon A would be outside the considered subspace.

The second type of higher order effect concerns the generation of higher order emission in SPDC. The probability of obtaining two pairs from one crystal and one pair from each crystal is essentially the same. However, the contribution from higher order terms such as double-pair emission from one crystal is ruled out because our state is conditioned upon a detection event occurring at all four detectors. The four photons created in double-pair emission from either one of the crystals cannot, even in principle, be detected at all four detectors. This is because our experiment is constructed in such a way that detectors A and T only measure photons created crystal 2 and 1 respectively. The probability of even higher-order terms being generated, such as triple-pair emission, is roughly 10^{-4} to 10^{-5} times more unlikely than a double-pair emission, and can be safely neglected.

Bibliography

[1] Albert Einstein, Boris Podolsky, and Nathan Rosen. Can quantum-mechanical description of physical reality be considered complete? *Physical review*, 47(10):777, 1935.

[2] E Schrödinger. Die gegenwärtige Situation in der Quantenmechanik. *Naturwissenschaften*, 23(49):823–828, 1935.

[3] John S Bell. On the einstein podolsky rosen paradox, 1964.

[4] Thomas Monz, Philipp Schindler, Julio T Barreiro, Michael Chwalla, Daniel Nigg, William A Coish, Maximilian Harlander, Wolfgang Hänsel, Markus Hennrich, and Rainer Blatt. 14-qubit entanglement: Creation and coherence. *Physical Review Letters*, 106(13):130506, 2011.

[5] J Kelly, R Barends, AG Fowler, A Megrant, E Jeffrey, TC White, D Sank, JY Mutus, B Campbell, Yu Chen, et al. State preservation by repetitive error detection in a superconducting quantum circuit. *Nature*, 519(7541):66–69, 2015.

[6] Hannes Bernien, Bas Hensen, Wolfgang Pfaff, Gerwin Koolstra, MS Blok, Lucio Robledo, TH Taminiau, Matthew Markham, DJ Twitchen, Lilian Childress, et al. Heralded entanglement between solid-state qubits separated by three metres. *Nature*, 497(7447):86–90, 2013.

[7] Russell Stewart Deacon, A Oiwa, J Sailer, S Baba, Y Kanai, K Shibata, K Hirakawa, and S Tarucha. Cooper pair splitting in parallel quantum dot josephson junctions. *Nature communications*, 6, 2015.

[8] Mario Krenn, Marcus Huber, Robert Fickler, Radek Lapkiewicz, Sven Ramelow, and Anton Zeilinger. Generation and confirmation of a (100× 100)-dimensional entangled quantum system. *Proceedings of the National Academy of Sciences*, 111(17):6243–6247, 2014.

[9] Marcus Huber and Julio I de Vicente. Structure of multidimensional entanglement in multipartite systems. *Physical review letters*, 110(3):030501, 2013.

[10] CK Hong, ZY Ou, and Leonard Mandel. Measurement of subpicosecond time intervals between two photons by interference. *Physical Review Letters*, 59(18):2044, 1987.

[11] Daniel M Greenberger, Michael A Horne, and Anton Zeilinger. Going beyond bells theorem. In *Bells theorem, quantum theory and conceptions of the universe*, pages 69–72. Springer, 1989.

[12] John D Trimmer. The present situation in quantum mechanics: A translation of schrödinger's" cat paradox" paper. *Proceedings of the American Philosophical Society*, pages 323–338, 1980.

[13] Michael A Nielsen and Isaac L Chuang. *Quantum computation and quantum information*. Cambridge university press, 2010.

[14] Ryszard Horodecki, Paweł Horodecki, Michał Horodecki, and Karol Horodecki. Quantum entanglement. *Reviews of Modern Physics*, 81(2):865, 2009.

[15] Martin B Plenio and Shashank Virmani. An introduction to entanglement measures. *arXiv preprint quant-ph/0504163*, 2005.

[16] Dagmar Bruß. Characterizing entanglement. *Journal of Mathematical Physics*, 43(9):4237–4251, 2002.

[17] Sevag Gharibian. Strong np-hardness of the quantum separability problem. *arXiv preprint arXiv:0810.4507*, 2008.

[18] Asher Peres. Separability criterion for density matrices. *Physical Review Letters*, 77(8):1413, 1996.

[19] Michał Horodecki, Paweł Horodecki, and Ryszard Horodecki. Separability of mixed states: necessary and sufficient conditions. *Physics Letters A*, 223(1):1–8, 1996.

[20] RE Edwards. Functional analysis: Theory and applications, holt, rinehart and winston, new york, 1965. *MR*, 36:4308, 1994.

[21] Ingemar Bengtsson and Karol Zyczkowski. *Geometry of quantum states: an introduction to quantum entanglement*. Cambridge University Press, 2006.

[22] Anna Sanpera, Dagmar Bruß, and Maciej Lewenstein. Schmidt-number witnesses and bound entanglement. *Physical Review A*, 63(5):050301, 2001.

[23] Barbara M Terhal and Paweł Horodecki. Schmidt number for density matrices. *Physical Review A*, 61(4):040301, 2000.

[24] Charles H Bennett, Gilles Brassard, Claude Crépeau, Richard Jozsa, Asher Peres, and William K Wootters. Teleporting an unknown quantum state via dual classical and einstein-podolsky-rosen channels. *Physical review letters*, 70(13):1895, 1993.

[25] Charles H Bennett, Gilles Brassard, Sandu Popescu, Benjamin Schumacher, John A Smolin, and William K Wootters. Purification of noisy entanglement and faithful teleportation via noisy channels. *Physical review letters*, 76(5):722, 1996.

[26] Ilse Fasol and Gerhard Ludwig Fasol. *Ludwig Boltzmann (1844-1906): zum hundertsten Todestag*. Springer-Verlag, 2007.

[27] Melvin Lax, William H Louisell, and William B McKnight. From maxwell to paraxial wave optics. *Physical Review A*, 11(4):1365, 1975.

[28] LW Davis. Theory of electromagnetic beams. *Physical Review A*, 19(3):1177, 1979.

[29] D Gloge and D Marcuse. Formal quantum theory of light rays. *JOSA*, 59(12):1629–1631, 1969.

[30] Dietrich Marcuse. Light transmission optics. 1972.

[31] Les Allen, Marco W Beijersbergen, RJC Spreeuw, and JP Woerdman. Orbital angular momentum of light and the transformation of laguerre-gaussian laser modes. *Physical Review A*, 45(11):8185, 1992.

[32] MJ Padgett and L Allen. The poynting vector in laguerre-gaussian laser modes. *Optics communications*, 121(1):36–40, 1995.

[33] L Allen and MJ Padgett. The poynting vector in laguerre–gaussian beams and the interpretation of their angular momentum density. *Optics Communications*, 184(1):67–71, 2000.

[34] Florian Schlederer, Mario Krenn, Robert Fickler, Mehul Malik, and Anton Zeilinger. Cyclic transformation of orbital angular momentum modes. *arXiv preprint arXiv:1512.02696*, 2015.

[35] Robert W Boyd. *Nonlinear optics*. Academic press, 2003.

[36] Sonja Franke-Arnold, Stephen M Barnett, Miles J Padgett, and L Allen. Two-photon entanglement of orbital angular momentum states. *Physical Review A*, 65(3):033823, 2002.

[37] FM Miatto, D Giovannini, J Romero, S Franke-Arnold, SM Barnett, and MJ Padgett. Bounds and optimisation of orbital angular momentum bandwidths within parametric down-conversion systems. *The European Physical Journal D*, 66(7):1–6, 2012.

[38] Alois Mair, Alipasha Vaziri, Gregor Weihs, and Anton Zeilinger. Entanglement of the orbital angular momentum states of photons. *Nature*, 412(6844):313–316, 2001.

[39] RGH Van Uden, R Amezcua Correa, E Antonio Lopez, FM Huijskens, C Xia, G Li, A Schülzgen, H de Waardt, AMJ Koonen, and Chigo M Okonkwo. Ultra-high-density spatial division multiplexing with a few-mode multicore fibre. *Nature Photonics*, 8(11):865–870, 2014.

[40] Thomas Durt, Dagomir Kaszlikowski, Jing-Ling Chen, and LC Kwek. Security of quantum key distributions with entangled qudits. *Physical Review A*, 69(3):032313, 2004.

[41] Mehul Malik, Manuel Erhard, Marcus Huber, Mario Krenn, Robert Fickler, and Anton Zeilinger. Multi-photon entanglement in high dimensions. advance online publication:doi: 10.1038/nphoton.2016.12, 2016.

[42] Jonathan Leach, Johannes Courtial, Kenneth Skeldon, Stephen M Barnett, Sonja Franke-Arnold, and Miles J Padgett. Interferometric methods to measure orbital and spin, or the total angular momentum of a single photon. *Physical review letters*, 92(1):013601, 2004.

[43] Robert Fickler, Radek Lapkiewicz, Marcus Huber, Martin PJ Lavery, Miles J Padgett, and Anton Zeilinger. Interface between path and orbital angular momentum entanglement for high-dimensional photonic quantum information. *Nature communications*, 5, 2014.

[44] Mario Krenn, Mehul Malik, Robert Fickler, Radek Lapkiewicz, and Anton Zeilinger. Automated search for new quantum experiments. *arXiv preprint arXiv:1509.02749*, 2015.

[45] Josh Cadney, Marcus Huber, Noah Linden, and Andreas Winter. Inequalities for the ranks of multipartite quantum states. *Linear Algebra and its Applications*, 452:153–171, 2014.

[46] Anton Zeilinger, Michael A Horne, Harald Weinfurter, and Marek Żukowski. Three-particle entanglements from two entangled pairs. *Physical review letters*, 78(16):3031, 1997.

[47] Xing-Can Yao, Tian-Xiong Wang, Ping Xu, He Lu, Ge-Sheng Pan, Xiao-Hui Bao, Cheng-Zhi Peng, Chao-Yang Lu, Yu-Ao Chen, and Jian-Wei Pan. Observation of eight-photon entanglement. *Nature Photonics*, 6(4):225–228, 2012.

[48] R. Kaltenbaek. *Interference of Photons from Independent Sources*. PhD thesis, University of Vienna, 2009.

[49] Thomas Scheidl, Felix Tiefenbacher, Robert Prevedel, Fabian Steinlechner, Rupert Ursin, and Anton Zeilinger. Crossed-crystal scheme for femtosecond-pulsed entangled photon generation in periodically poled potassium titanyl phosphate. *Physical Review A*, 89(4):042324, 2014.

[50] Hammam Qassim, Filippo M Miatto, Juan P Torres, Miles J Padgett, Ebrahim Karimi, and Robert W Boyd. Limitations to the determination of a laguerre–gauss spectrum via projective, phase-flattening measurement. *JOSA B*, 31(6):A20–A23, 2014.

[51] Francesco Tonolini, Susan Chan, Megan Agnew, Alan Lindsay, and Jonathan Leach. Reconstructing high-dimensional two-photon entangled states via compressive sensing. 4:6542 EP –.

[52] R. VICTOR JONES. On classical electromagnetic fields, 2000. [Online; accessed 28-January-2016].

[53] Matthäus Halder, Alexios Beveratos, Nicolas Gisin, Valerio Scarani, Christoph Simon, and Hugo Zbinden. Entangling independent photons by time measurement. *Nature Physics*, 3(10):692–695, 2007.

[54] Jian-Wei Pan, Zeng-Bing Chen, Chao-Yang Lu, Harald Weinfurter, Anton Zeilinger, and Marek Żukowski. Multiphoton entanglement and interferometry. *Reviews of Modern Physics*, 84(2):777, 2012.

[55] Jérémie Fulconis, Olivier Alibart, Jeremy L OBrien, William J Wadsworth, and John G Rarity. Nonclassical interference and entanglement generation using a photonic crystal fiber pair photon source. *Physical review letters*, 99(12):120501, 2007.